Theoretical Spectral Diagnostic Analyses in Support of PBFA-II Beam-Plasma Interaction Experiments

J.J. MacFarlane and P. Wang

March 1993

UWFDM-913

FUSION TECHNOLOGY INSTITUTE

UNIVERSITY OF WISCONSIN

MADISON WISCONSIN

Theoretical Spectral Diagnostic Analyses in Support of PBFA-II Beam-Plasma Interaction Experiments

J.J. MacFarlane and P. Wang

Fusion Technology Institute
University of Wisconsin
1500 Engineering Drive
Madison, WI 53706

http://fti.neep.wisc.edu

March 1993

UWFDM-913

Table of Contents

Section I

Introduction

The purpose of this report is to summarize work performed for Sandia National Laboratories during the period March 1992-March 1993. The primary objective of this work is to provide theoretical support for the analyses of spectral measurements obtained in Particle Beam Fusion Accelerator-II (PBFA-II) experiments. In our analyses, we use: (1) a collisional-radiative equilibrium (CRE) code in which multilevel statistical equilibrium equations are solved self-consistently with the radiation field and ion beam properties; and (2) a suite of atomic physics codes which provide high quality atomic structure and cross section data for the many radiative and collisional processes that can occur in light ion beam-plasma interaction experiments. The major features of the CRE and atomic physics codes are listed in Tables 1.1 and 1.2, respectively.

The statement of work for the past year is shown in Table 1.3. The primary objective of this year concerns the analysis of inner-shell X-ray spectra from targets heated by intense lithium beams. To do this, we have improved our modeling capabilities in several areas. First, it was necessary to develop the capability to calculate the cross sections for multiple ionization events. Because of the higher charge of the projectile in present PBFA-II experiments (Li^{3+} vs. H^{+}), a higher probability exists for the ejection of more than one electron from a target atom during its interaction with a beam ion. Details of the modeling and comparisons with experimental data are presented in Section II. Second, to improve our capability to predict K_α spectra from moderate-Z targets, term-dependent fluorescence yields and Auger rates are now computed. The fluorescence yield calculations are described in Section III. Third, it was necessary to generalize the statistical equilibrium equations in the CRE model to account for the enhanced atomic physics modeling. In particular, transitions between atomic levels of non-adjacent ionization stages must be included because of multiple ionization events induced by the Li beam.

Using the enhanced modeling capabilities, calculations were performed to predict K_α spectra from Al targets heated by intense Li beams. First, we performed CRE calculations utilizing time-dependent temperature and density distributions predicted from radiation-hydrodynamics simulations carried out at Sandia. This is described in Section IV, where calculated time-dependent and time-integrated K_α spectra are compared with measurements obtained in recent PBFA-II experiments. In Section V,

Table 1.1. Major Features of Collisional-Radiative Equilibrium Code

- Multilevel, steady-state atomic rate equations are solved self-consistently with the radiation field and ion beam properties.
- Every state of a given ion is coupled to all other states (ground and excited) of that ion, and all states of the next higher ionization stage.
- Emission spectra include contributions from bound-bound (lines), bound-free (recombinations), and free-free transitions (Bremsstrahlung).
- Line shapes include effects of natural, Doppler, and Stark broadening.
- Radiation transport is modeled using either:

  (i) an angle- and frequency-averaged escape probability method, or

  (ii) a multiangle, multifrequency model based on the second-order form of the transfer equation.

Table 1.2. Major Features of Atomic Physics Models

- Atomic structure and radiative data are computed using configuration interaction (CI) method with Hartree-Fock wavefunctions.
- Multiconfiguration Hartree-Fock and Dirac-Fock calculations provide accurate transition energies and oscillator strengths for lines of interest.
- Atomic collisional data are computed using a combination of distorted wave, Coulomb-Born, and semiclassical impact parameter models.
- Ion-impact ionization cross sections are computed using a plane-wave Born approximation model with Hartree-Fock wavefunctions and with the inclusion of binding energy, Coulomb-deflection, and relativistic corrections. Multiple ionization cross sections are computed using an independent event model with a binomial distribution probability.
- Term-dependent Auger rates and fluorescence yields are calculated using an LS coupling formalism with Hartree-Fock wavefunctions.

Table 1.3. Tasks for 1992

1. Extend the capabilities of the present atomic physics and line transport model for proton-irradiated plasmas to diagnose lithium beam-heated plasmas:

   A. Estimate the effects of multiple impact ionizations on the satellite spectra.

   B. Perform CRE calculations to determine opacity effects in the target material and predict spectral fluxes.

   C. Estimate plasma density and temperature conditions through analysis of measured PBFA-II spectra.

2. Perform CRE and atomic physics calculations in support of 1992 PBFA-II experiments.

3. Document results in a final report to SNL.

4. Provide source code for the CRE/transport package for installation on Sandia's computer system.

we describe a series of calculations for Li beam-heated Al and Mg plasmas in which we examine the potential for using line intensity ratios from He-like and Li-like ions to diagnose target plasma temperatures and densities.

In addition to the above analyses, work has been performed in several other areas. The work is summarized in papers which have been submitted for publication during the past year. We include them as Appendices A, B, and C in this report. Appendices A and B concern our analysis of Al K_α spectra obtained in *proton* beam experiments on PBFA II (Bailey et al. 1990). Appendix A represents a collaborative effort between the University of Wisconsin, Sandia National Laboratories, and the University of Florida in which a detailed analysis of proton-induced Al K_α spectra was presented. Appendix B presents a detailed description of the atomic physics calculations performed for proton-irradiated K_α analysis. Finally, Appendix C presents a preliminary analysis of visible spectra obtained from the PBFA-II Ar gas cell region. This work was presented at the Beams '92 Conference last May in Washington, D.C.

Section II

Multiple Inner-Shell Ionization Processes in Targets Irradiated by Intense Lithium Beams

2.1. Introduction

Numerous studies of ion-atom collisions have shown that K-shell ionization is usually accompanied by multiple L-shell ionization. This multiple inner-shell ionization of atoms by ion beam bombardment produces rich structure in x-ray satellite spectra. Generally speaking, multiple ionization is less significant when the atomic number of the projectile is much smaller than that of target; *i.e.*, $Z_1/Z_2 \ll 1$. However, as the ratio of Z_1/Z_2 increases, multiple ionization processes become increasingly important. Figure 2.1 shows a series of Ti K_α x-ray spectra produced by different projectiles (Hill et al. 1976). It can be seen that multiple ionization effects are important for projectiles with $Z_1 \geq 2$.

K_α x-ray satellite spectroscopy has been used as a temperature and density diagnostic for plasmas heated by particle beams in inertial fusion experiments (Nardi and Zinnamon 1981; Bailey et al. 1990). K_α satellite spectra provide information on the ionization distributions in plasmas, and with that, constraints on plasma conditions. However, it should be noted that both thermal ionization and multiple inner-shell ionization by ion bombardment can influence K_α satellite spectra. For example, the Be-like K_α satellite of Al can be produced by a single K-shell ion impact ionization from B-like Al, i.e.,

$$1s^2 2s^2 2p^1 \overset{ion\ impact\ ionization}{\longrightarrow} 1s^1 2s^2 2p^1 \overset{fluorescence\ decay}{\longrightarrow} 1s^2 2s^2, \tag{2.1}$$

and by double ionization K1L1 from C-like Al (here, K1L1 represents the double ionization of one K-shell electron and one L-shell electron):

$$1s^2 2s^2 2p^2 \overset{double\ ionization}{\longrightarrow} 1s^1 2s^2 2p^1 \overset{fluorescence\ decay}{\longrightarrow} 1s^2 2s^2. \tag{2.2}$$

If multiple inner-shell ionization effects are significant, it may lead to inaccurate predictions of the ionization distributions of plasmas if it is not properly accounted for. Hence, it is very important to understand multiple inner-shell ionization effects on K_α satellite spectra when using K_α spectra as a temperature diagnostic.

We have developed a computer code, MICPSSR (Multiple Ionization calculations in the framework of Coulomb-deflection, Perturbed-Stationary-State, and Relativistic

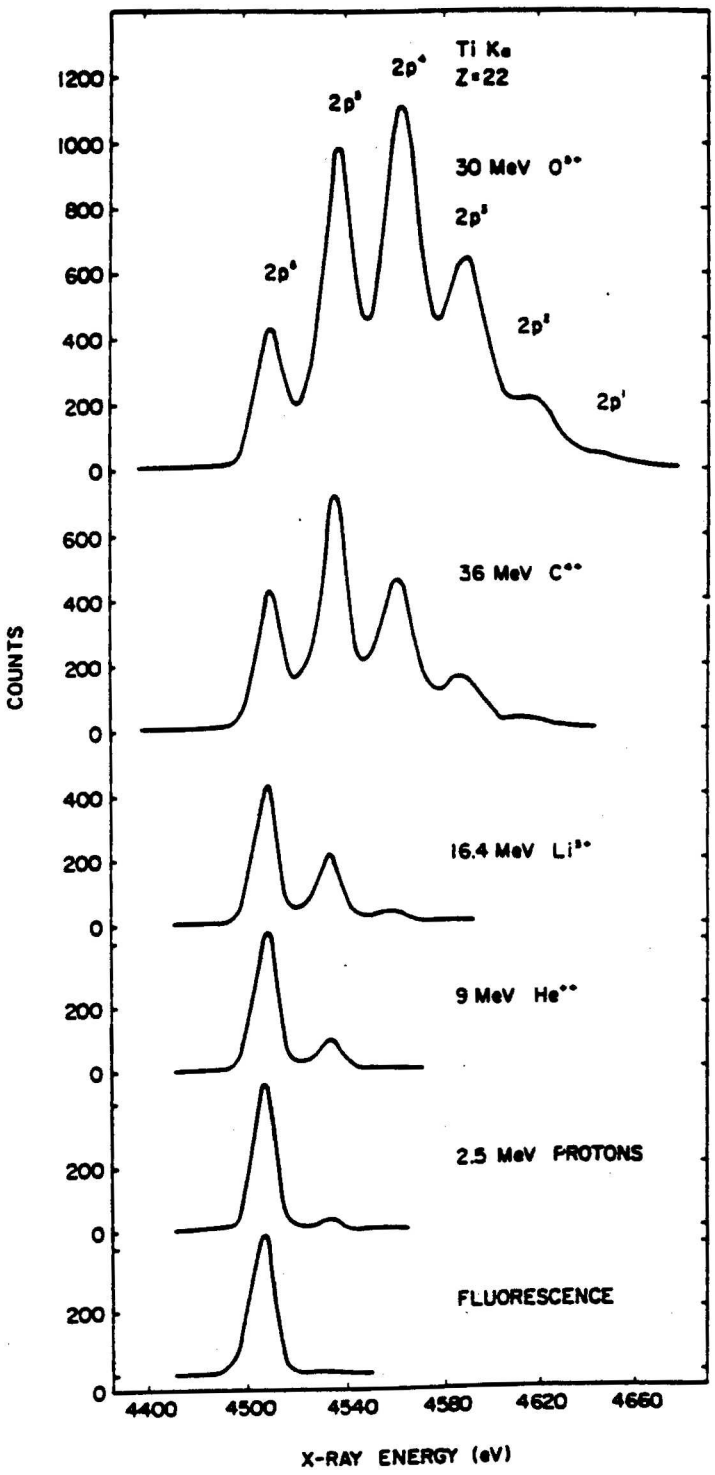

Figure 2.1. Typical Ti K_α spectra resulting from bombardment by the various projectiles.

target wavefunction model), for calculating ion impact ionization cross sections. The processes considered include single ionization, multiple ionization, and electron capture. In this section we discuss the theoretical models used in our calculations, and present results from a series of benchmark calculations, as well as results of multiple inner-shell ionization of aluminum by high velocity lithium ions.

2.2. Theoretical Models

2.2.1. Plane-Wave Born-Approximation Cross Sections

In the plane-wave-Born approximation (PWBA) (Madison et al. 1975), the cross section for ejection of an electron from an atomic subshell $(n_i l_i)$ is given by

$$\sigma(a_i, a_f) = \frac{4Z_1^2 M_1}{(2l_i+1)E_1} \sum_{l,\kappa} \int_0^{E_1-I_i} d\epsilon \int_{k_1-k_2}^{k_1+k_2} dq [R_\kappa(q)]^2 q^3. \tag{2.3}$$

Here, σ is the ionization cross section in πa_o^2, ϵ is the kinetic energy of the ejected electron in *hartree*, q is the momentum transfered to that electron, I_i is ionization threshold of the $(n_i l_i)$ subshell, and Z_1, M_1, and E_1 are the charge, mass, and initial kinetic energy of the incident particle. The quantities k_1 and k_2 are the momenta of the incident and outgoing ions, respectively:

$$k_1 = \sqrt{\frac{2E_1}{M_1}} \tag{2.4}$$

and

$$k_2 = \sqrt{k_1^2 - \frac{2(I_i+\epsilon)}{M_1}}\,. \tag{2.5}$$

The radial integral factor $R_\kappa(q)$ for the l partial wave is

$$R_\kappa(q) = \Pi(\kappa l_i l) \begin{pmatrix} \kappa & l_i & l \\ 0 & 0 & 0 \end{pmatrix} \int_0^\infty P(n_i l_i|r) P(\epsilon l|r) (j_\kappa(qr) - \delta_{\kappa 0}) dr, \tag{2.6}$$

where

$$\Pi(\kappa l_i l) = \sqrt{(2\kappa+1)(2l_i+1)(2l+1)}\,, \tag{2.7}$$

and $P(n_i l_i|r)$ and $P(\epsilon l|r)$ are the one electron radial wave functions. In our calculations the electron wave functions were calculated using the Hartree-Fock method. The PWBA method can provide good results for ion impact ionization cross sections if the velocity of the incident particle v_1 is larger than the orbital velocity v_i of the ionizing electron. However, for slow collisions, i.e., $v_1 < v_i$, the PWBA model can overestimate cross

sections significantly because it neglects the perturbation by the charged projectile on the target's atomic states, and the influence of internuclear repulsion. Figure 2.2 shows a comparison of experimental data (Richard et al. 1973) and PWBA results for Al K-shell ionization cross sections by He^{+2}. Note that the discrepancies between theory and experiment in the slow collision regime are typically an order of magnitude. We have included two important corrections for PWBA in our calculations to resolve this problem.

Binding Energy and Polarization Effects

The perturbation of the target atomic states by the presence of the charged projectile in the vicinity of the nucleus during the collision leads to a modification of the binding energy and, consequently, the ionization cross section. From first-order perturbation theory, the change in binding energy including polarization for a shell i (with $i = 1s$, $2s$, or $2p$) is (Brandt and Lapicki 1981, Lapicki and Zander 1981, Basbas et al. 1978):

$$\Delta E_i = \frac{2Z_1 E_i}{Z_{2i}\theta_i}(g_i - h_i)\,. \tag{2.8}$$

Here, E_i is the binding energy of the shell i. The effective charge for the ionizing electron is $Z_{2i} = Z_2 - \delta_i$, with $\delta_{1s} = 0.3$ and $\delta_{2s} = \delta_{2p} = 4.15$. The reduced energy is $\theta_i = E_i/(Z_{2i}^2/2n^2)$, where n is the principal quantum number. The quantities g_i and h_i are the binding and polarization functions defined by Lapicki and Zander (1981). In our calculations, the binding and polarization effects were taken into account by using $E_i + \Delta E_i$ as the i-shell binding energy.

Coulomb Deflection

In the semiclassical approximation, the ionization cross section for a projectile moving along the classical hyperbolic orbit in the Coulomb field of the target nucleus can be approximated by taking the cross section calculated for a straight-line path and multiplying it by a correction factor. In our calculation, the Coulomb deflection factor was taken to be (Brandt and Lapicki 1981)

$$C(x) = \begin{cases} 9\,\varepsilon_{10}(\pi x) & \text{for } 1s \text{ and } 2s \text{ shells}\,, \\ 11\,\varepsilon_{12}(\pi x) & \text{for } 2p \text{ shell}\,, \end{cases} \tag{2.9}$$

with

$$x = 2\,d\,q_{0i}\,\zeta_i\,[z_i(1+z_i)]^{-1}$$

and $\zeta_i = 1 + \Delta E_i/E_i$. Here, z_i is the parameter which accounts for the energy-loss effects, d is the half-distance between the collision partners at closest approach, q_{0i} is

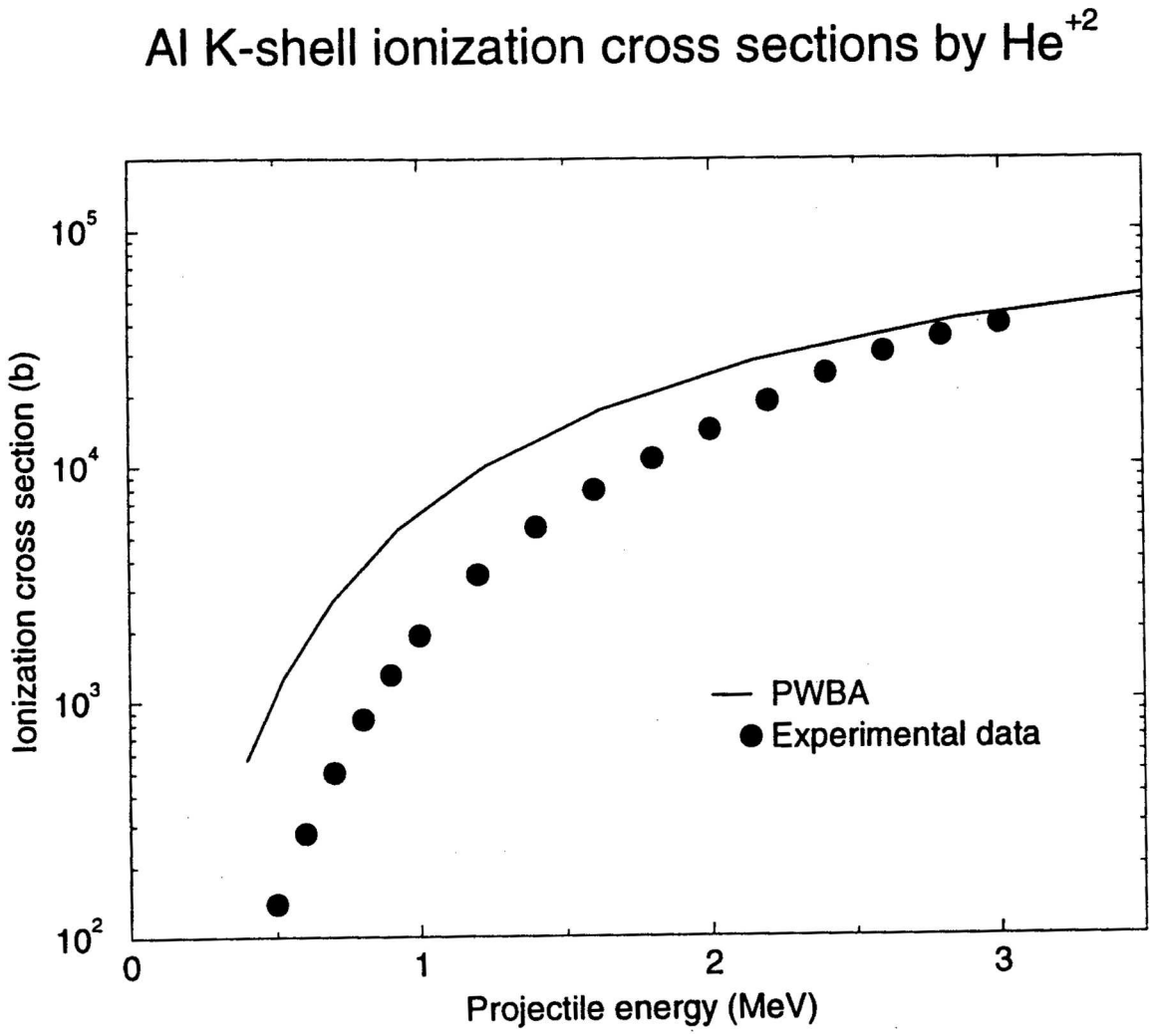

Figure 2.2. Al K-shell ionization cross sections by He^{+2} bombardment. A comparison of PWBA result with experimental data (Richard et al. 1973).

the approximate minimum momentum transfer, and $\varepsilon_n(\pi x)$ is the exponential integral (Abramowitz and Stegun 1965).

With the inclusion of binding, polarization, and Coulomb deflection effects, a significant improvement in the accuracy of the calculated ion impact ionization cross sections is achieved. As shown in Fig. 2.3, the calculated cross sections agree very well with the experimental data over a wider range of projectile energies.

2.2.2. Ionization Probability Model

The ionization cross section, σ_i, can be expressed as the integral of the probability, $P_i(b)$, for single ionization from a shell with N_i electrons, over the impact parameter b

$$\sigma_i(E_1) = N_i \int_0^R 2\pi b P_i(E_1, b) db. \tag{2.10}$$

Here R is the distance at which $P(E_1, b)$ goes to zero. It has been suggested by Kessel and Rudd (1970) that $P(E_1, b)$ can be represented by a step function of the form:

$$P(E_1, b) \begin{cases} \simeq \bar{P}_i(E_1), & b < R, \\ = 0, & b > R. \end{cases} \tag{2.11}$$

Substituting into Eq. (2.10), we have:

$$\bar{P}_i(E_1) = \frac{\sigma_i(E_1)/N_i}{\pi R^2}. \tag{2.12}$$

To deduce average ionization probability, $\bar{P}_i$, from the corresponding ionization cross section, it is critical to have a reasonable estimate for R^2. This has been taken as twice the RMS radius of the i subshell (McGuire and Richard 1973; Hopkins et al. 1973); i.e.,

$$R^2 = 2\langle r_i^2 \rangle \,. \tag{2.13}$$

This procedure has been shown to produce good agreement with experimental data for $\bar{P}_i$ in cases involving light projectiles (McGuire and Richard 1973). However, fundamental difficulties arise with the theory for higher-Z_1 projectiles or very low Z_2 targets. It is apparent that taking R to be independent of the projectile is not always adequate. For different ion-atom collision systems R should be different. If we consider R as an effective interaction radius within which the electrons in the ith shell can interact with the projectile, it can be expected that this effective interaction radius will be larger as the nuclear charge of projectile increases. From the point of view of polarization, R

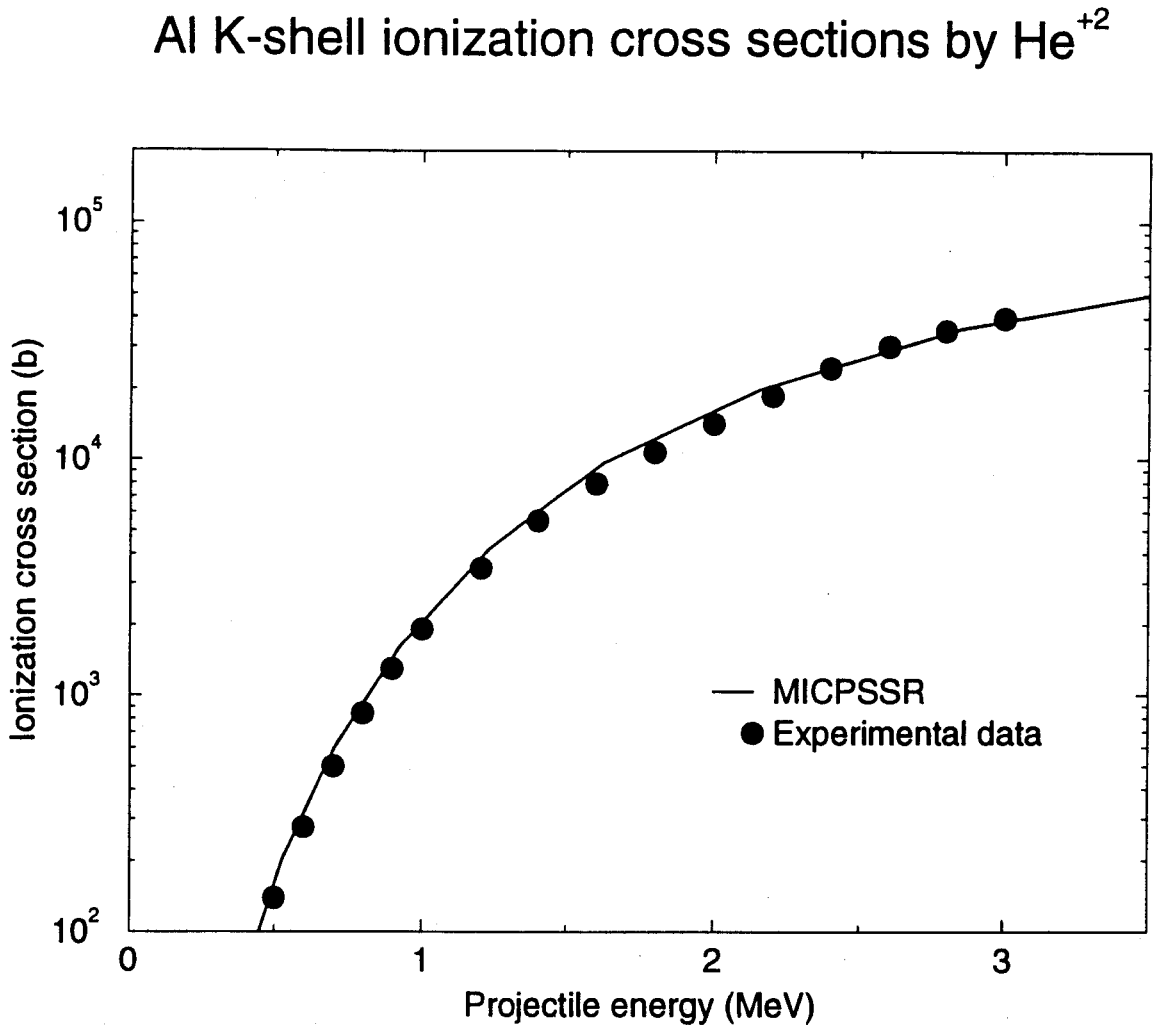

Figure 2.3. Al K-shell ionization cross sections by He^{+2} bombardment. A comparison of MICPSSR results with experimental data.

should increase as Z_1/Z_2 or v_i/v_1 increase. In accordance with our numerical tests, we have found that the following empirical expression for R leads to much better overall agreement with experimental data for a wide range of projectile energies and projectile-target combinations:

$$R^2 = 2\sqrt{\frac{22Z_1}{Z_2}}\sqrt{\frac{v_i}{v_1}}\langle r_i^2\rangle\,. \tag{2.14}$$

Here, the numerical factor 22 is the atomic number of Ti. Hopkins et al. (1973) found that good agreement with experimental data for $\bar{P}_L$ was achieved in applying Eq. (2.13) for the collision system of p + Ti with $v_i/v_1 \approx 1$. Hence we have taken $Z_2/Z_1 = 22$ as a reference.

2.2.3. Multiple Ionization Cross Sections

Assuming that the electrons of the target atom are mutually independent, the cross section for simultaneous production of one K-shell and i $2s$-shell and j $2p$-shell vacancies can be expressed as (McGuire and Richard 1973):

$$\sigma^I_{K,ij} = N_K \int_0^{R_K} 2\pi b P_K(b) P_{ij}(b) db\,, \tag{2.15}$$

where $P_K(b)$ and $P_{ij}(b)$ are the probabilities for single K-shell and multiple L-shell ionization, respectively. The total number of the L-shell vacancies produced is $i+j=m$. R_K is the distance at which $P_K(b)$ goes to zero. It has been shown (Hansteen and Hosebekk 1972; Watson et al. 1983) that a binomial distribution can be used to describe the probability of multiple ionizations in target atoms. For the L shell, we have:

$$P_{ij}(b) = C_2^i[P_{2s}(b)]^i[1-P_{2s}(b)]^{2-i}C_6^j[P_{2p}(b)]^j[1-P_{2p}(b)]^{6-j}\,, \tag{2.16}$$

where $P_{2s}(b)$ and $P_{2p}(b)$ are the probabilities of single ionization from the $2s$ and $2p$ shells, respectively, for an impact parameter b. The quantities C_m^n are binomial coefficients.

It is assumed that over the region of $b \le R_K$, where $P_K(b)$ is nonzero, the probabilities $P_{2s}(b)$ and $P_{2p}(b)$ are flat. This is a reasonable assumption because $R_K \ll R_{2s}$, R_{2p}. We then have

$$\begin{aligned}\sigma^I_{K,ij} &= N_K P_{ij}(0)\int_0^{R_k} 2\pi b P_K(b) db \\ &\simeq P_{ij}(0)\sigma^I_K\,.\end{aligned} \tag{2.17}$$

Thus, the multiple ionization cross section for $K1Lm$ is simply reduced to the product of the single K-shell ionization cross section and the zero impact parameter ionization

probability. Both the single ionization cross section and the zero impact parameter ionization probability can be evaluated using the procedures discussed in previous sections.

2.3. MICPSSR Benchmark Calculations

We have performed a series of benchmark calculations to test the multiple ionization model described above. The primary purpose of the calculations was to assess the accuracy of MICPSSR for single and multiple ionization cross sections.

Three sets of calculations of single ionization cross sections have been performed and compared with experimental data (Datz et al. 1974; Hopkins et al. 1976). The results are shown in Fig. 2.4 through Fig. 2.6. In these calculations, relativistic Hartree-Fock wavefunctions were used for heavy target ions like Au. For the collision process of $F^{+9} \rightarrow Ar$, the inner-shell electron capture effects, i.e.,

$$F^{+9} + Ar\,(1s^2 2s^2 2p^6 3s^2 3p^6) \rightarrow F^{+8}(1s^1) + Ar^{+1}\,(1s^1 2s^2 2p^6 3s^2 3p^6)\,,$$

have been found to be important and were included in our calculations. It can be seen that our calculations are in good agreement with the total single ionization cross sections for a wide range of projectile energies and various projectile-target combinations.

In Table 2.1, the ionization probabilities of $2p$ electrons for various targets by different projectiles are listed. Our calculated results are compared with experimental data (Kauffman et al. 1973) and results of the binary-encounter approximation (BEA) and semi-classical-approximation (SCA) models (Hansteen and Hosebekk 1972). It is clear that our results give better agreement with the experimental data than those of BEA and SCA methods. The accuracy of L-shell ionization probabilities is very critical for the prediction of multiple ionization cross sections of type $K1Lm$. A small error in $P_L(0)$ is greatly magnified when computing cross sections for which many electrons are ejected. We believe that our preditions of subshell ionization probabilities (i.e., the single ejection probabilities) for light ion encounters with intermediate-Z targets should be accurate to a few tens of percent.

Using the calculated single K-shell ionization cross sections and L-shell ionization probabilities, the cross sections for multiple ionization processes of type $K1Lm$ are readily obtained from Eq. (2.16). Figure 2.7 compare calculated and experimental multiple ionization cross sections for He^{+2} on a cold Al target as a function of the projectile energy. It can be seen that the calculated results compare quite well with experiment.

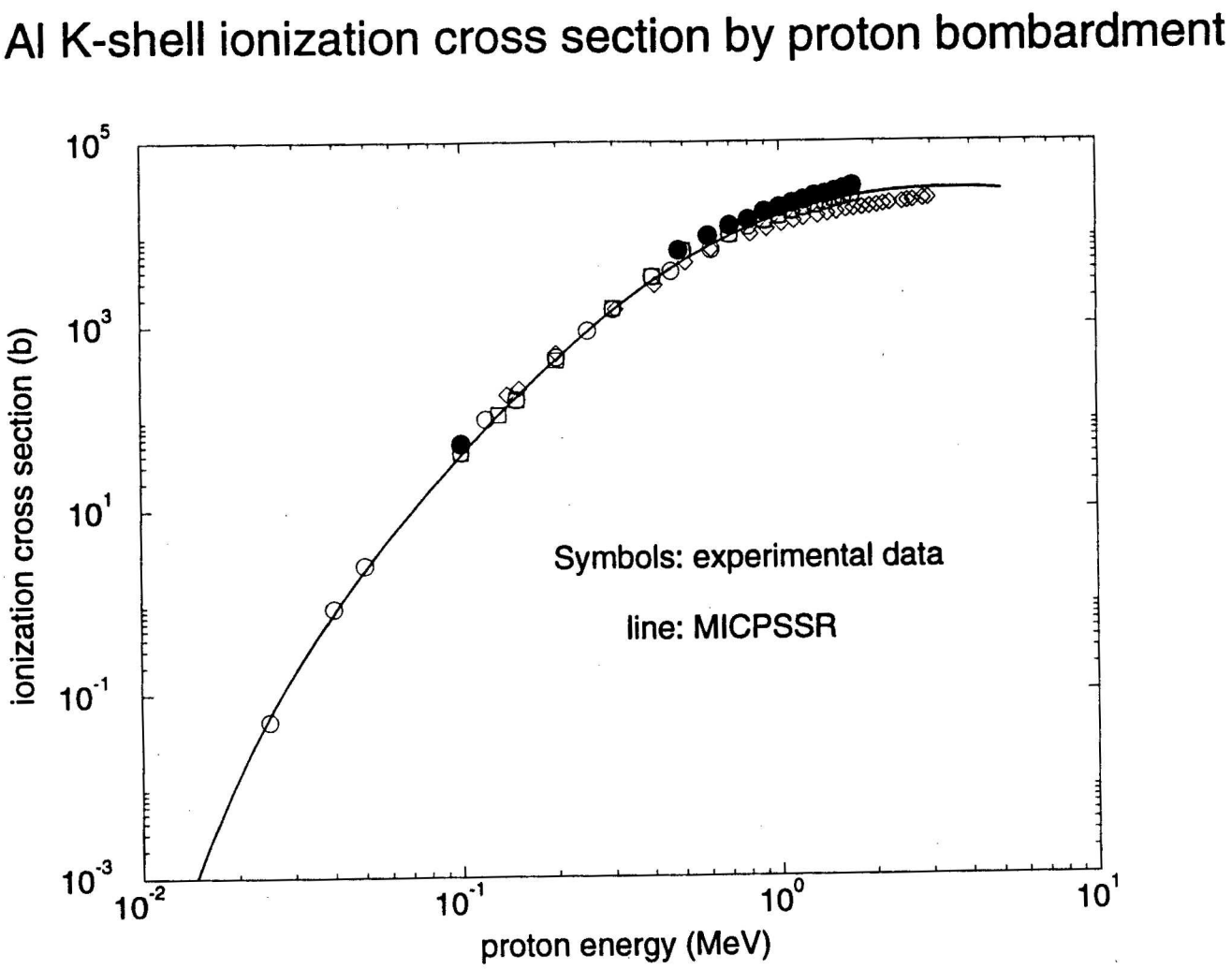

Figure 2.4. Al K-shell ionization cross sections by proton bombardment. A comparison of MICPSSR results with experimental data.

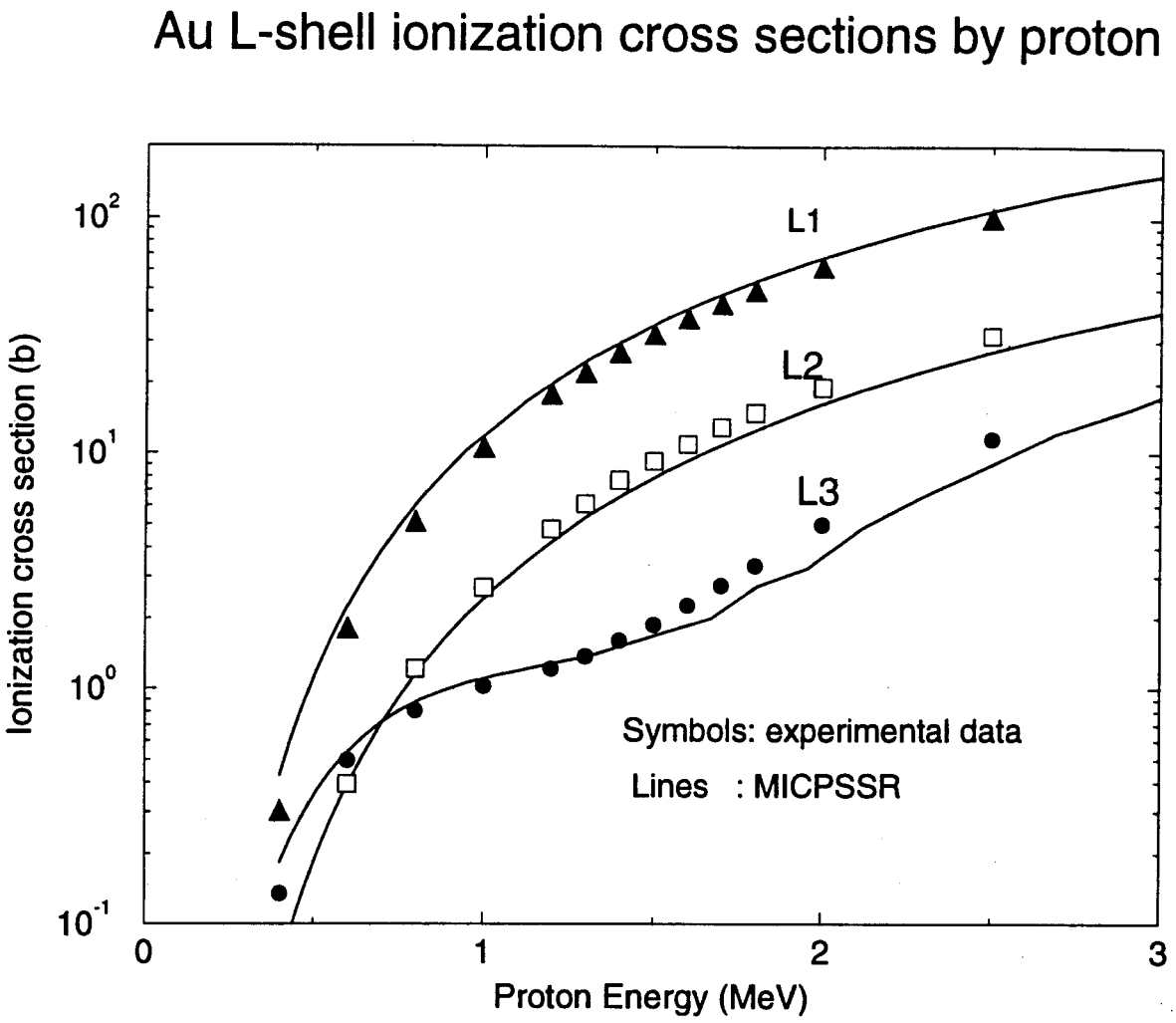

Figure 2.5. Au L-shell ionization cross sections by proton bombardment. A comparison of MICPSSR results with experimental data.

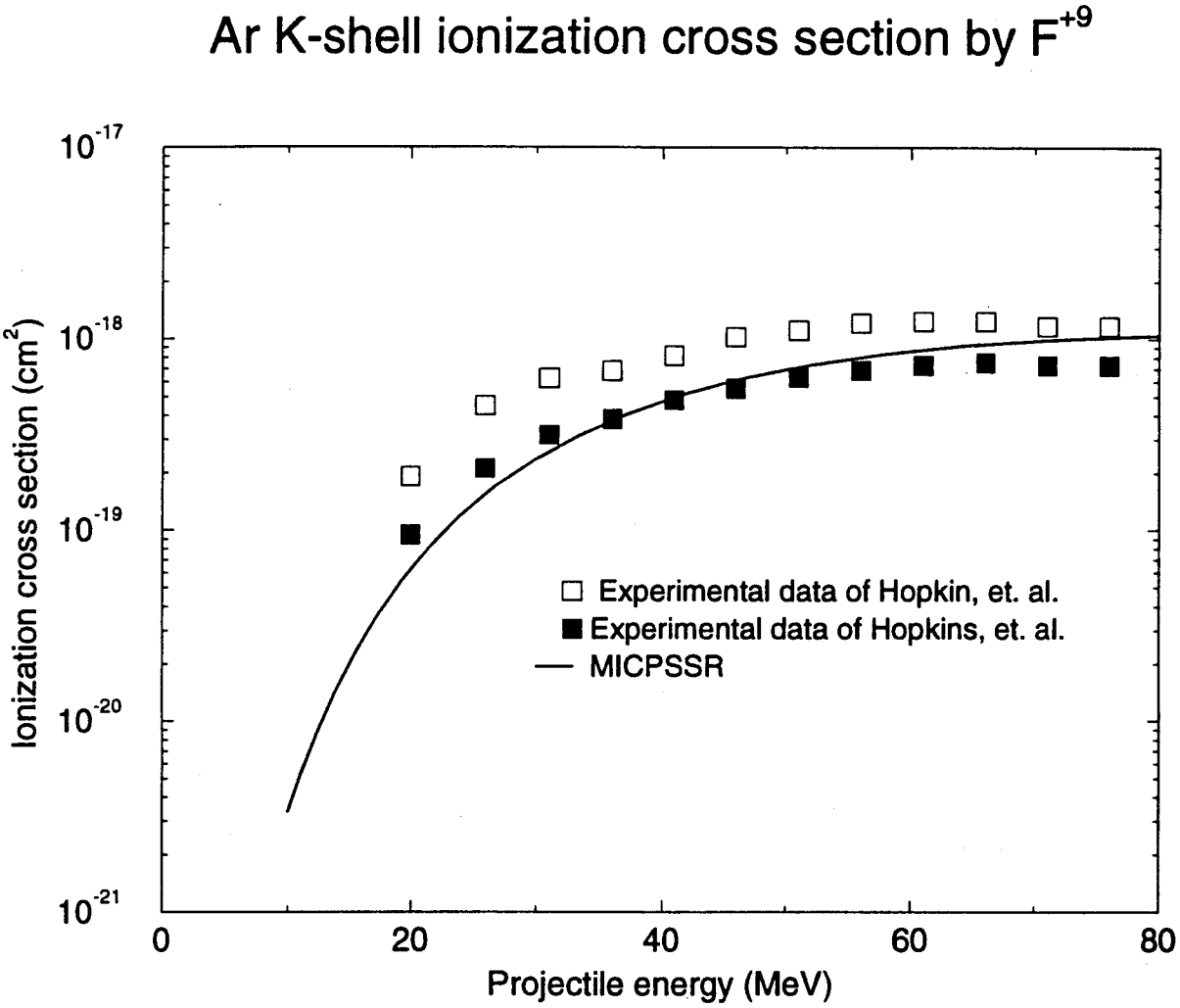

Figure 2.6. Ar K-shell ionization cross sections by F^{+9} bombardment. A comparison of MICPSSR results with experimental data.

Table 2.1. Comparison of Experimental and Calculated $P_L(0)$

Element	Experiment	Calculation	BEA	SCA
		(0.8 MeV Proton)		
Ca	0.012	0.012	0.013	0.019
Sc	0.011	0.011	0.011	0.021
Ti	0.0093	0.0093	0.0093	0.0203
V	0.0054	0.0070	0.0079	0.0195
Cr	0.0040	0.0061	0.0067	0.0193
Mn	0.0028	0.0033	0.0057	0.0189
		(3.2 MeV α Particle)		
Al	0.13	0.12	0.15	—
Ca	0.044	0.039	0.054	0.0795
Sc	0.038	0.033	0.044	0.084
Ti	0.031	0.027	0.037	0.081
V	0.025	0.023	0.030	0.078
Cr	0.018	0.019	0.027	0.077
Mn	0.010	0.016	0.023	0.076
		(30 MeV O^{+5})		
Al	0.033	0.06	0.13	—
Ca	0.29	0.30	0.92	0.44
Sc	0.28	0.27	0.80	0.53
Ti	0.27	0.25	0.72	0.52
V	0.25	0.23	0.63	0.54
Cr	0.24	0.21	0.56	0.55
Mn	0.23	0.20	0.49	0.54

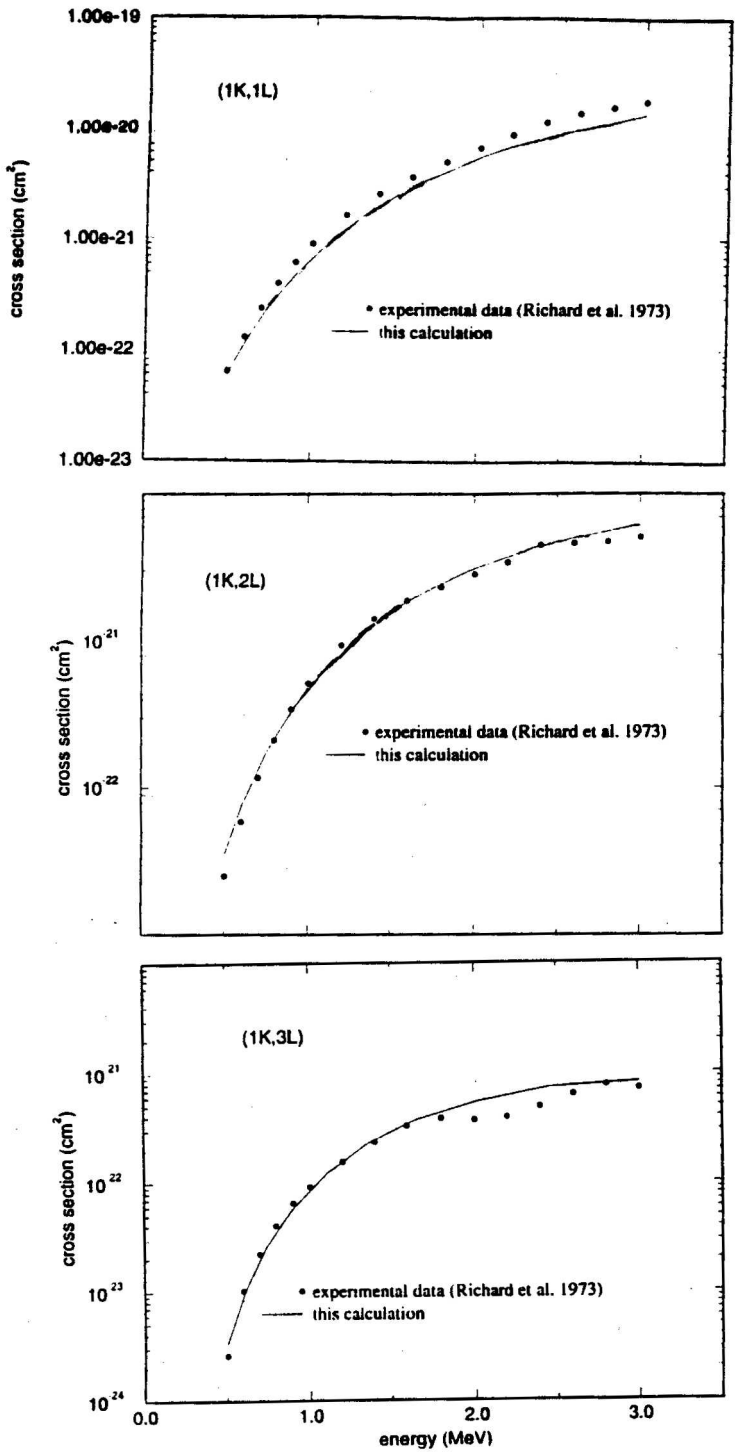

Figure 2.7. Al inner-shell multiple ionization cross sections by He^{+2} bombardment. A comparison of MICPSSR results with experimental data.

$K1L0$ represents the single K-shell ionization process, $K1L1$ represents the ionization of one K-shell electron and one L-shell electron, $K1L2$ represents the ionization of one K-shell electron and two L-shell electrons, and so forth. In Fig. 2.8, the BEA cross sections calculated by J.H. McGuire (1973) are compared with experimental data. It is apparent that our calculated cross sections agree better with the experimental data than those of BEA calculations. The theoretical curves from BEA calculations do not agree well with the data, but they do span the same orders of magnitude and have the same approximate shape.

2.4. Effects of Multiple Ionization in Al Targets Irradiated by Intense Li Beams

Using MICPSSR we have performed calculations for the recent Li beam-Al target experiments on PBFA-II. The results are meant to give some feeling for how multiple ionization events might have influenced the observed K_α spectra. The relative intensities of different satellite lines in the figures shown in this section are weighted by the ionization cross sections and the corresponding fluoresence yields, namely

$$I(Lm : a \rightarrow b) \; = \; \sigma_{K1Lm}\, \omega(a \rightarrow b). \tag{2.18}$$

Hence the influence of multiple ionization is present in the relative intensities of the stick spectra shown below. It should be mentioned that the line positions in the figures are not accurate because only configuration-averaged atomic levels are considered in these calculations. The symbol Lm refers to configurations with m vacancies in the L-shell.

Figures 2.9 through 2.11 show the influence of various effects on multiple ionization. These effects are: (1) target ionization state, (2) projectile charge state, and (3) projectile energy.

For the Li beam-irradiated Al targets in recent PBFA-II experiments, the lower ionization stages of Al quickly disappear as the plasma temperature increases. The strongest lines from higher ionization state Al, i.e., from Ne- through He-like Al, come from electronic configurations of the type $1s^1 2s^r 2p^t$. It is suspected that multiple ionization processes may be less important for the higher ionization stages of Al because the binding energy increases. In order to study the dependence of multiple ionization processes on target ionization states, we have calculated K_α stick spectra for Al I-Al XI with line intensities defined by Eq. (2.18). The calculated results are shown in Fig. 2.9. For Al I-IV, the predominant peak occurs at L1 or L2; that is, a K-shell ejection plus 1 or

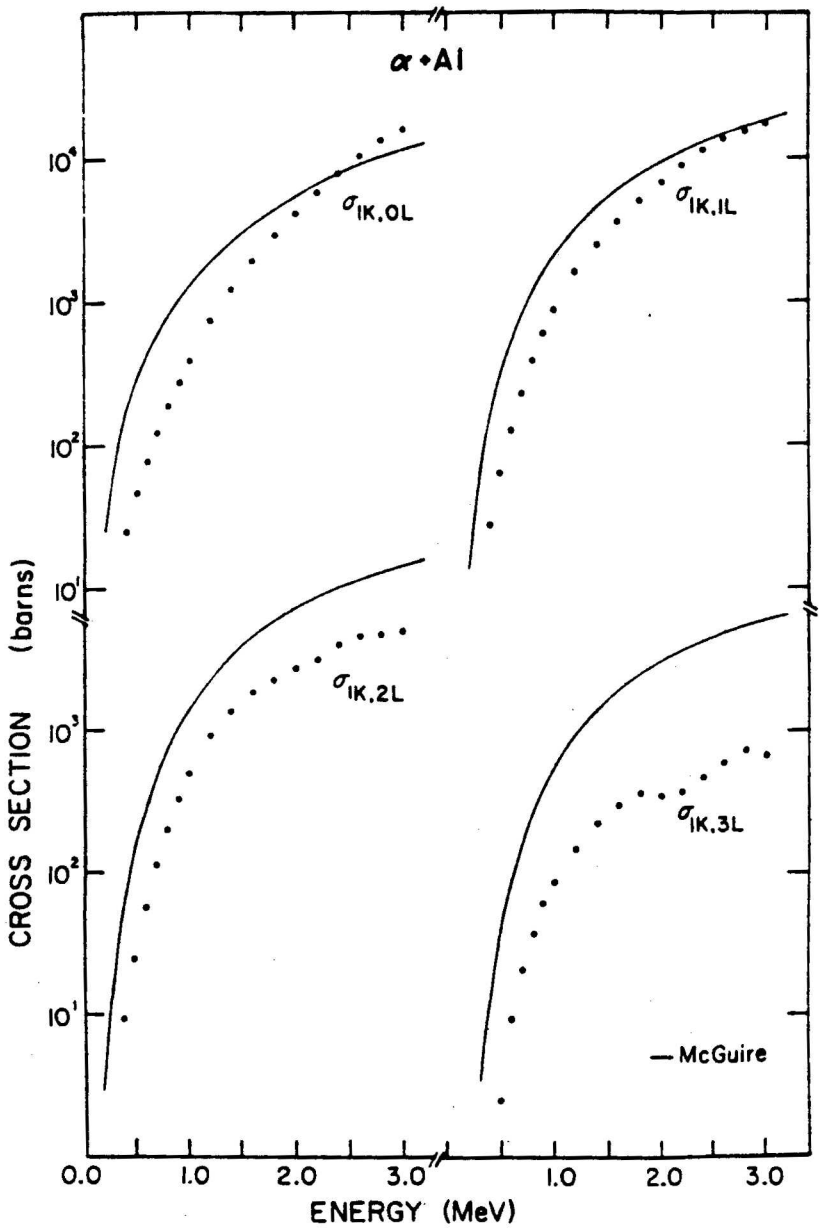

Figure 2.8. Al inner-shell multiple ionization cross sections by He^{+2} bombardment. A comparison of BEA results with experimental data.

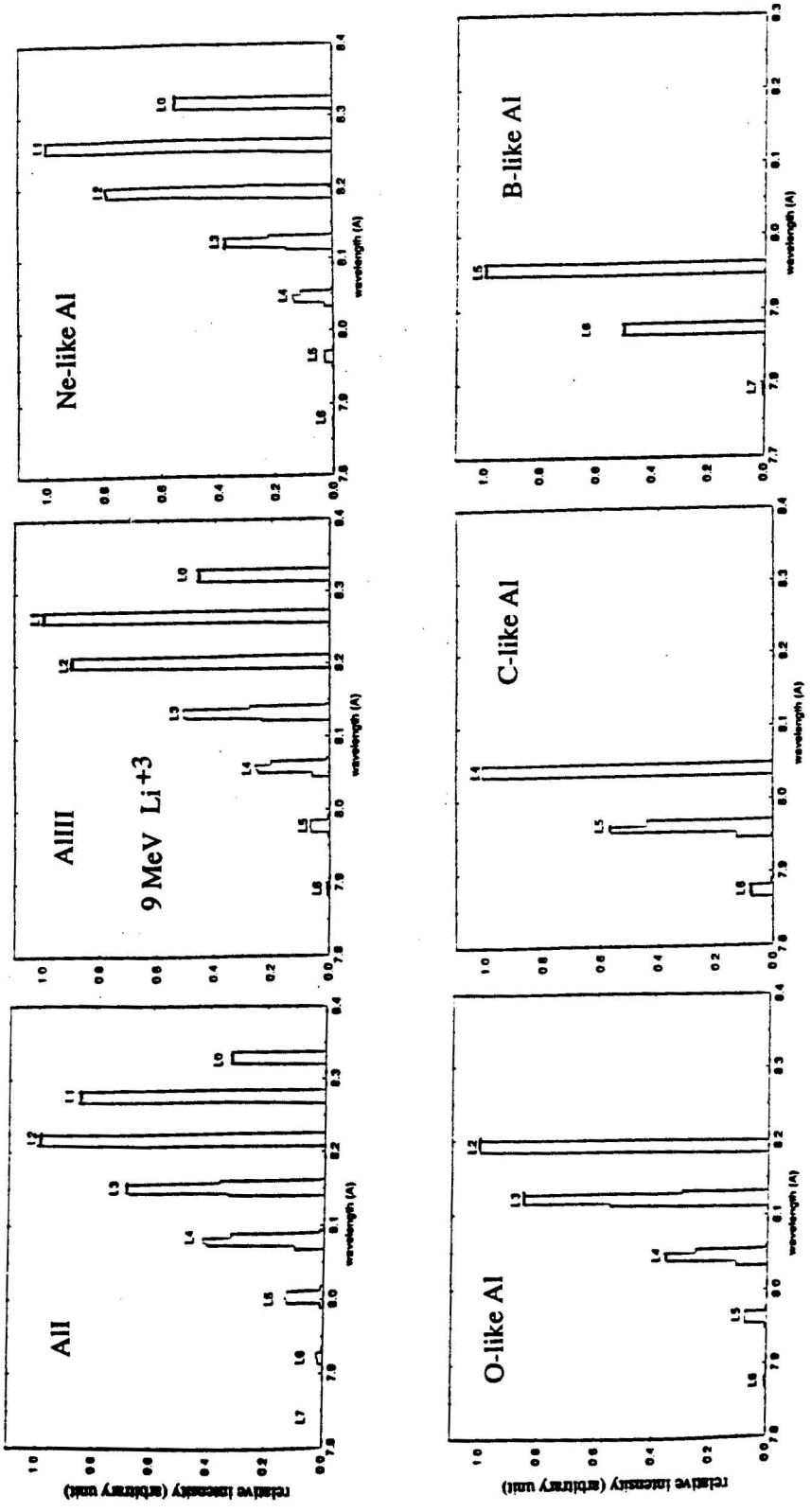

Figure 2.9. Inner-shell multiple ionization cross sections of Al I-Al IX (B-like) by Li^{+3} bombardment calculated using MICPSSR.

2 L-shell ejections. For O- and C-like Al, the single K-shell ejection at L2 (O-like ground configuration) and L4 (C-like ground configuration) dominates. The multiple ionization processes become less important as target ionization state increases. However, even for B-like ions (with ground electronic configuration $1s^2 2s^2 2p^1$) multiple ionization effects cannot be totally discounted.

Figure 2.10 shows the dependence of multiple ionization on the projectile charge state. In these calculations, we have assumed that the nuclear charge of the projectile is completely screened by the bound electrons. This assumption may not be adequate because the screening of the bound electron to the nucleus is never complete. However, the trend is qualitatively correct; i.e., multiple ionization becomes more important as the projectile charge state increases. Figure 2.11 shows the sensitivity to the beam energy. For the energy range of interest the relative importance of multiple ionization decreases as the energy increases. This effect was also noted by Watson et al. (1983) for Ne "targets".

To conclude, multiple ionization processes become *less* important for: (1) more energetic beams, (2) lower charged projectiles, and (3) more highly ionized target atoms.

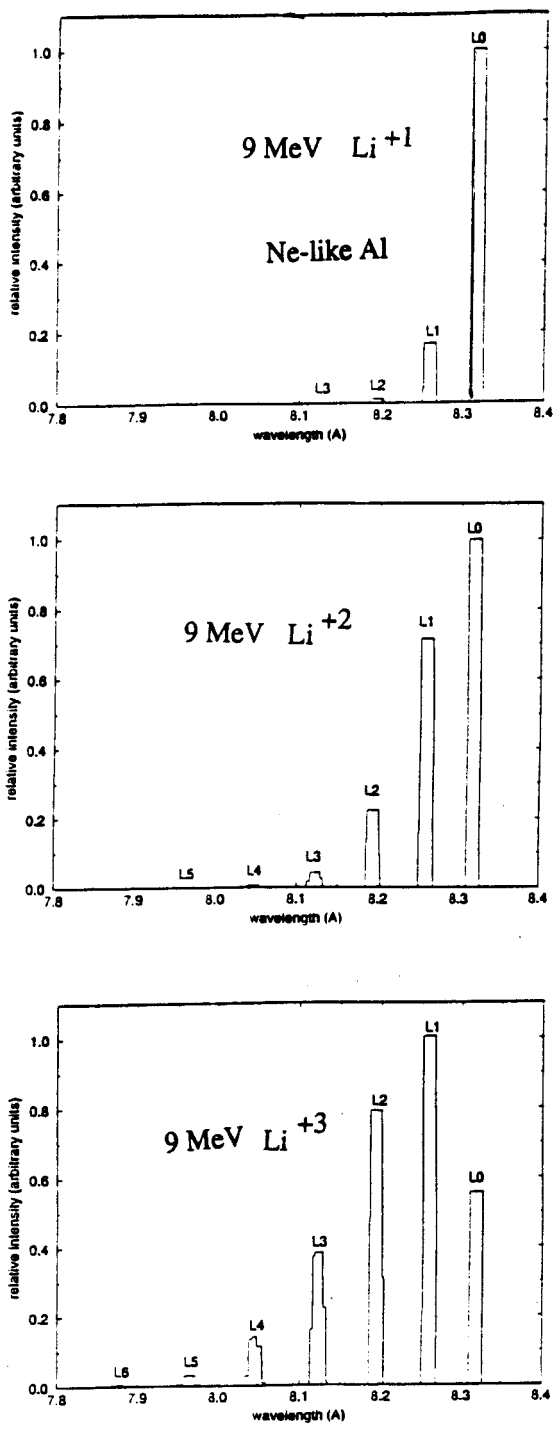

Figure 2.10. Inner-shell multiple ionization cross sections of Ne-like Al by Li^{+3}, Li^{+2}, Li^{+1} bombardment.

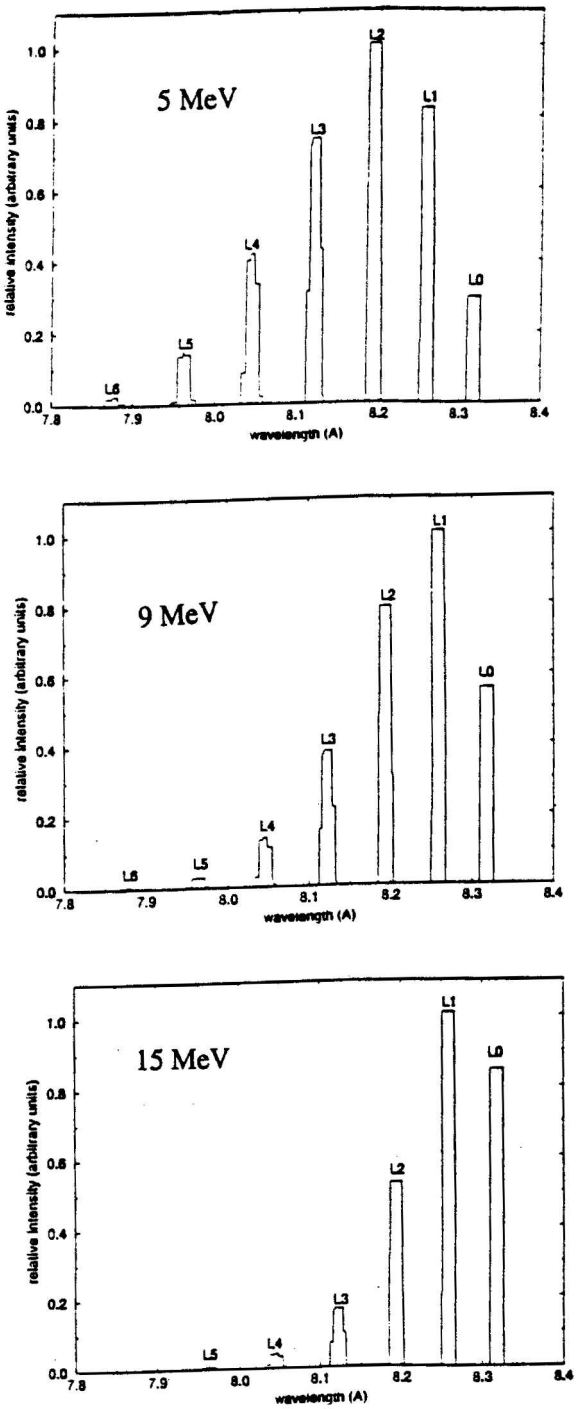

Figure 2.11. Inner-shell multiple ionization cross sections of Ne-like Al by Li^{+3} bombardment ($E_{projectile}$ = 5 MeV, 9 MeV, and 15 MeV).

Section III

Term-Dependent K-Shell Auger Rates and Fluorescence Yields for Aluminum Ions

3.1. Introduction

Term-dependent K-shell Auger transition rates, radiative transition rates, and fluorescence yields in aluminum ions with electronic configurations of type $1s^1 2s^q 2p^r 3l^t$ have been calculated using a Hartree-Fock model. Eleven aluminum ions from Mg-like to He-like were considered.

Accurate K-shell Auger rates, radiative rates, and fluorescence yields are critical for the interpretation of observed K_α satellite spectra. It has been shown (McGuire 1974) that for an ion with an inner-shell hole and a partially filled outer shell, the Auger and radiative decay rates and the fluorescence yield of the autoionizing state can differ by orders of magnitude among various LS terms of a given initial hole electronic configuration. In the case of multiply ionized ions, for which experimental data is often not available, theoretical calculations are essential. Some calculations of term-dependent Auger and radiative rates and fluorescence yields for intermediate-Z ions have been carried out previously (Chen et al. 1981; Bhalla 1975; Chen and Crasemann 1975; Combet Farnoux 1985). However, to our knowledge no systematic calculations have been performed for aluminum ions with electronic configurations of the general type $1s^1 2s^q 2p^r 3l^t$ ($q \geq 0$, $r \geq 1$, and $t \geq 0$). Here we report on calculations of term-dependent K-shell Auger and radiative rates and fluorescence yields for all terms of electronic configurations of type $1s^1 2s^q 2p^r 3l^t$ of aluminum ions from Al II to Al XII.

3.2. Theoretical Approach

The Auger rate for the transition from an initial state, i, with a $1s$ hole to the final state, f, is based on the following formulations (Cowan 1981):

$$\Gamma_A(\gamma_i, 1s, \epsilon l_4, L'S' \rightarrow \gamma_f, n_1 l_1, n_2 l_2, LS) = 2\pi \sum | < i|1/r_{12}|f > |^2 \qquad (3.1)$$

and

$$< i|1/r_{12}|f >= \sum_k x_k R^k(1s, \epsilon l_4; n_1 l_1, n_2 l_2|r), \qquad (3.2)$$

where Γ_A is Auger rate in atomic units, the transition $(1s, \epsilon l) \rightarrow (n_1 l_1, n_2 l_2)$ refers to the exchange of holes between initial and final states, x_k is a coefficient related to the angular

momentum coupling and can be expressed with $3j$ and $6j$ symbols, and the $R^k(r)$ are radial integrals defined as follows:

$$R^k(l_1 l_2 l_3 l_4) = \int_0^\infty \int_0^\infty \frac{r_<^k}{r_>^{k+1}} P^*_{n_1 l_1}(r_i) P^*_{n_2 l_2}(r_j) P_{n_3 l_3}(r_i) P_{\epsilon l_4}(r_j) dr_i dr_j. \tag{3.3}$$

Radial wavefunctions $P_{nl}(r)$ were calculated by solving the Hartree-Fock equations. The continuum wavefunction $P_{\epsilon l}(r)$ is normalized to $\delta(\epsilon - \epsilon')$.

The radiative transition probability for an electric dipole allowed transition $i \to f$ is given by

$$\Gamma_R(\gamma_i, n_i l_i, L_i S_i \to \gamma_f, n_f l_f, L_f S_f) = \frac{4\Delta E^3 \alpha^3}{3(2L+1)} | < \gamma_i, L_i S_i || T^{(1)} || \gamma_f, L_f S_f > |^2 . \tag{3.4}$$

Here, Γ_R is the radiative transition rate in atomic units, ΔE is transition energy in $2Ry$, α is the fine structure constant, and $< i||T^{(1)}||f >$ is the reduced matrix element:

$$| < \gamma_i L_i S_i || T^{(1)} || \gamma_f L_f S_f > |^2 = \bar{S}(\gamma_i L_i S_i - \gamma_f L_f S_f) l_> | \int_0^\infty P_{n_i l_i}(r) P_{n_f l_f}(r) r dr |^2. \tag{3.5}$$

The reduced multiplet strength $\bar{S}$ in Eq. (3.5) is an angular factor which depends on the transition type. A general formula for the evaluation of $\bar{S}$ under LS coupling representation is given in Cowan (1981).

LS term-dependent fluorescence yields, $\omega(LS)$, were calculated using the following definition:

$$\omega(\gamma LS) = \frac{\sum_f \Gamma_R(\gamma LS \to \gamma_f L_f S_f)}{\sum_f \Gamma_R(\gamma LS \to \gamma_f L_f S_f) + \sum_f \Gamma_A(L\gamma S \to \gamma_f L_f S_f)}. \tag{3.6}$$

We have also calculated effective fluorescence yield for each configuration, which is given by:

$$\bar{\omega}(\gamma) = \frac{\sum_{L,S}(2L+1)(2S+1)\omega(\gamma LS)}{\sum_{L,S}(2L+1)(2S+1)}. \tag{3.7}$$

3.3. Results and Discussion

We have calculated term-dependent K-shell Auger and radiative transition rates and fluorescence yields for aluminum ions with electronic configurations of type $1s^1 2s^q 2p^r 3l^t$ ($q \geq 0$, $r \geq 1$, and $t \geq 0$). Some of our calculated results are listed in Table 3.1 and compared with the theoretical results of Combet Farnoux (1985). It can be seen that two sets of data are in good agreement. We have also compared our

calculated results with other available theoretical results (Bhalla 1975; Chen et al. 1981), and good agreement is generally found except for the terms for which Auger or radiative decay channels are closed in LS coupling. It is important to note that some of the closed Auger or radiative decay channels in LS-coupling can be open channels in intermediate coupling. In such cases the pure LS coupling is not valid and the states should be expressed in intermediate coupling. In Table 3.2 we list partial Auger rates, radiative decay rates, term-dependent fluorescence yields, and effective configuration fluorescence yields for all terms of electronic configurations of type $1s^1 2s^q 2p^r$. These configurations are believed to be the most important contributors to the Al K_α spectra measured in recent PBFA-II experiments. It should be noted that the values of the fluorescence yield depend sensitively on the multiplicity $(2S+1)$ and the orbital angular momentum value (L) of a term for a specific electronic configuration. For the data listed in Table 3.2, the Auger rates or radiative decay rates are zero for the terms with closed Auger or radiative decay channels in LS coupling. For the light elements like aluminum, these rates may be non-zero, but typically have values three or four orders of magnitude smaller than those of open channels.

Table 3.1. Term-dependent Auger, Radiative Transition Rates and Fluorescence Yields for $1s^1\,2s^2\,2p^r$ of Al

Configuration	LS	Auger Rate*	Radiative Rate*	$\omega_K(LS)$	$\omega_K(LS)$ (Combet Farnoux)
$1s^1\,2s^2\,2p^6$	^2S	130.05	6.26	0.0459	0.0462
$1s^1\,2s^2\,2p^5$	^1P	103.99	8.95	0.0793	0.0814
	^3P	113.67	4.53	0.0383	0.0393
$1s^1\,2s^2\,2p^4$	^2S	89.50	4.88	0.0517	0.0543
	^2P	73.16	9.63	0.1164	0.1258
	^4P	88.71	2.46	0.0270	0.0290
	^2D	102.48	4.86	0.0453	0.0475
$1s^1\,2s^2\,2p^3$	^3S	31.53	10.37	0.2474	0.3152
	^5S	52.36	0.0	0.0	0.0
	^1P	59.80	7.77	0.1149	0.1283
	^3P	71.38	2.65	0.03578	0.0397
	^1D	69.10	12.59	0.1541	0.1112
	^3D	81.21	2.63	0.0314	0.0347
$1s^1\,2s^2\,2p^2$	^2S	48.55	2.836	0.05518	0.0654
	^2P	27.51	8.309	0.2320	0.308
	^4P	45.25	0.0	0.0	0.0
	^2D	64.48	2.815	0.04184	0.0482

*In multiples of 10^{-4} a.u., 1 a.u. $= 4.134 \times 10^{16}\,s^{-1}$

Table 3.2.

configuration	LS	Auger rate(in a.u.) (K)-(L1L1)	(K)-(L1L23)	(K)-(L23L23)	Total	Radiative rate	omega(LS)	omega(n)
1s**1 2s**2 2p**6								.0459
	2S	12.3896	39.0731	78.5832	130.0459	6.2564	.0459	
1s**1 2s**2 2p**5								.0485
	1P	14.5066	29.9888	59.4917	103.9871	8.9507	.0793	
	3P	13.5511	38.7212	61.4009	113.6732	4.5263	.0383	
1s**1 2s**1 2p**6								.0669
	1S	.0000	4.7670	92.6171	97.3842	6.8365	.0656	
	3S	.0000	.8240	92.5303	93.3543	6.7450	.0674	
1s**1 2s**2 2p**4								.0526
	2S	15.4224	32.4216	41.6589	89.5029	4.8751	.0517	
	2D	15.4029	32.6818	54.3972	102.4818	4.8613	.0453	
	2P	16.5172	22.5533	34.0849	73.1554	9.6388	.1164	
	4P	14.7497	37.7707	36.1931	88.7136	2.4594	.0270	
1s**1 2s**1 2p**5								.0765
	2P	.0000	5.6503	71.5158	77.1661	6.1262	.0736	
	2P	.0000	.9323	70.3095	71.2418	8.6374	.1081	
	4P	.0000	.5172	72.0357	72.5529	4.8106	.0622	
1s**1 2p**6								.0680
	2S	.0000	.0000	99.9598	99.9598	7.2914	.0680	
1s**1 2s**2 2p**3								.0663
	1P	18.1068	18.4557	23.2432	59.8057	7.7697	.1150	
	3P	16.7688	30.0329	24.5743	71.3760	2.6486	.0358	
	1D	18.0954	18.5864	32.4143	69.0961	12.5872	.1541	
	3D	16.7556	30.2493	34.2047	81.2096	2.6306	.0314	
	3S	18.8136	12.7214	.0000	31.5350	10.3652	.2474	
	5S	16.0852	36.2785	.0000	52.3636	.0000	.0000	
1s**1 2s**1 2p**4								.0947
	1S	.0000	6.4500	48.8954	55.3454	5.3018	.0874	
	1D	.0000	6.4582	63.6257	70.0838	5.2821	.0701	
	3P	.0000	6.4859	41.4981	47.9840	5.2485	.0986	
	3S	.0000	.4736	48.8506	49.3241	5.2385	.0960	
	3D	.0000	.4690	63.5688	64.0379	5.2203	.0754	
	1P	.0000	1.0020	39.8679	40.8699	10.8732	.2101	
	3P	.0000	.7264	40.6496	41.3760	7.9493	.1612	
	5P	.0000	.2244	42.3056	42.5299	2.5761	.0571	
1s**1 2p**5								.0783
	1P	.0000	.0000	74.9263	74.9263	10.4009	.1219	
	3P	.0000	.0000	77.1177	77.1177	5.2513	.0638	
1s**1 2s**2 2p**2								.0640
	2S	19.0217	19.8052	9.7273	48.5542	2.8357	.0552	
	2D	19.0052	20.1268	25.3449	64.4768	2.8151	.0418	
	2P	20.5291	6.9815	.0000	27.5106	8.3093	.2320	
	4P	18.2175	27.0349	.0000	45.2524	.0000	.0000	
1s**1 2s**1 2p**3								.1712
	2P	.0000	6.9259	28.3642	35.2901	4.2557	.1076	
	2D	.0000	6.9941	39.3301	46.3242	4.2395	.0838	
	4S	.0000	7.0623	.0000	7.0623	4.1853	.3721	
	2P	.0000	.5230	27.5888	28.1118	7.1300	.2023	
	4P	.0000	.1903	28.7242	28.9145	2.8046	.0884	
	2D	.0000	.5179	38.2872	38.8052	7.1276	.1552	
	4D	.0000	.1884	39.8163	40.0047	2.7839	.0651	
	2S	.0000	.8883	.0000	.8883	11.8316	.9302	
	4S	.0000	.5100	.0000	.5100	7.0906	.9329	
	6S	.0000	.0000	.0000	.0000	.0000	.0000	
1s**1 2p**4								.0966
	2S	.0000	.0000	51.9525	51.9525	5.6443	.0980	
	2D	.0000	.0000	67.6026	67.6026	5.6213	.0768	
	2P	.0000	.0000	43.7644	43.7644	11.1775	.2034	
	4P	.0000	.0000	44.8942	44.8942	2.8399	.0595	
1s**1 2s**2 2p**1								.0516
	1P	22.2330	.3020	.0000	22.5350	5.8584	.2063	
	3P	20.5040	14.9918	.0000	35.4958	.0000	.0000	
1s**1 2s**1 2p**2								.2784
	1S	.0000	6.5023	11.5077	18.0100	3.0714	.1457	
	1D	.0000	6.6550	29.5138	36.1688	3.0436	.0776	
	3P	.0000	6.7642	.0000	6.7642	3.0057	.3076	
	3S	.0000	.1523	11.4957	11.6480	3.0375	.2068	
	3D	.0000	.1460	29.4876	29.6335	3.0122	.0923	
	1P	.0000	.5262	.0000	.5262	9.3723	.9468	
	3P	.0000	.3175	.0000	.3175	6.0984	.9505	
	5P	.0000	.0000	.0000	.0000	.0000	.0000	
1s**1 2p**3								.1600
	1P	.0000	.0000	30.4856	30.4856	8.9013	.2260	
	3P	.0000	.0000	30.2917	30.2917	3.0521	.0915	
	1D	.0000	.0000	41.4972	41.4972	8.9733	.1778	
	3D	.0000	.0000	42.0148	42.0148	3.0276	.0672	
	3S	.0000	.0000	.0000	.0000	11.9632	1.0000	
	5S	.0000	.0000	.0000	.0000	.0000	.0000	
1s**1 2s**1 2p**1								.3113
	2P	.0000	3.7083	.0000	3.7083	1.6163	.3036	
	2P	.0000	.3026	.0000	.3026	4.8723	.9415	
	4P	.0000	.0000	.0000	.0000	.0000	.0000	
1s**1 2p**2								.2458
	2S	.0000	.0000	11.9307	11.9307	3.2630	.2148	
	2D	.0000	.0000	30.9823	30.9823	3.2322	.0945	
	2P	.0000	.0000	.0000	.0000	9.5649	1.0000	
	4P	.0000	.0000	.0000	.0000	.0000	.0000	
1s**1 2p**1								.2500
	1P	.0000	.0000	.0000	.0000	6.7324	1.0000	
	3P	.0000	.0000	.0000	.0000	.0000	.0000	

Section IV

Analysis of Al K_α Spectra Obtained in PBFA-II Lithium Beam Experiments

In recent experiments on PBFA-II, thin planar targets composed of Au and Al were irradiated with intense Li beams. X-ray line emission was detected from Au M-shell and Al K_α lines. One of the objectives of the experiments was to determine whether the observed K_α line radiation was consistent with beam power densities deduced from beam diagnostic measurements. In our analysis of the Al K_α spectrum, we performed CRE calculations to determine Li ion beam-induced K_α line emission using time-dependent temperature and density distributions predicted from SNL radiation-hydrodynamic simulations. Atomic physics calculations were performed to provide a comprehensive database for energy levels, collisional and radiative rate coefficients, beam-induced ionization cross sections, Auger rates, and fluorescence yields.

The models used for the Li/Al analysis were in many respects similar to our analysis of proton beam-induced K_α line emission from Al. Details of the latter have been published elsewhere (MacFarlane et al. 1993; Wang et al. 1993; see also Appendices A and B). Major improvements in regards to the CRE and atomic physics modeling are as follows:

1. Multiple ionization effects, which arise because of the higher charge of the Li projectile, are included. Ion impact ionization cross sections were computed using the model described in Section II. Multiple ionization processes are included in the statistical equilibrium equations as direct transitions between atomic states of non-adjacent ionization stages; i.e., all charge states are coupled together. Ion-impact ionization out of excited states (non-autoionizing levels with M-shell spectator electrons) is also considered.

2. Term-dependent Auger rates and fluorescence yields were computed for all Al ions. This was done because of the significant variations found in fluorescence yields between atomic levels (see Section III; Combet Farnoux 1987), and because of its importance in computing spectral line intensities.

3. Complete collisional coupling for He-like and Li-like ions is included in atomic models for Al and Mg. This was found to be necessary because the collisional

depopulation of metastable states can significantly affect predicted line intensities. For example, the collisional depopulation of the He-like $1s^1\,2p^1\,{}^3P$ state into the $1s^1\,2p^1\,{}^1P$ state results in a significant increase in the He-α line intensity (Duston and Davis 1980). Collisional rate coefficients were computed using a distorted wave (DW) model.

In the recent PBFA-II experiments, planar targets composed of 2000 Å-thick Al and 5600 Å-thick Au were irradiated by a 8 - 10 MeV, 2 - 3 TW/cm^2 Li-beam. The Al and Au layers were sandwiched between 1400 Å-thick CH tampers. A schematic illustration of the target geometry is shown in Fig. 4.1.

X-ray line emission was observed using an elliptical crystal spectrometer with a resolution of $\lambda/\Delta\lambda \approx 1500$ (Bailey et al. 1990). The measured spectra were time-integrated. Figure 4.2 shows the Al K_α satellite spectra observed from Shots 5881 and 5851. K_α satellites are seen for He-like Al ($\lambda = 7.76$ Å) down through cold Al ($\lambda = 8.34$ Å). Roughly speaking, each major peak corresponds to a different ionization stage of Al, but with Al I-IV unresolved. Considerable structure is evident within each of these major features.

To analyze this time-integrated spectrum, we have used the results of 1-D radiation-hydrodynamic simulations performed at Sandia (Dukart and Mehlhorn 1993) to provide time-dependent temperature and density distributions for the Al region. Radiation-hydrodynamic results were provided for two beam power densities: 1 TW/cm^2 and 3 TW/cm^2. Results are shown in Figs. 4.3 and 4.4 for the low and high power density cases, respectively. The different curves correspond to simulation times, in 2 ns intervals, ranging from 12 to 38 ns. Note that the peak temperature is about 39 eV and 26 eV in the 3 and 1 TW/cm^2 cases, respectively. In each case the densities have fallen to roughly 10^{-3} of their solid density value by the time the temperature reaches its peak value.

CRE calculations were performed for each of the simulation times for both the high and low power density cases. The Al atomic models for the CRE calculations consisted of just over 1000 atomic levels distributed over all 14 Al ionization stages. Roughly 600 of these were autoionizing levels. The level energies were determined from configuration interaction (CI) calculations. Collisional (electron impact) and radiative rate coefficients were computed using methods described elsewhere (see Appendix A). Multiple ionization cross sections were calculated using the model described in Section II. To compute the corresponding ion impact ionization rate coefficients, we used the same time-dependent Li

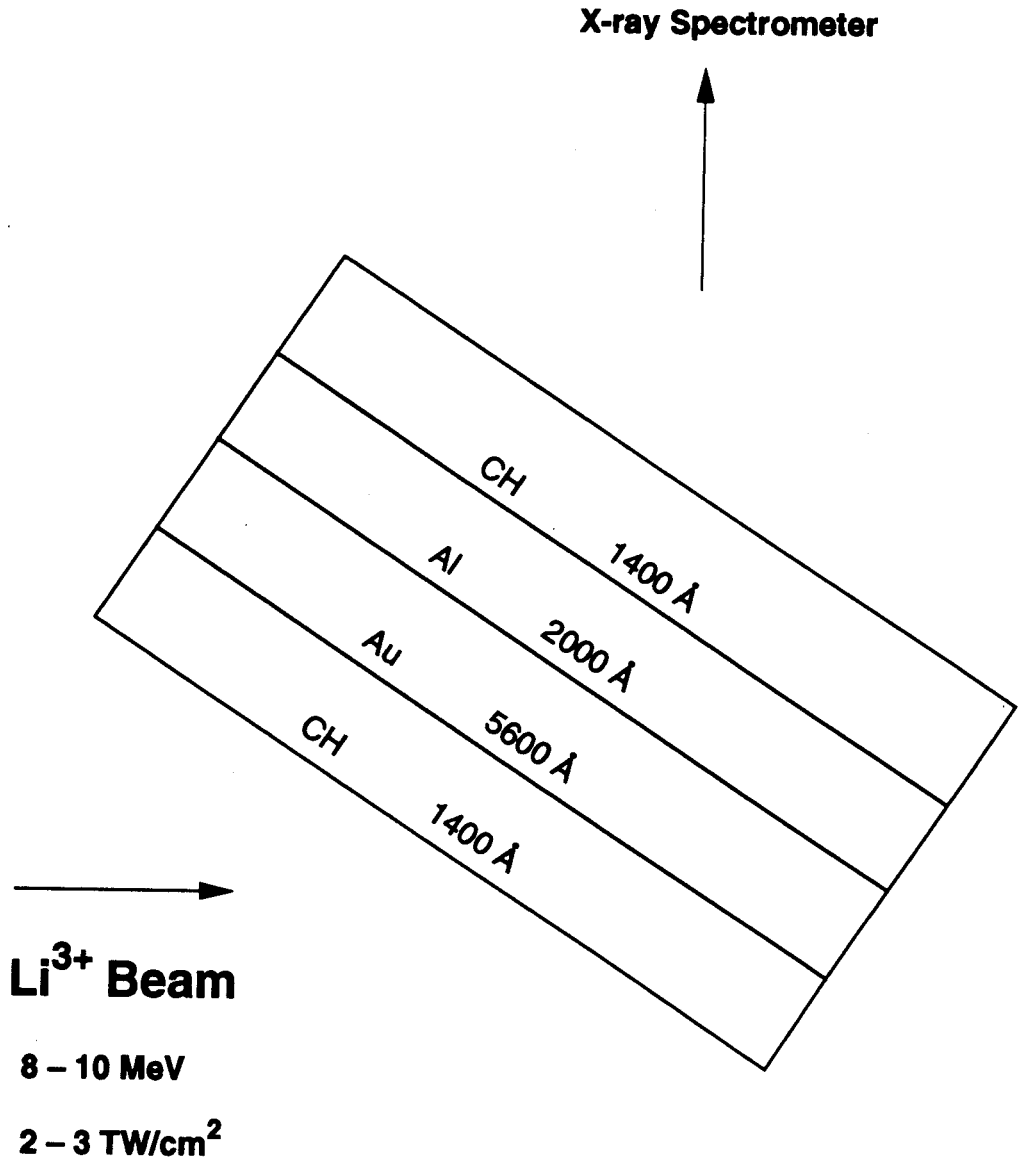

Figure 4.1. Schematic illustration of target geometry in PBFA-II experiment.

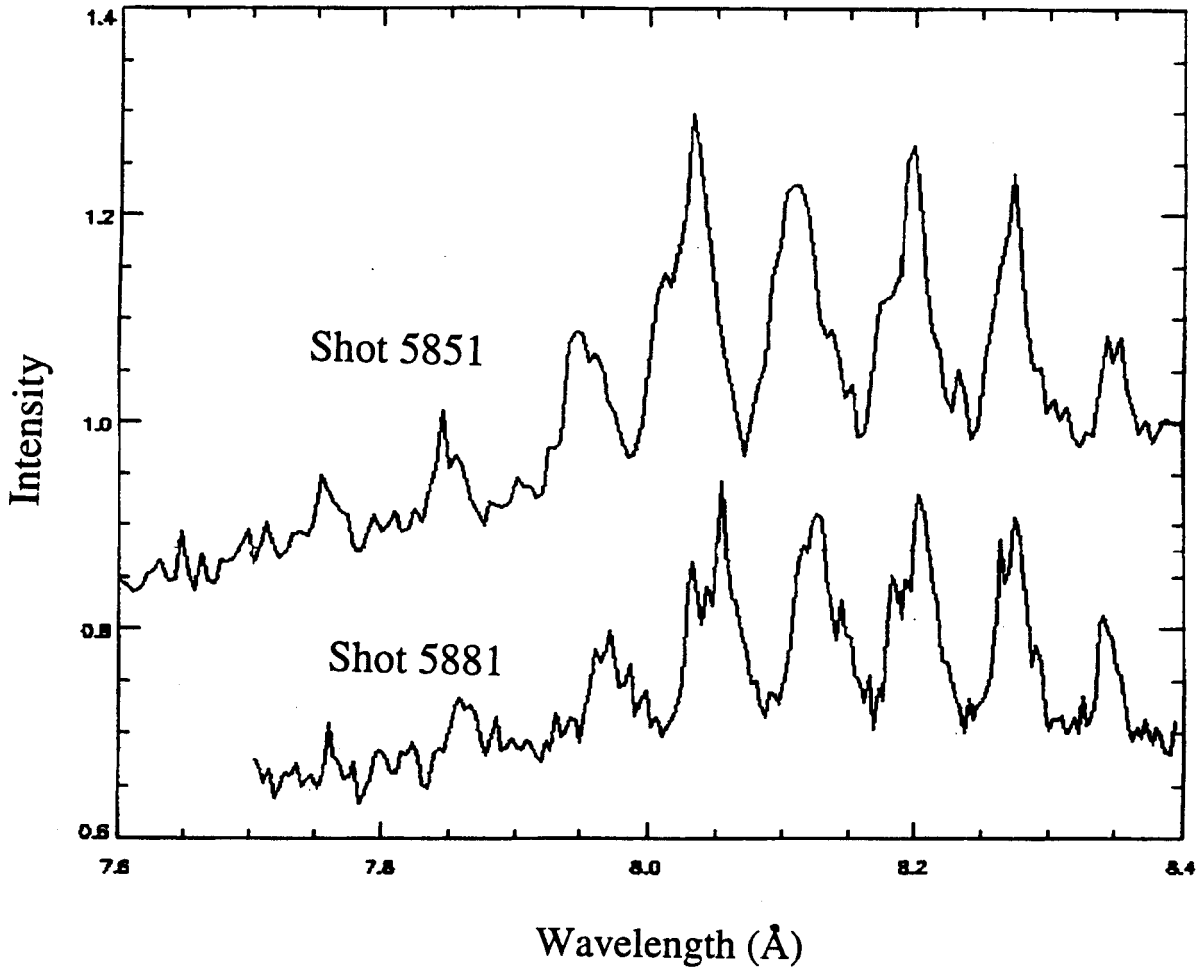

Figure 4.2. Measured Al K_α spectra from Shots 5881 and 5851.

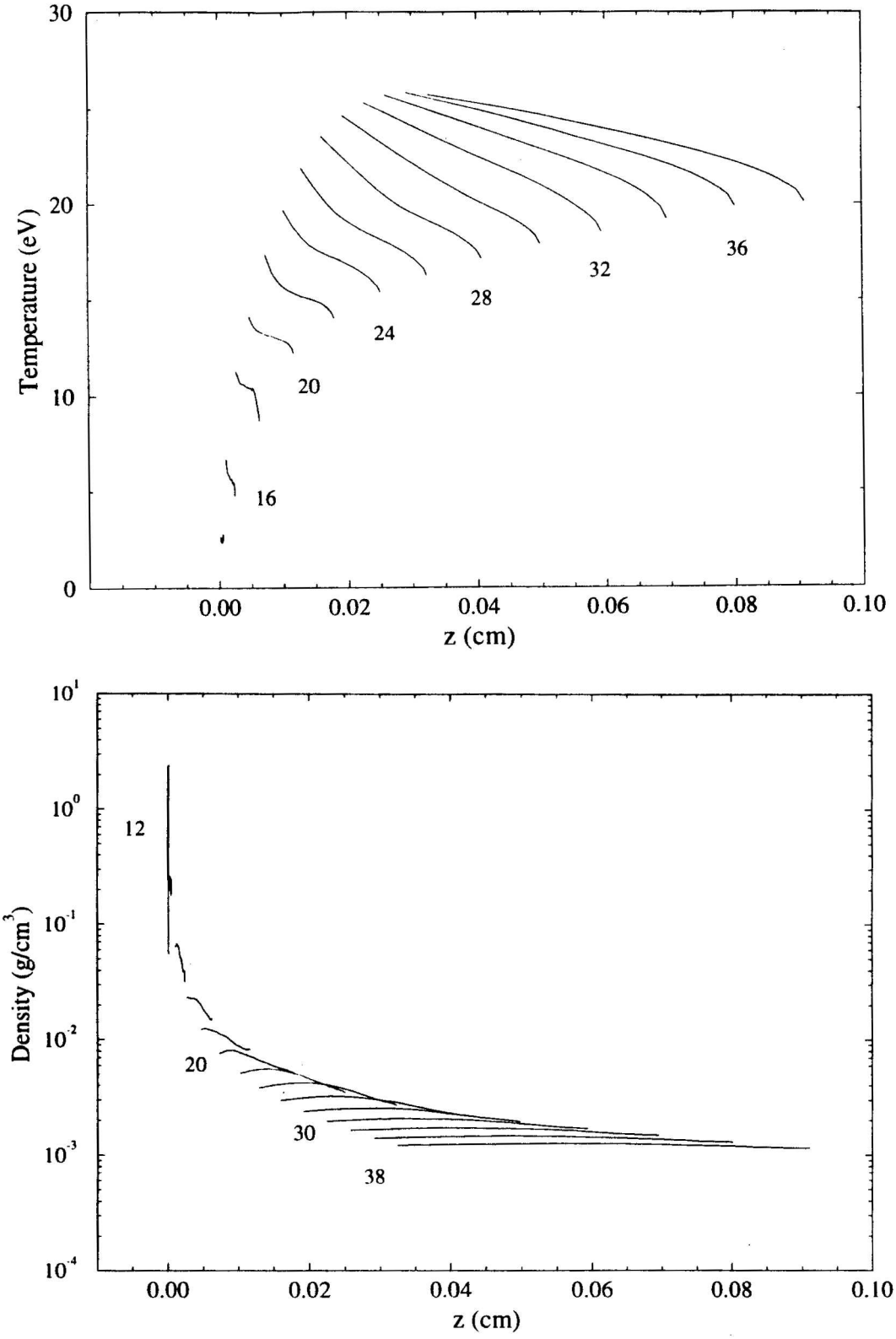

Figure 4.3. Temperature and density distributions from radiation-hydrodynamic simulations for a 1 TW/cm^2 Li beam. The results are given in 2 ns intervals from 12 to 38 ns.

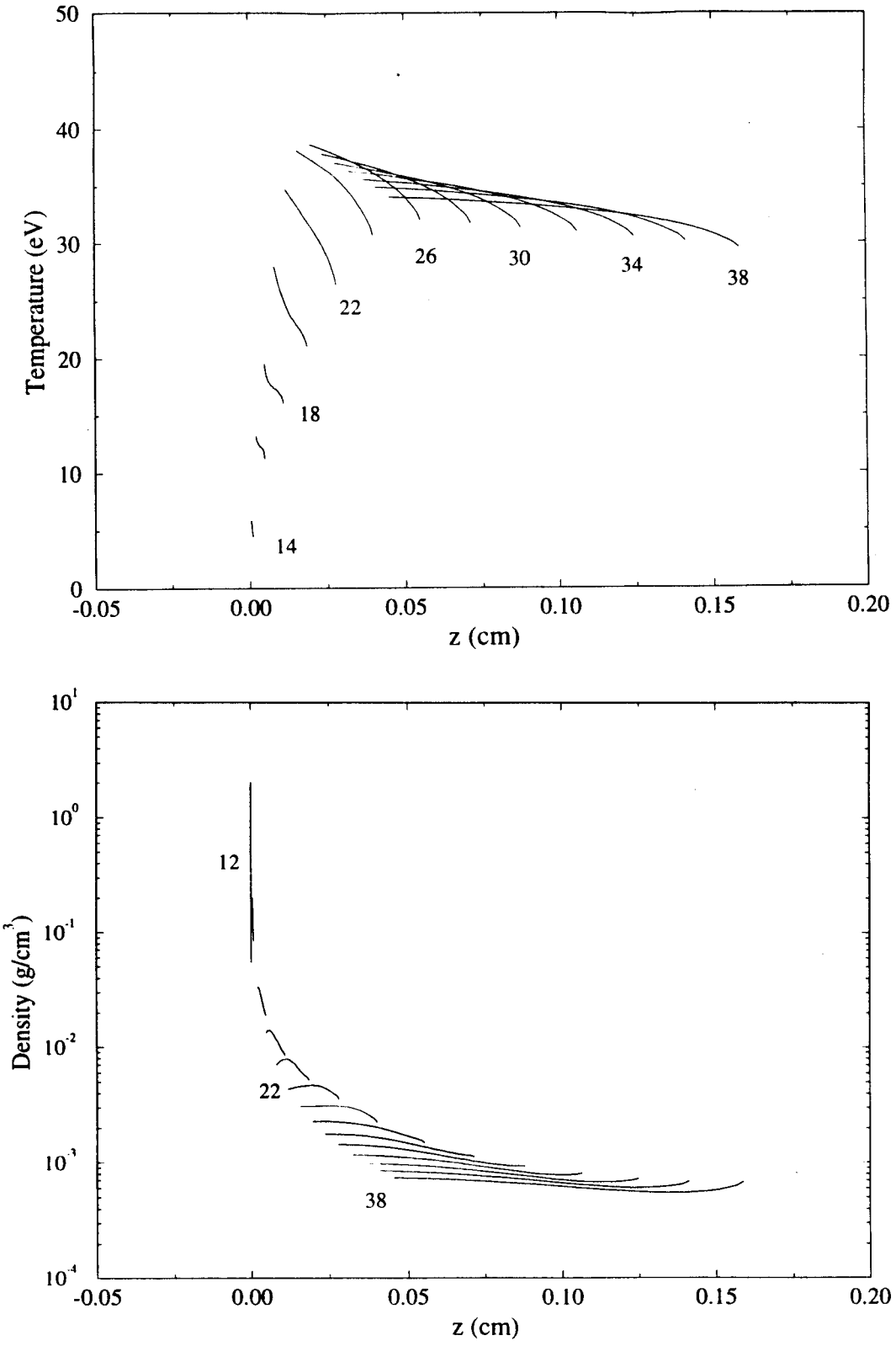

Figure 4.4. Same as Fig. 4.3, but for a 3 TW/cm^2 Li beam.

beam properties as those used in the radiation-hydrodynamic simulations. Atomic level populations and line intensities were computed using term-dependent Auger rates and fluorescence yields. Because the strongest lines tend to be optically thick, photoexcitation (resonance self-absorption) effects were computed using an escape probability radiative transfer model (MacFarlane et al. 1990, 1991).

Figure 4.5 shows time-dependent spectra from the CRE calculations for the 3 TW/cm^2 case. At 12 ns, several satellites are predicted to exhibit intensities of comparable magnitude to the cold Al K_α line (at $\lambda = 8.34$ Å). This results from the ejection of multiple inner shell electrons during a collision with the Li^{3+} beam. As discussed in Section II, multiple ionization processes tend to be of greater importance for the lower ionization stages of Al.

As the plasma temperature increases, satellites at shorter wavelengths appear. (Note the change in scale between simulation times.) Relatively little emission, however, is predicted at wavelengths shortward of 8.0 Å until a simulation time of 22 ns, at which point the plasma temperature is approximately 30 eV. The dominant ionization stages at this time are C-like and N-like Al. The Be-like autoionizing levels are primarily populated either by B-like Al via the ionization of a single K-shell electron, or by C-like Al via the simultaneous ejection of one K-shell and one L-shell electron. Our calculation for the plasma conditions at $t = 22$ ns indicates that the Be-like autoionizing states in the $1s^1\,2s^1\,2p^2$ configuration are roughly 3 times more likely to originate from B-like Al as opposed to C-like Al. Thus, even though C-like Al is predicted to be roughly 5 times more abundant than B-like Al, single ionization processes can still be an important populating mechanism for some of the levels of these relatively high ionization stages.

The peak temperature occurs at 26 ns in the radiation-hydrodynamic simulation. The CRE calculations indicate the intensities of He-like ($\lambda = 7.76$ Å) through B-like ($\lambda \simeq 8.02$ Å) Al are the greatest at this time. The excited states of the He-like ion are populated at about the same rate by the beam impact ionization of Be-like and B-like Al. Even though the single ionization cross sections for these stages are higher than those for multiple ionization (see Section II), the rate for ionization from Li-like Al (a single ionization process) is lower because its ionization fraction is low ($\sim 10^{-4}$). C-like and B-like Al are the most abundant ionization stages at this time.

Figure 4.6 compares the computed time-integrated spectrum for the 3 TW/cm^2 case with the observed spectrum from Shots 5881 and 5851. The calculated spectrum

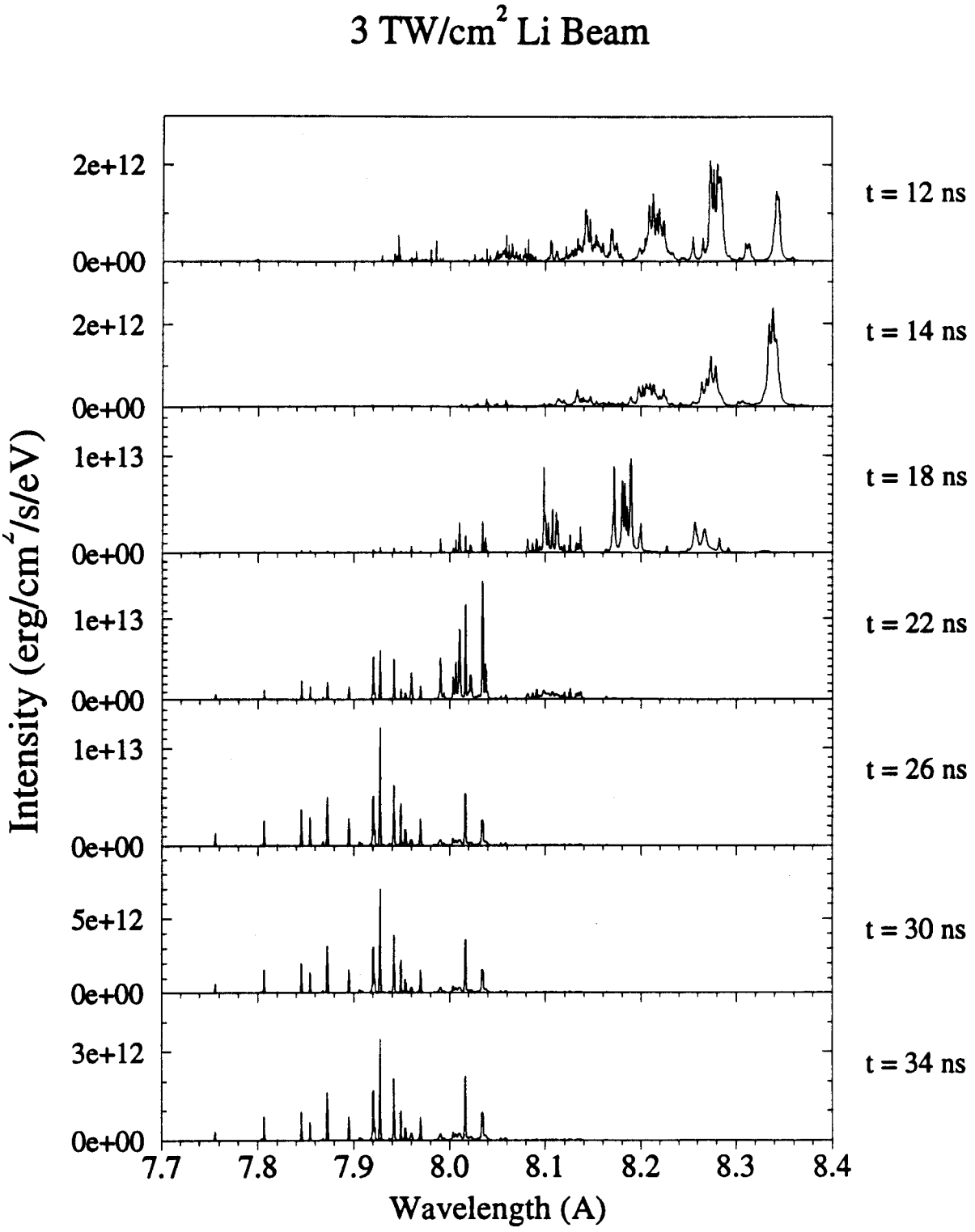

Figure 4.5. Calculated Al K_α spectra using temperature and density distributions from a radiation-hydrodynamics calculation with a 3 TW/cm^2 Li beam.

was obtained by summing the results from 12 to 38 ns and smoothing the spectrum with a 1 eV (5.5 mÅ) FWHM Gaussian to account for instrumental broadening. The computed spectrum is seen to be quite similar to the observed spectrum in several respects. Firstly, the predicted wavelengths of the peak intensities for each of the satellites is reasonably consistent with the data, with the discrepancies being $\lesssim 0.01 - 0.02$ Å. (In these preliminary calculations, the calculated wavelengths may be slightly blue-shifted because the effect of correlation interactions may have been underestimated.) Secondly, the computed structure within each satellite compares well with the observed spectrum. And thirdly, the relative intensity of each of the satellites is in good general agreement. The calculated Be-like intensity between 7.9 and 8.0 Å is somewhat higher than observation when compared with the lower ionization satellites, but the overall agreement is quite good for this 3 TW/cm^2 case.

By comparison, the time-integrated spectrum computed using the radiation-hydrodynamic results from the 1 TW/cm^2 simulations is in rather poor agreement with the observed spectrum. This is seen in Fig. 4.7, where the 3 TW/cm^2 results (middle spectrum) are compared with the 1 TW/cm^2 results (top). For the 1 TW/cm^2 case, the peak intensities are predicted to come from C-like, N-like, and O-like Al. Note that very little emission is expected from the He-like through Be-like Al K_α lines, whose satellites are clearly detected in Shots 5881 and 5851.

The higher satellites do not appear in the 1 TW/cm^2 case because the peak temperature in the radiation-hydrodynamic simulations is predicted to be only about 26 eV. The CRE calculations predict the dominant ionization stage to reach only as high as N-like Al. Thus, the combined CRE/hydrodynamics analysis results in much better agreement with the observed spectrum when the beam power density is 3 TW/cm^2.

A third series of CRE calculations was run to determine the sensitivity of the K_α spectrum to plasmas with higher temperatures. In this series, we assumed the same beam parameters and plasma density distributions as in the 3 TW/cm^2 case, but the plasma temperatures were assumed to be 20% higher. The peak temperature in the series was 47 eV. The resulting time-integrated spectrum is shown at the bottom of Fig. 4.7. The highest intensities in this case are from Li-like and Be-like lines, which is not consistent with the observation. It is, however, interesting to note that the relative strengths of the 2 Li-like lines near 7.85 Å shifts toward the longer wavelength line ($\lambda = 7.855$ Å results from $1s^1\,2p^2\,{}^2P \rightarrow 1s^2\,2p^1\,{}^2P$, while $\lambda = 7.846$ Å results from $1s^1\,2s^1\,2p^1\,{}^2P \rightarrow 1s^2\,2s^1\,{}^2S$), as the temperature increases (see Section V for more details

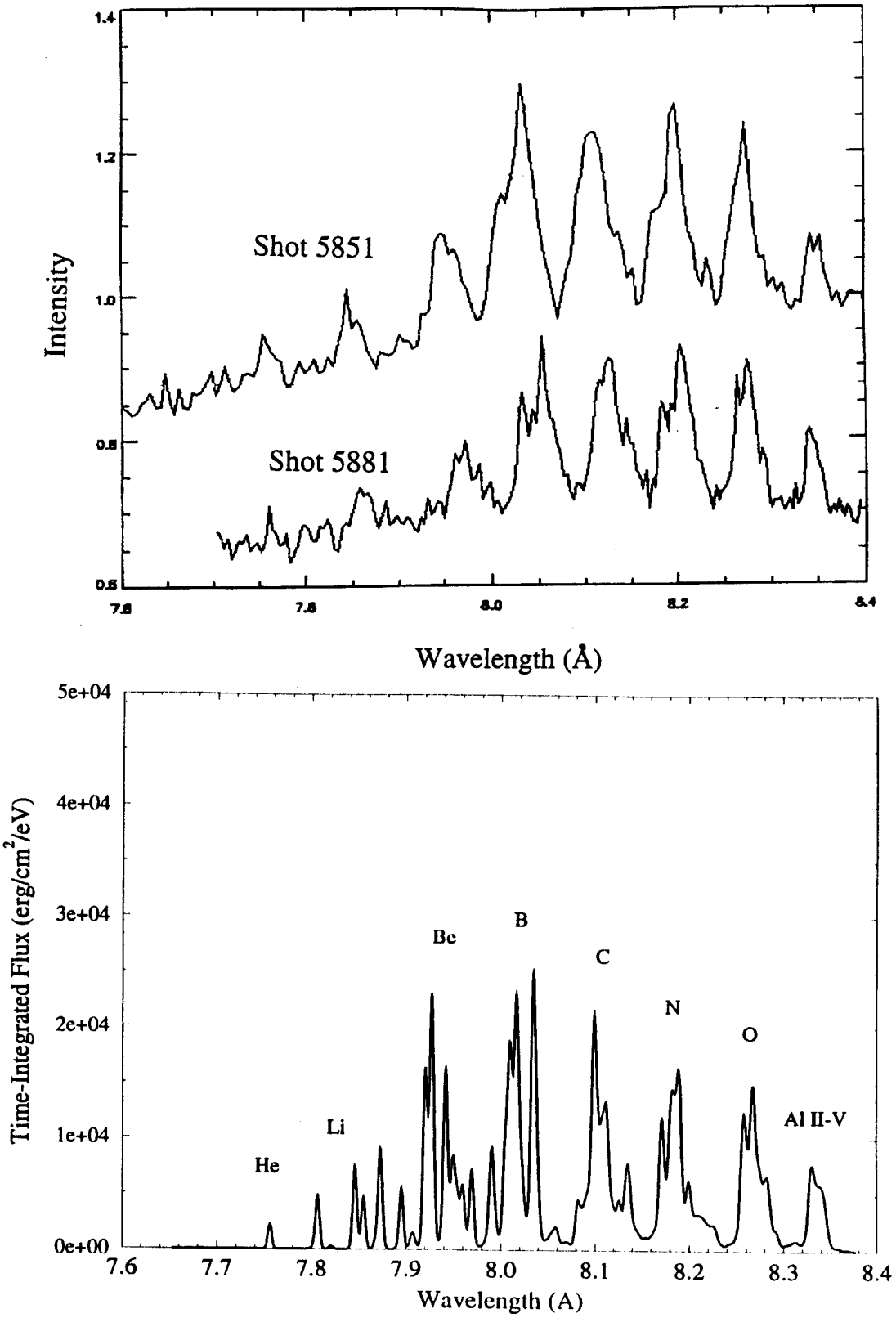

Figure 4.6. Comparison of observed K_α spectrum from Shots 5881 and 5851 (top) with the calculated time-integrated spectrum for the case with a 3 TW/cm^2 Li beam (bottom).

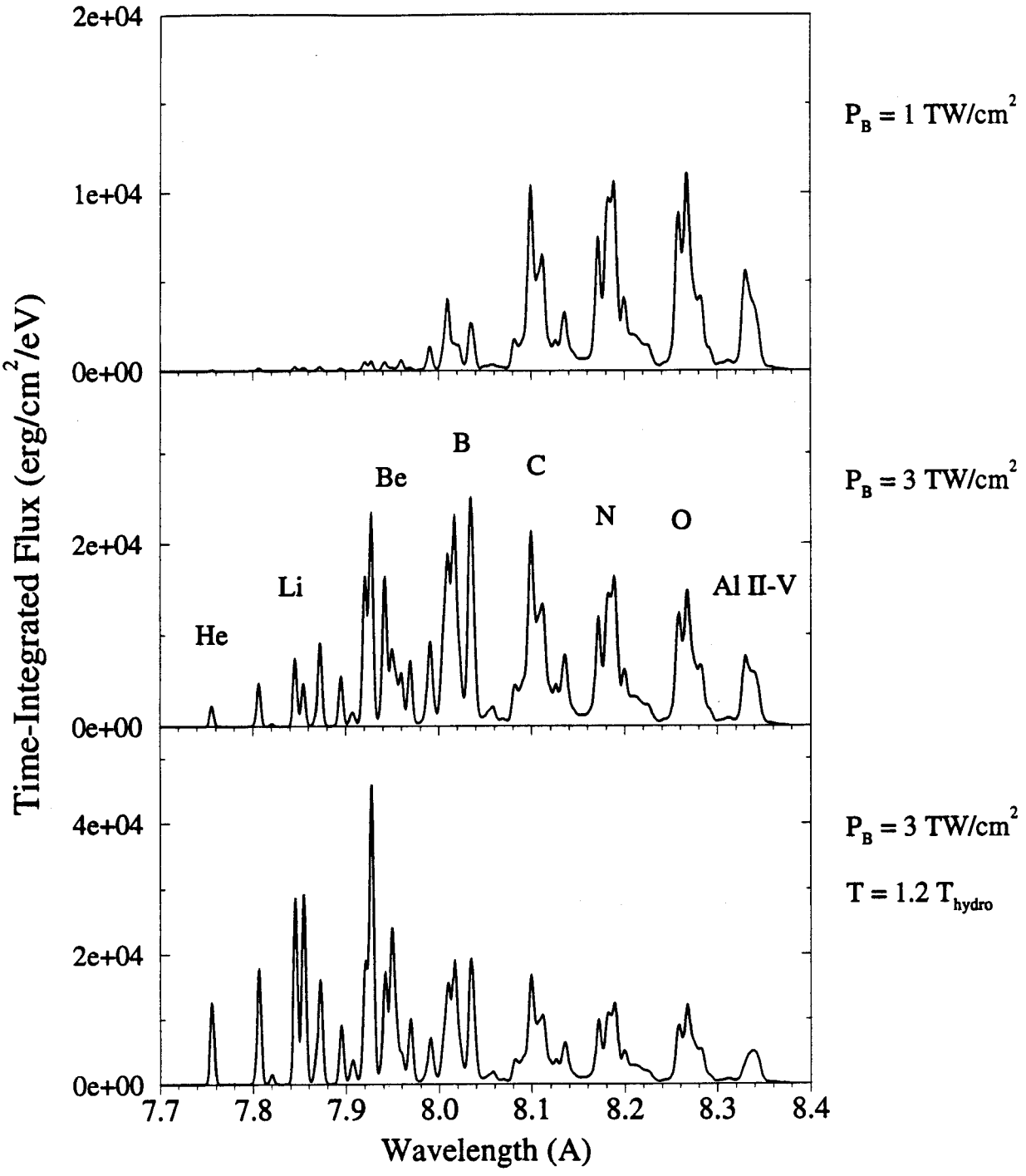

Figure 4.7. Calculated time-integrated Al K_α spectrum for: (top) 1 TW/cm^2 case; (middle) 3 TW/cm^2 case; (bottom) same as middle, but with plasma temperatures increased by 20%.

on using line ratios as diagnostics). By comparison, the ratio (λ 7.855/λ 7.846) observed in Shot 5881 is somewhat lower than that seen in the bottom spectrum of Fig. 4.7, but somewhat higher than seen in the middle spectrum. This suggests the peak temperature in the experiment was somewhere between those of these 2 cases; i.e., between 39 and 47 eV.

Figure 4.8 show the energy levels involved in producing the strongest K_α lines in our calculations. The spectral fluxes are from calculations for different simulation times of the hydrodynamics calculation for the 3 TW/cm^2 case. Except when the plasma is at relatively low temperatures ($t < 16$ ns) the strongest lines are those without M-shell spectator electrons.

Figure 4.9 shows the frequency-dependent optical depth corresponding to the simulation time of 26 ns; i.e., the time at which the maximum temperature occurs. Note that all lines shortward of 7.9 Å have line center optical depths of $\lesssim 10^{-1}$. In fact the He-like line at 7.76 Å has an optical depth of only 0.02. Thus, if the diagnostic region was, say, 5 times thicker, the intensities of the He-like and Li-like lines would have been approximately 5 times more intense. The trade-off of course is that the Be-like and B-like lines would become even more optically thick, a complexity one would like to avoid when interpreting spectra. However, if one is interested in using the highest observed ionization stages as a diagnostic, a thicker diagnostic layer could be used (say, up to 1 μm) and still avoid major problems associated with resonance self absorption.

To conclude, the combined CRE/radiation-hydrodynamics analysis is consistent with a beam power density of about 3 TW/cm^2. The 1 TW/cm^2 case clearly does not produce high enough ionization to be consistent with the K_α spectrum of Shots 5881 and 5851. In fact, this preliminary analysis suggests the maximum temperature obtained in the experiment may have been slightly higher (perhaps 10%) than the 39 eV predicted from the 3 TW/cm^2 radiation-hydrodynamics calculation.

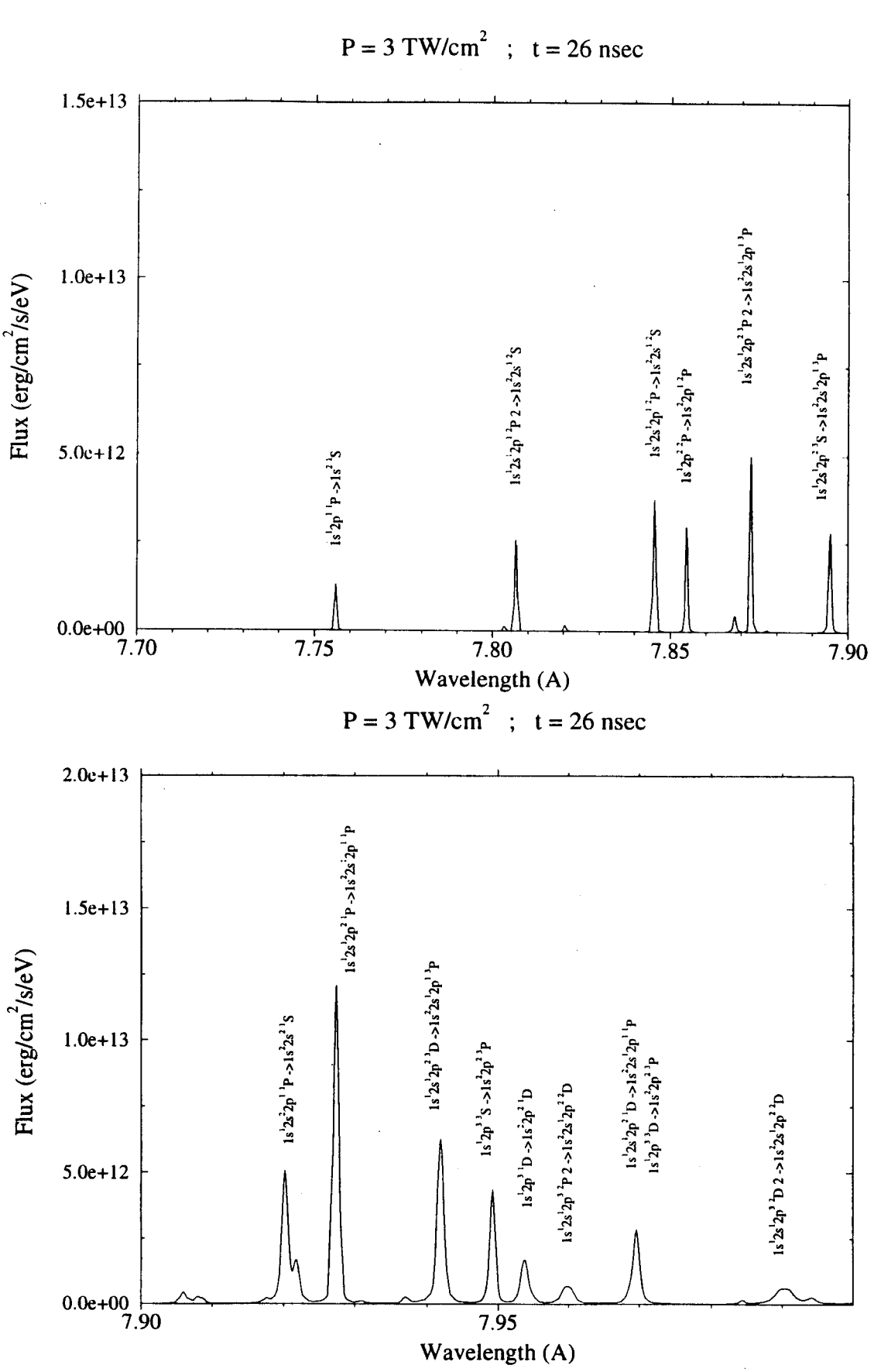

Figure 4.8(a). Identification of strongest lines occurring in the 3 TW/cm^2 calculation series.

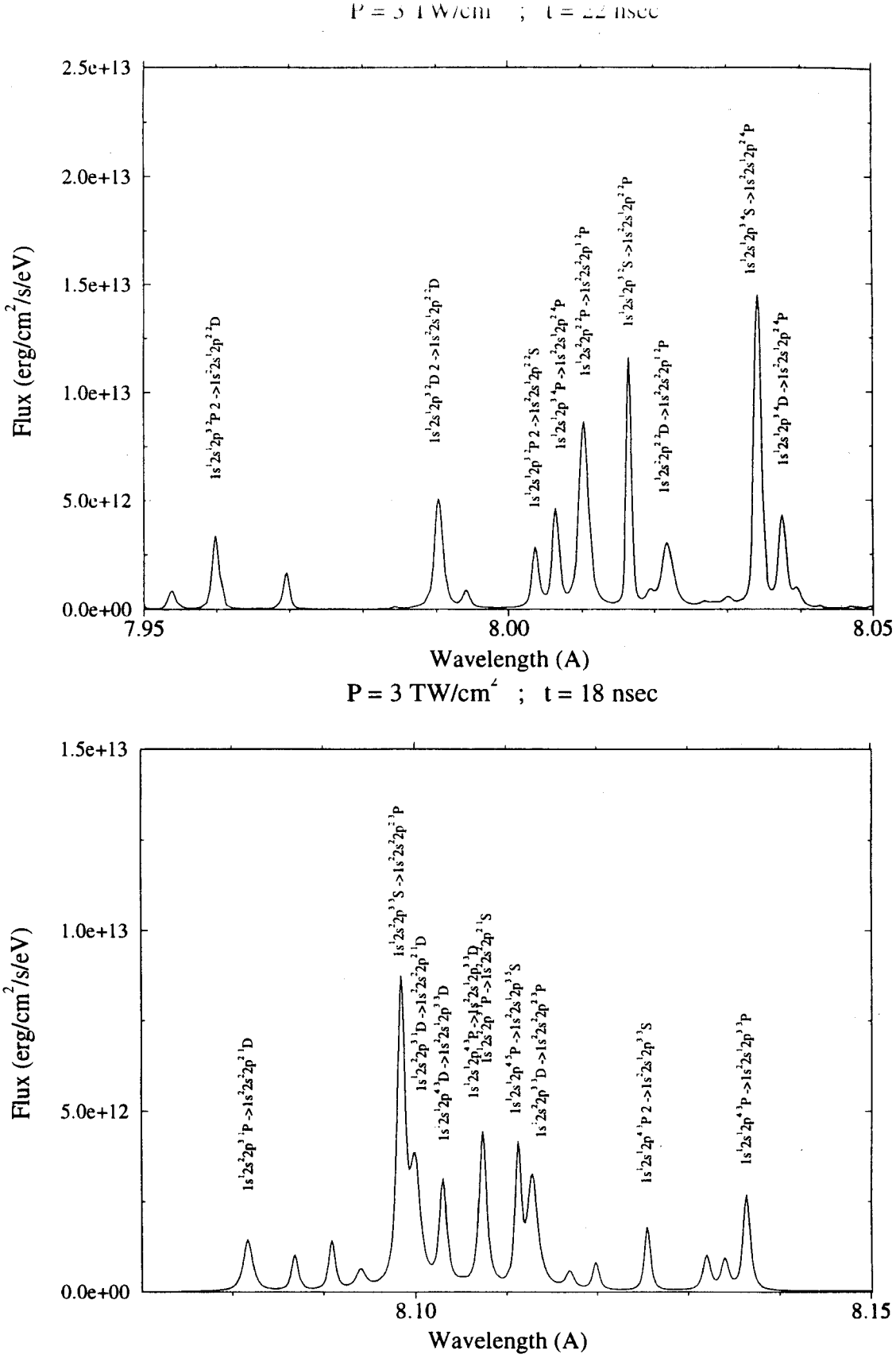

Figure 4.8(b). Identification of strongest lines occurring in the 3 TW/cm^2 calculation series.

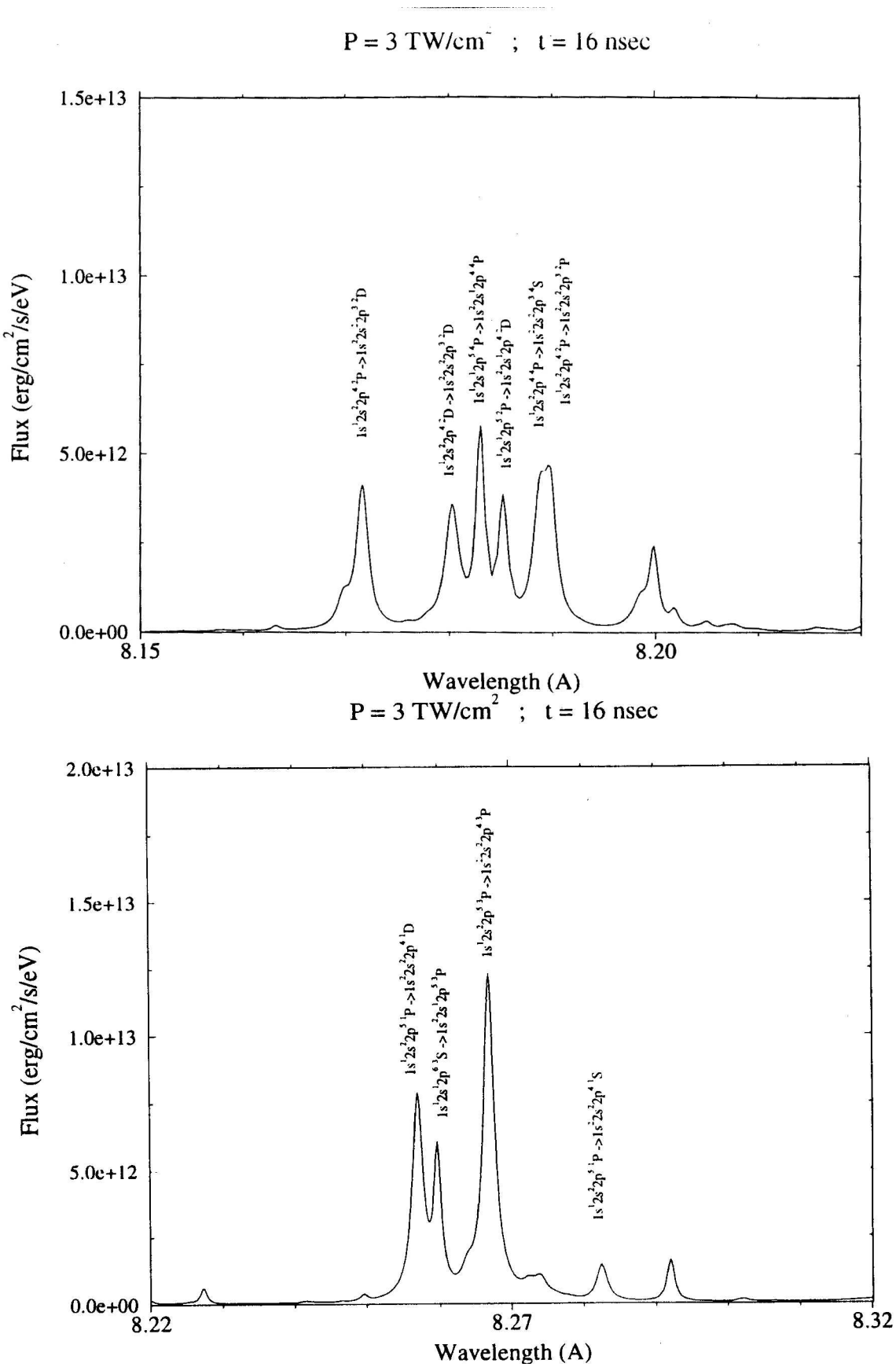

Figure 4.8(c). Identification of strongest lines occurring in the 3 TW/cm^2 calculation series.

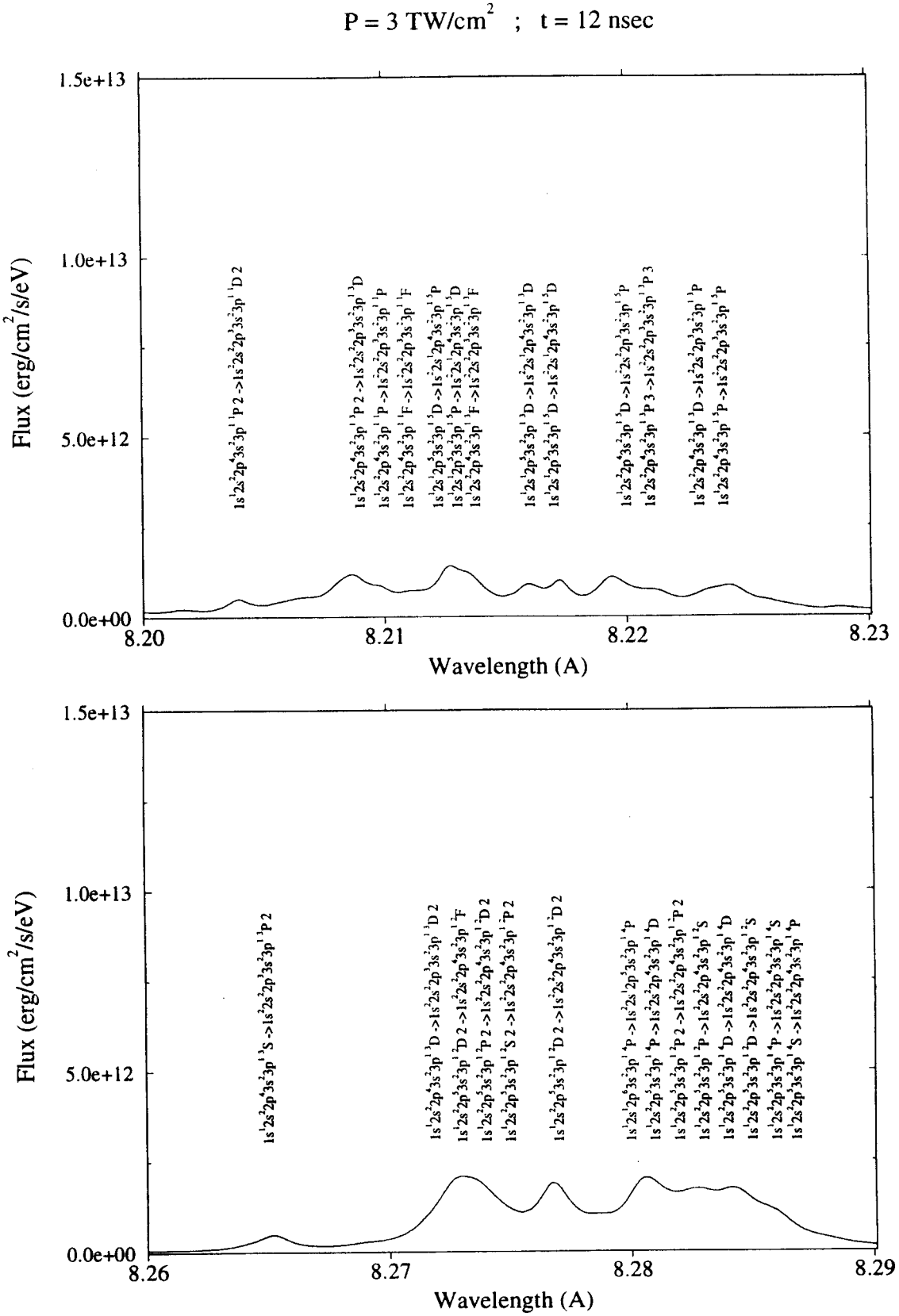

Figure 4.8(d). Identification of strongest lines occurring in the 3 TW/cm^2 calculation series.

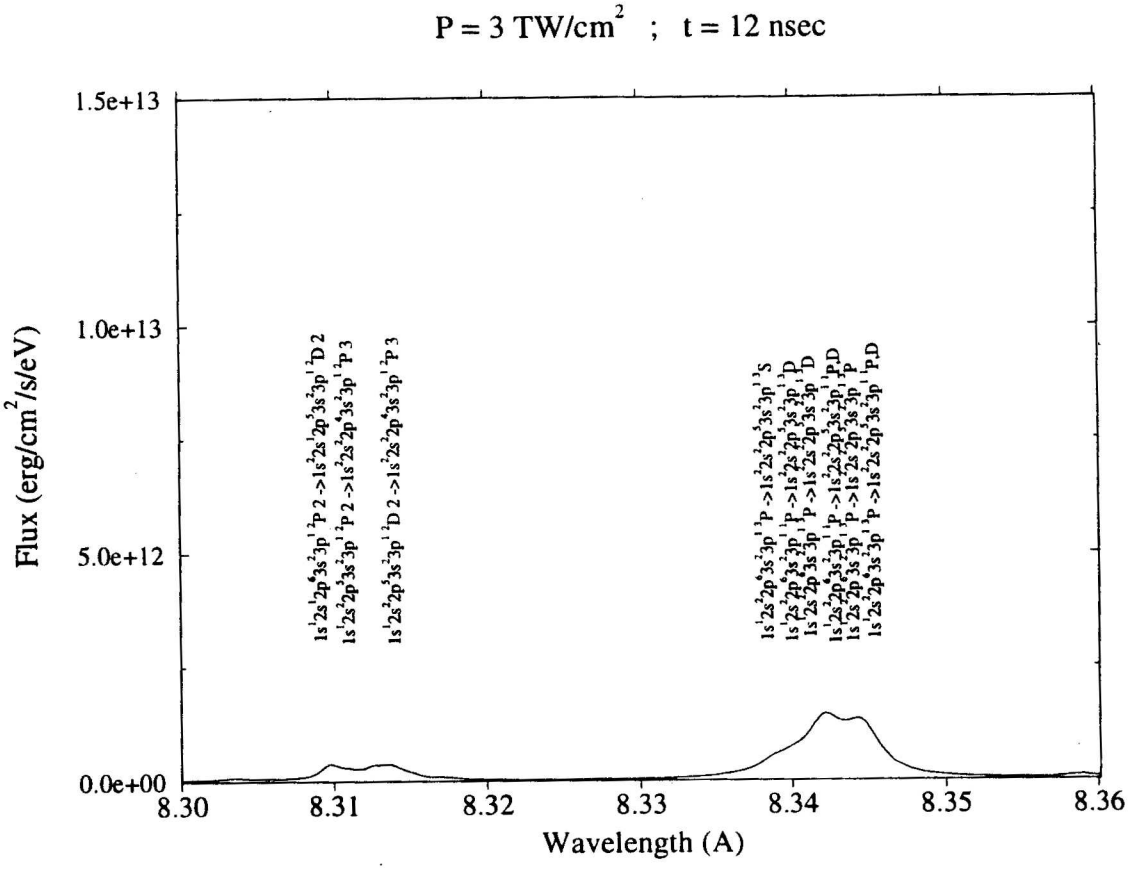

Figure 4.8(e). Identification of strongest lines occurring in the 3 TW/cm^2 calculation series.

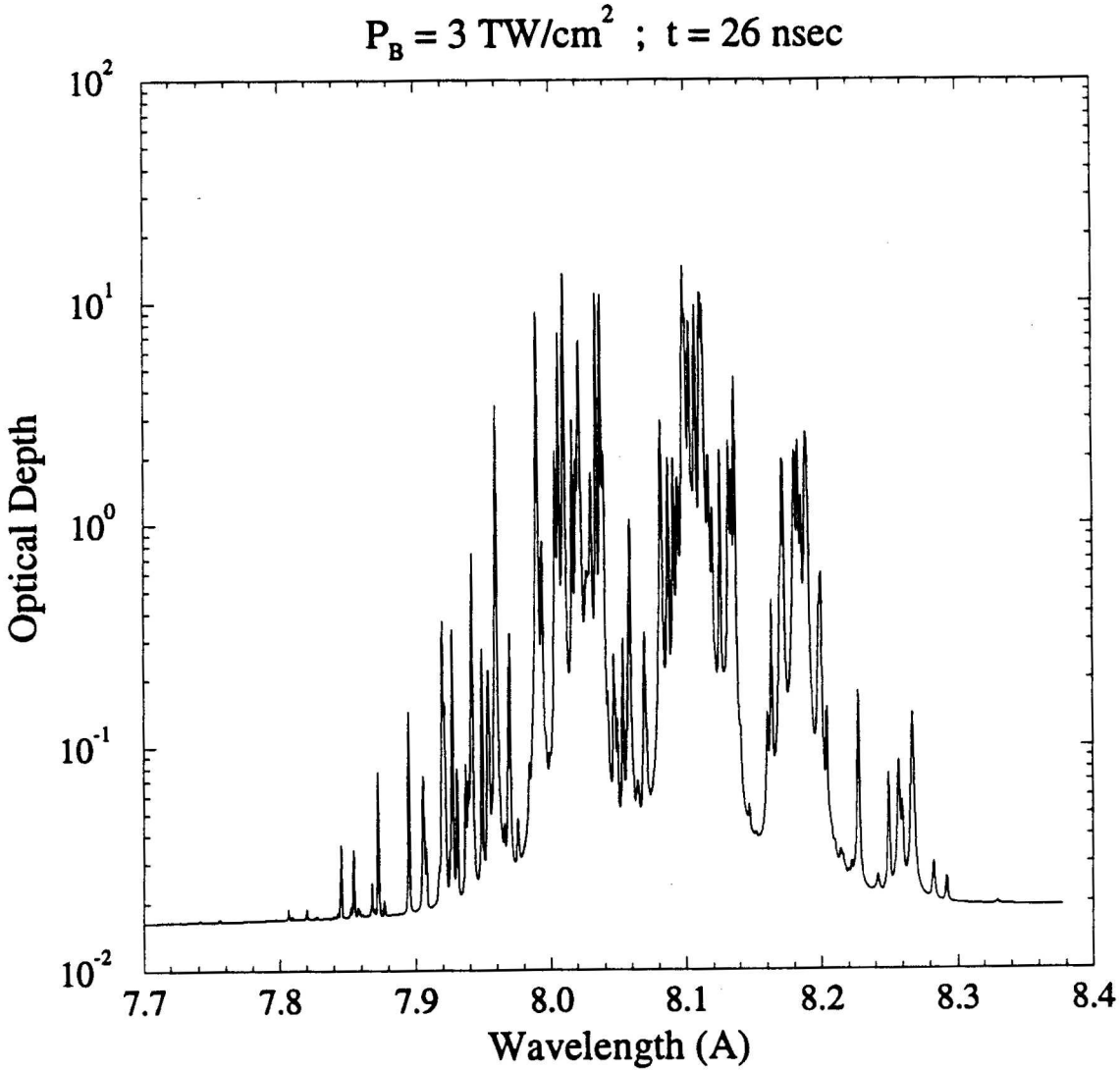

Figure 4.9. Frequency-dependent optical depth in the K_α satellite spectral region. The plasma conditions are those predicted by the 3 TW/cm^2 radiation-hydrodynamics simulations at the time of maximum temperature ($t = 26$ ns).

Section V

Diagnosing Conditions in Lithium Beam-Heated Plasmas from Al and Mg K_α Line Ratios

In this section, we examine the potential of using line ratios from Al and Mg K_α lines as a means of diagnosing plasma conditions in targets irradiated by intense Li beams. We have looked in particular at using the Li-like and He-like lines of Al because: (1) they have recently been observed in PBFA-II target experiments, and (2) the atomic physics modeling is simpler for these relatively few electron systems. In the calculations performed to date, we assumed the Al (or Mg) diagnostic layers to be optically thin and of uniform temperature and density. The temperatures ranged from 30 to 70 eV, while the ion densities were varied between 10^{18} and 10^{22} cm^3.

Before describing the line ratio results, let us first compare line intensities between Al and Mg. Figure 5.1 shows calculated spectra for thin Al and Mg targets at $T = 40$ eV and $n = 10^{20}$ cm^3. The foil thicknesses and beam properties were identical for each calculation (a 9 MeV Li^{3+} beam was assumed). For Al the Be-like and Li-like K_α lines are strongest, while the Li-like and He-like lines are strongest for Mg. Table 5.1 shows the calculated wavelengths and upper and lower energy levels for the He-like and Li-like lines. Note that the strongest lines for Mg have peak intensities which are about a factor of 4 to 5 higher than for Al at the same plasma conditions. This results from: (1) the fluorescence yields for the He-like and Li-like ions are greater (for He-like, $Y = 1$); and (2) the He-like and Li-like ions are simpler and the photons resulting from beam-induced transitions are "funneled" through fewer K_α lines, thus making individual lines more intense. In fact, the He-like line ($1s^1\,2p^1\,{}^1P \rightarrow 1s^2\,{}^1S$) can be considerably stronger than those of lower ionization stages. This is shown in Fig. 5.2 where calculated Mg spectra are shown as a function of temperature. Note the change in scales for each temperature. For these optically thin plasmas the peak intensity for the He-like feature at 60 eV is about a factor of 11 greater than the Be-like line intensities which dominate at 30 eV.

The above results may have implications for diagnosing target plasma conditions. If two moderate-Z tracer layers were used in target experiments, the additional spectral information could be used to more accurately deduce target plasma temperatures and densities (Bailey 1993). For example, the peak temperature determined from analysis of the Al K_α spectrum in the recent PBFA-II lithium beam experiments was about 40 eV (see Section IV). If the Al layer was mixed with a similar amount of Mg, Fig. 5.1 shows

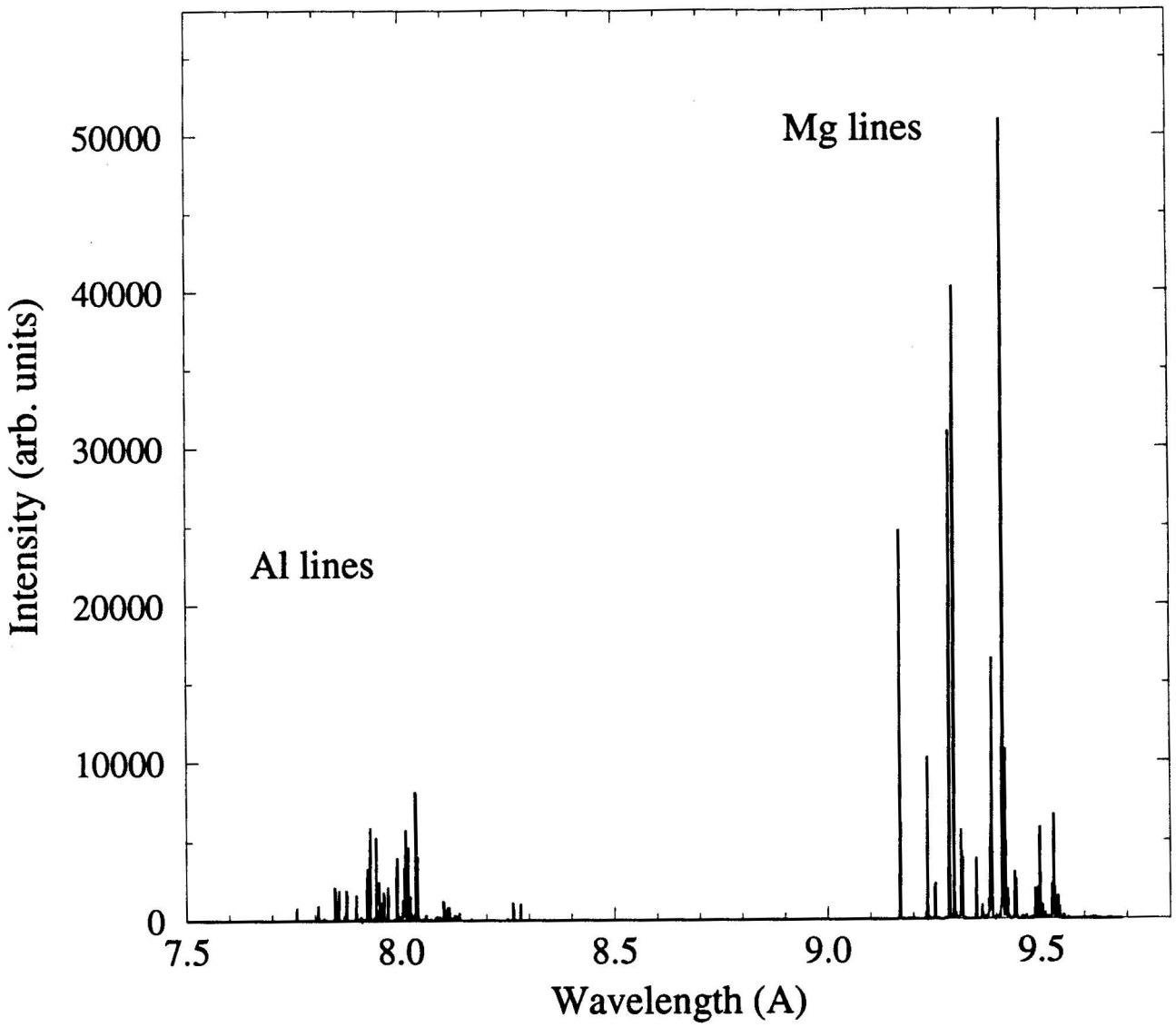

Figure 5.1. Calculated K_α spectra for optically thin Al and Mg diagnostic layers at $T = 40$ eV and $n = 10^{20}$ cm^{-3}.

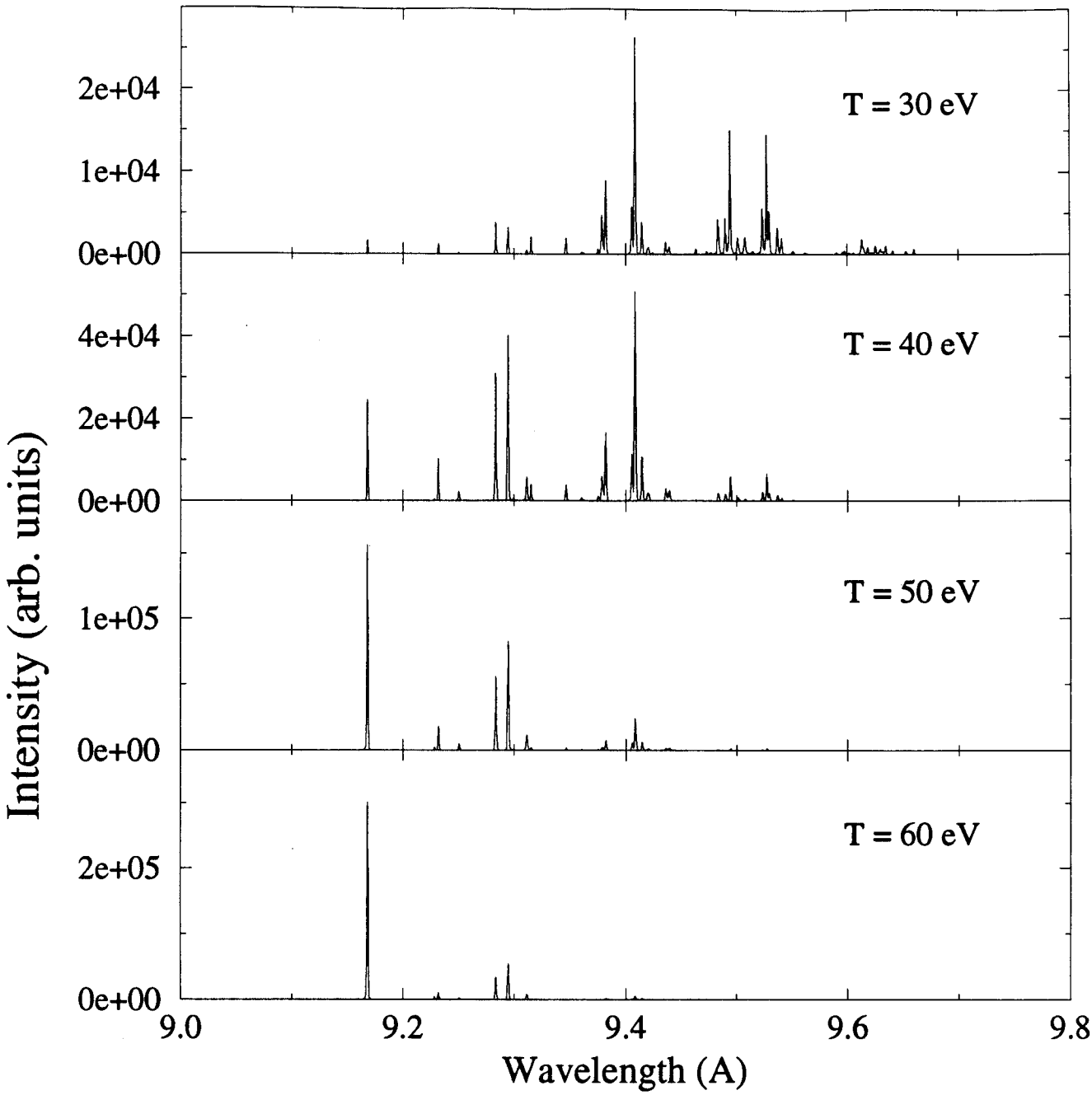

Figure 5.2. Dependence of Mg K_α spectrum on temperature for thin Mg layers at $n = 10^{20}$ cm^3. Note the strength of the He-like features increase significantly with temperature.

Table 5.1. Prominent He-like and Li-like K_α Lines for Al and Mg

Al Lines

Line Number	Ion	Upper Level		Lower Level		λ (calc.) (A)
1	He-like Al	$1s\,2p$	^1P	$1s^2$	^1S	7.756
2	He-like Al	$1s\,2p$	^3P	$1s^2$	^1S	7.803
3	Li-like Al	$1s\,2s\,2p$	$^2P(2)$	$1s^2\,2s$	^2S	7.807
4	Li-like Al	$1s\,2p^2$	^2S	$1s^2\,2p$	^2P	7.820
5	Li-like Al	$1s\,2s\,2p$	^2P	$1s^2\,2s$	^2S	7.846
6	Li-like Al	$1s\,2p^2$	^2P	$1s^2\,2p$	^2P	7.855
7	Li-like Al	$1s\,2p^2$	^2D	$1s^2\,2p$	^2P	7.868
8	Be-like Al	$1s\,2s\,2p^2$	$^3P(2)$	$1s^2\,2s\,2p$	^3P	7.873
9	Be-like Al	$1s\,2s\,2p^2$	^3S	$1s^2\,2s\,2p$	^3P	7.895

Mg Lines

Line Number	Ion	Upper Level		Lower Level		λ (calc.) (A)
1	He-like Mg	$1s\,2p$	^1P	$1s^2$	^1S	9.168
2	He-like Mg	$1s\,2p$	^3P	$1s^2$	^1S	9.228
3	Li-like Mg	$1s\,2s\,2p$	$^2P(2)$	$1s^2\,2s$	^2S	9.232
4	Li-like Mg	$1s\,2p^2$	^2S	$1s^2\,2p$	^2P	9.250
5	Li-like Mg	$1s\,2s\,2p$	^2P	$1s^2\,2s$	^2S	9.283
6	Li-like Mg	$1s\,2p^2$	^2P	$1s^2\,2p$	^2P	9.295
7	Li-like Mg	$1s\,2p^2$	^2D	$1s^2\,2p$	^2P	9.311
8	Be-like Mg	$1s\,2s\,2p^2$	$^3P(2)$	$1s^2\,2s\,2p$	^3P	9.315
9	Be-like Mg	$1s\,2s\,2p^2$	^3S	$1s^2\,2s\,2p$	^3P	9.346

that the Mg lines would have been a factor of a few more intense than the Al lines (because it reached a higher ionization stage). Furthermore, the He-like line intensity increases rapidly with temperature. So if the peak temperature reached, say, 50 eV instead of 40 eV, the He-like line intensity would have been even higher (by about a factor of 6). Higher intensities are of course preferable because more and stronger lines can lead to a more accurate determination of plasma conditions.

It is interesting to consider what would happen if the Al layer in the experiments described in Section IV were replaced by a Mg layer of the same thickness. Using the radiation-hydrodynamics results for the 3 TW/cm^2 Li beam case (see Fig. 4.4) we have computed a time-integrated Mg K_α satellite spectrum. The results are shown in Fig. 5.3 (bottom) and compared with the Al results (top). Also shown as dashed curves in Fig. 5.3 are the spectra computed using plasma temperatures which were 20% higher than those predicted by the 3 TW/cm^2 radiation-hydrodynamics calculations. Note the difference in the magnitude of the intensities for the Al and Mg calculations. For the $T = T_{hydro}$ case, the He-like (λ = 9.17 Å) and Li-like (λ = 9.2-9.3 Å) Mg lines are typically a factor of about 4 greater than the strongest Al lines. It is also seen that the Mg He-like line is quite sensitive to the temperature, with its peak increasing by about an order of magnitude for the $T = 1.2\,T_{hydro}$ case. (Recall that these results include opacity effects.) Thus, a Mg tracer layer could also be used to either provide additional diagnostic constraints for the same region (if it were mixed with Al), or perhaps diagnostic information on a separate region of the target.

In principal, the target plasma density and temperature can be determined by examining individual line ratios from time-resolved spectral measurements. To study this possibility for Li beam experiments on PBFA-II, we have computed line ratios for several He-like and Li-like lines of Al and Mg. The results for Al are shown in Fig. 5.4, while those for Mg are shown in 5.5. The temperature and density-dependence for each line ratio is shown. The lines are identified by indices at the top of each plot, where the line indices are defined in Table 5.1. For example, "2-1" is the ratio of the He-like intercombination line ($1s^1\,2p^1\,{}^3P \rightarrow 1s^2\,{}^1S$) intensity to the He-like resonance line ($1s^1\,2p^1\,{}^1P \rightarrow 1s^2\,{}^1S$) intensity. (Some term symbols are labeled as "$^2P(2)$"; this is just our system of identifying levels which can have identical term symbols because of multiple open shells.) The particular choice of Be-like lines was made based on wavelength — i.e., potential "contamination" of Li-like lines — as opposed to line strength.

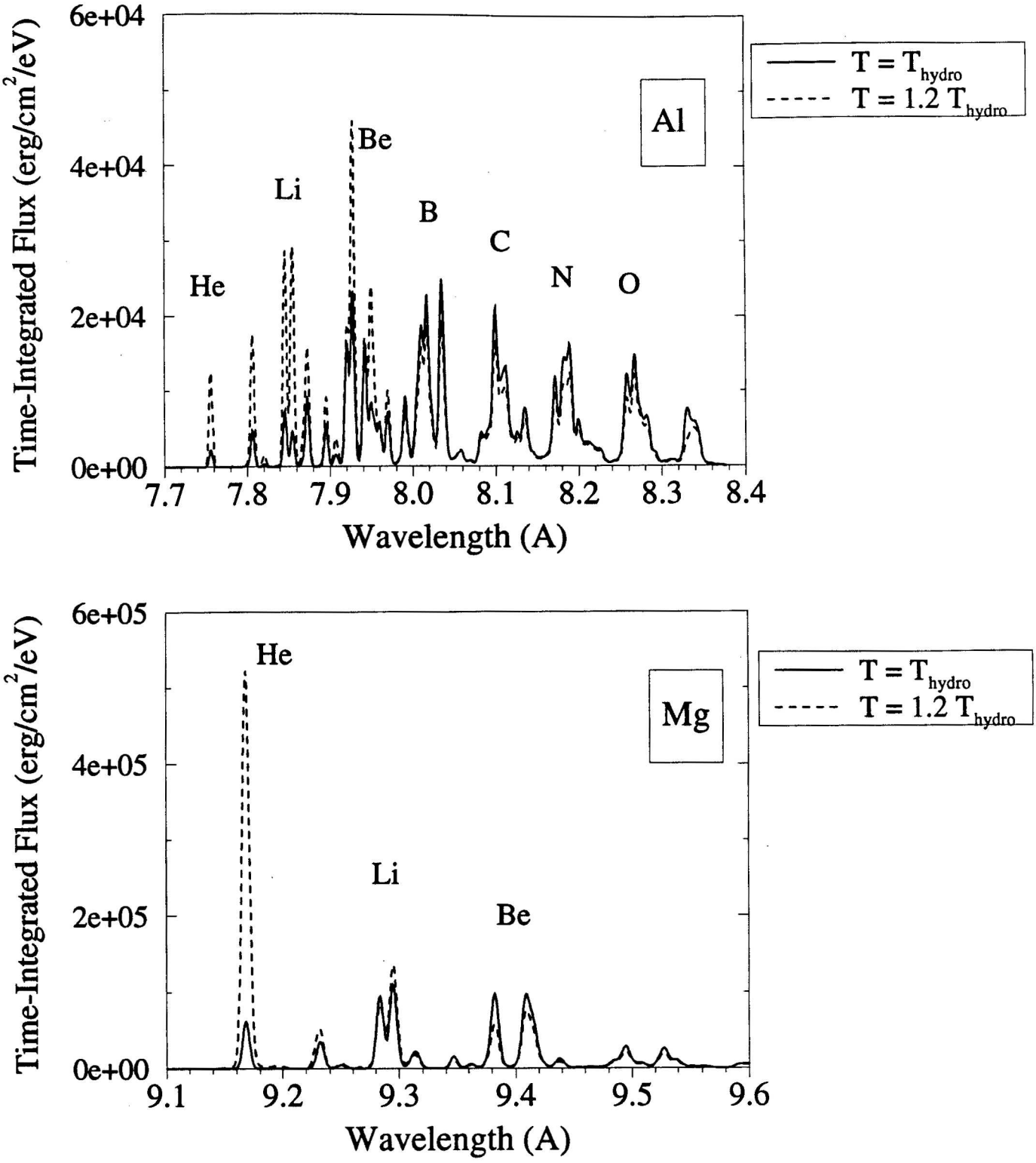

Figure 5.3. Calculated time-integrated K_α satellite spectra for Al (top) and Mg (bottom) using radiation-hydrodynamics results for 3 TW/cm^2 Li beam simulation. The dashed curves correspond to cases where the plasma temperatures were 20% higher than those predicted by the radiation-hydrodynamics calculations.

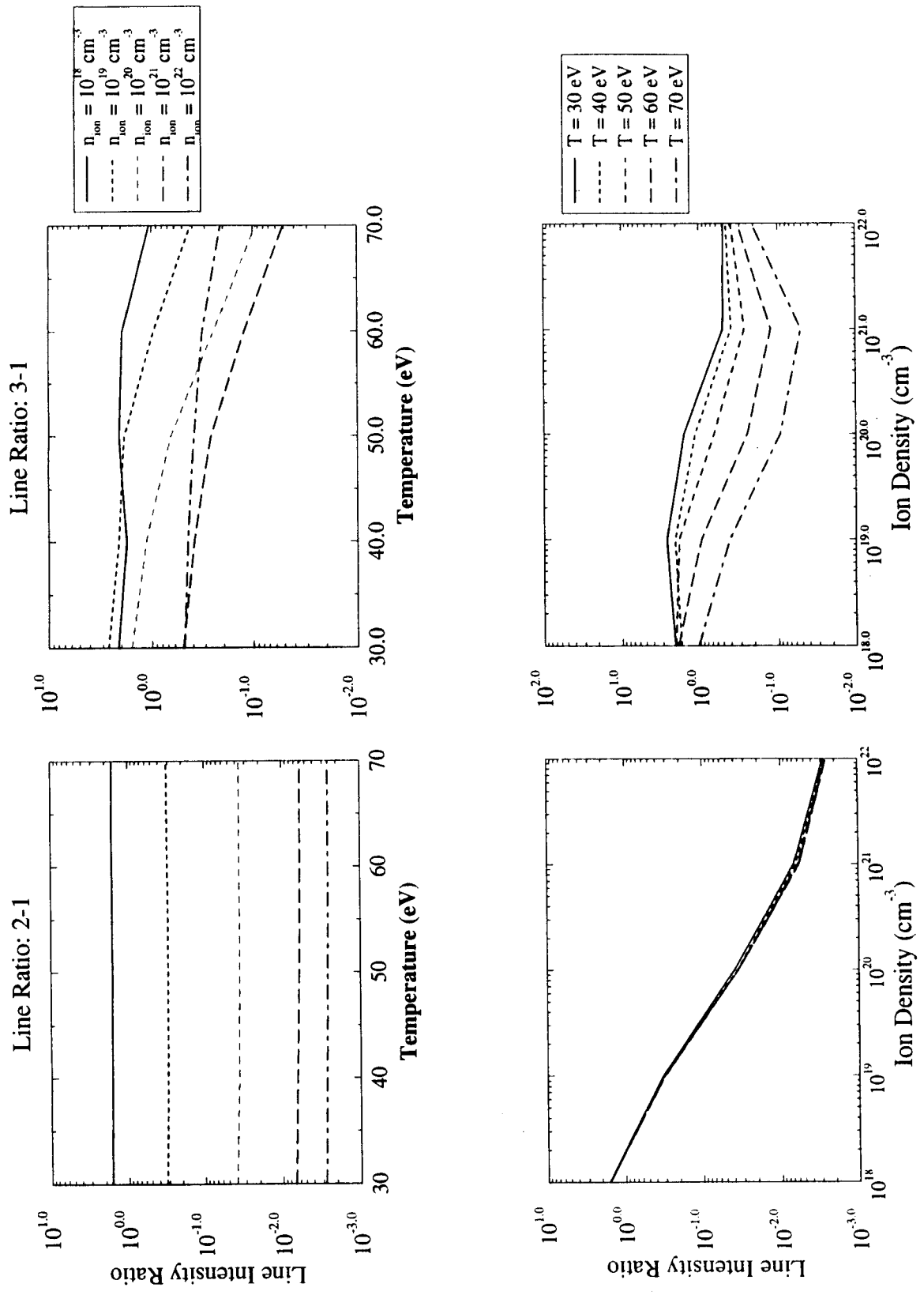

Figure 5.4(a). Calculated line intensity ratios for Al. Line definitions are given in Table 5.1.

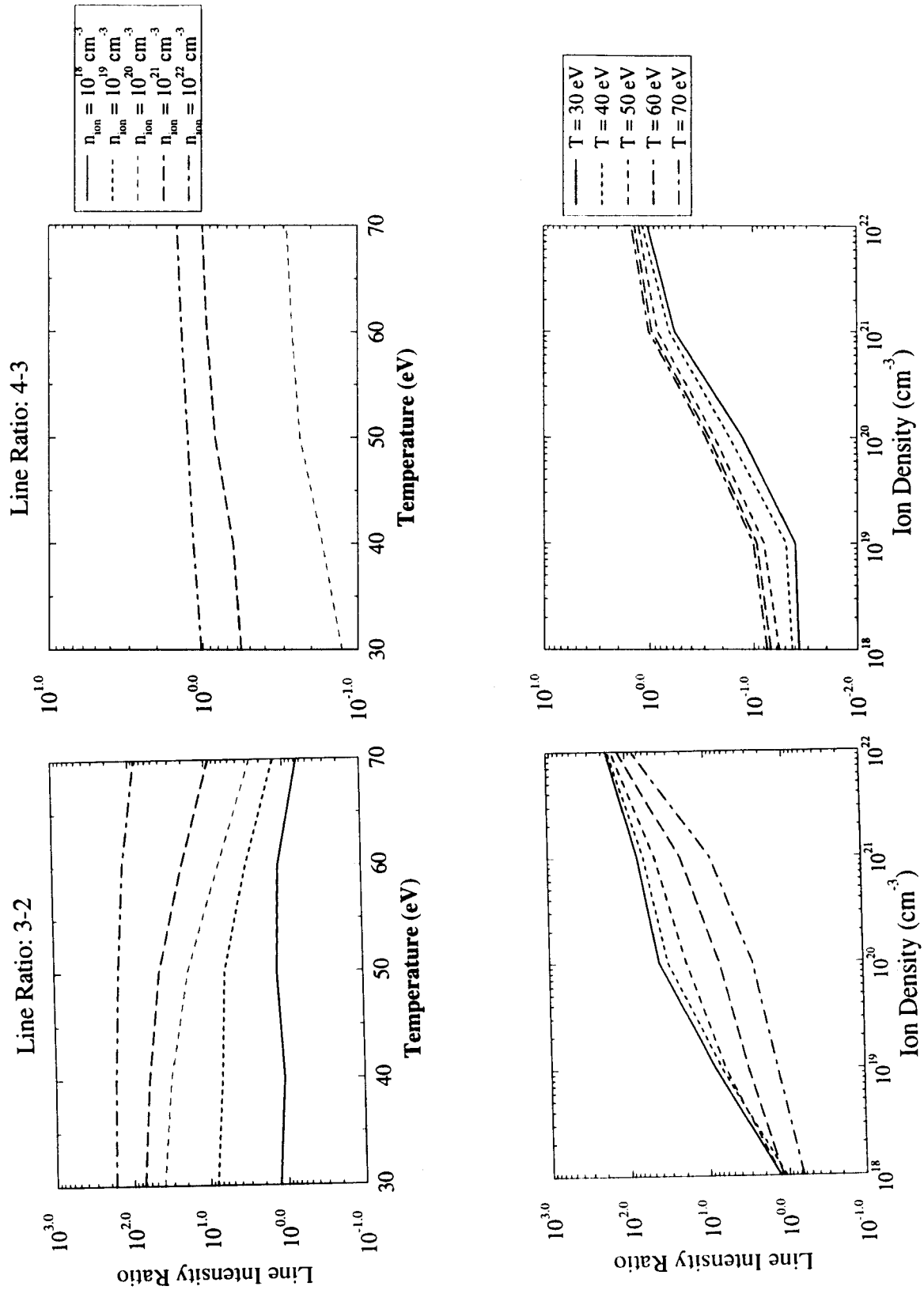

Figure 5.4(b). Calculated line intensity ratios for Al. Line definitions are given in Table 5.1.

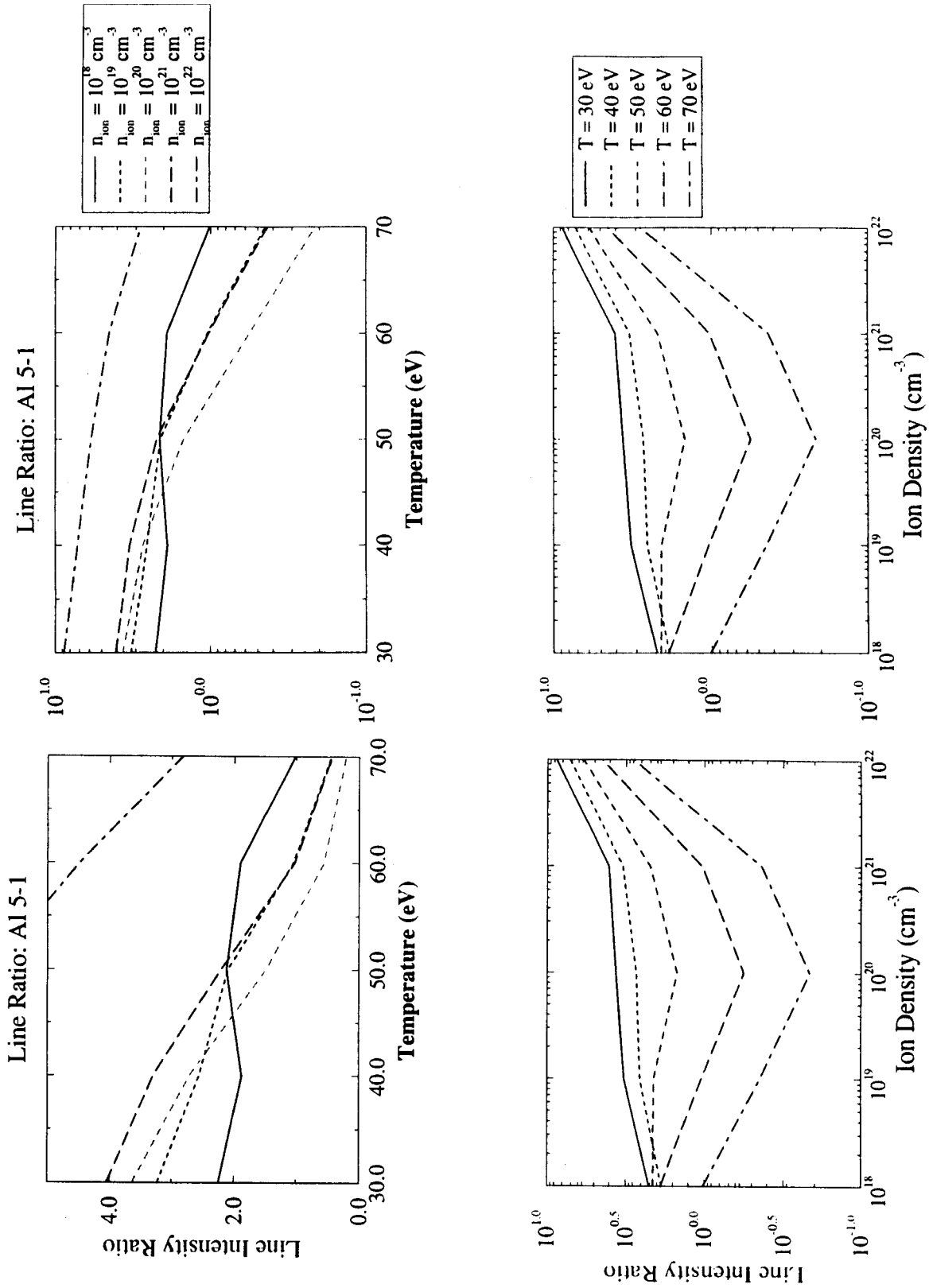

Figure 5.4(c). Calculated line intensity ratios for Al. Line definitions are given in Table 5.1.

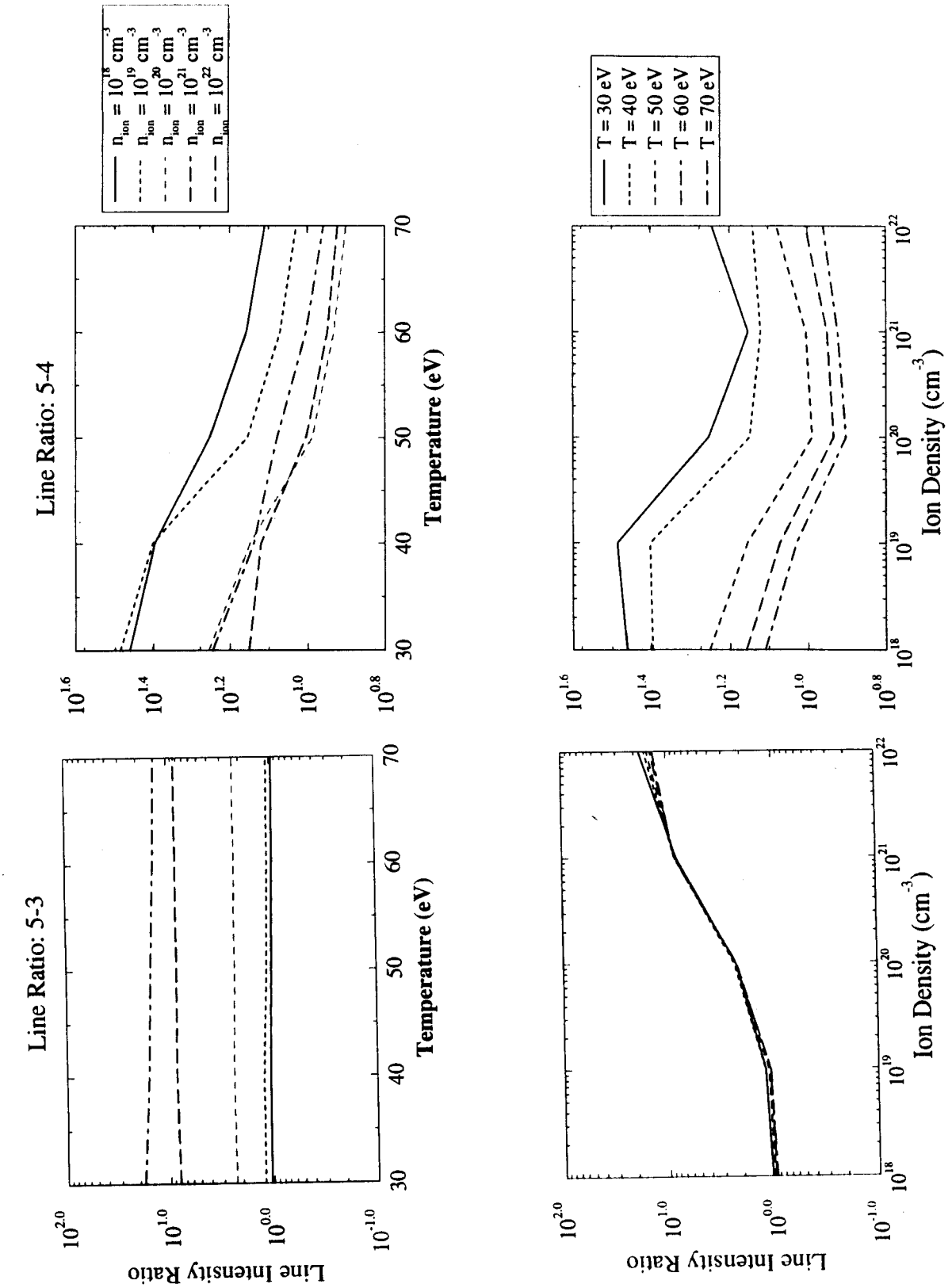

Figure 5.4(d). Calculated line intensity ratios for Al. Line definitions are given in Table 5.1.

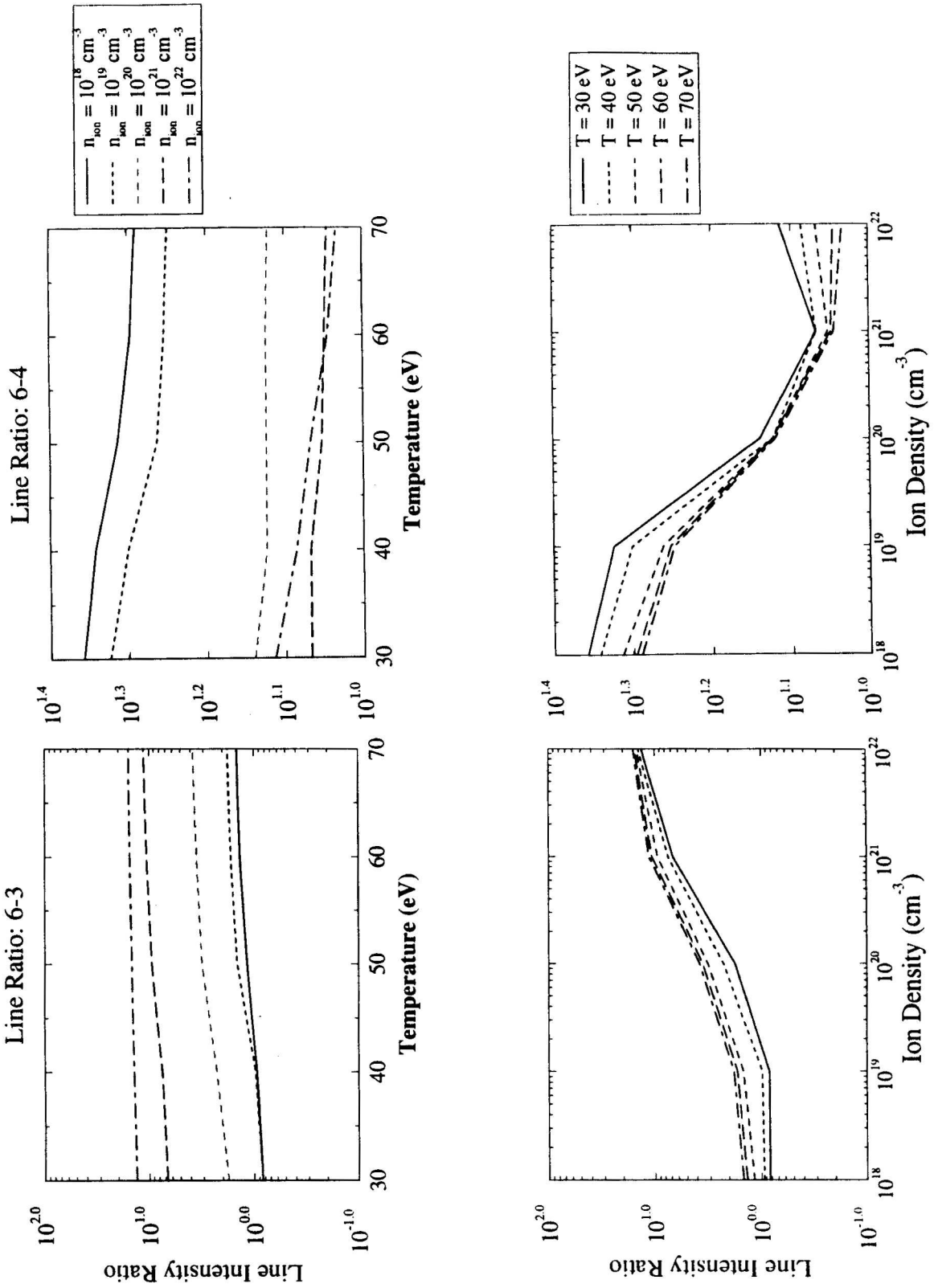

Figure 5.4(e). Calculated line intensity ratios for Al. Line definitions are given in Table 5.1.

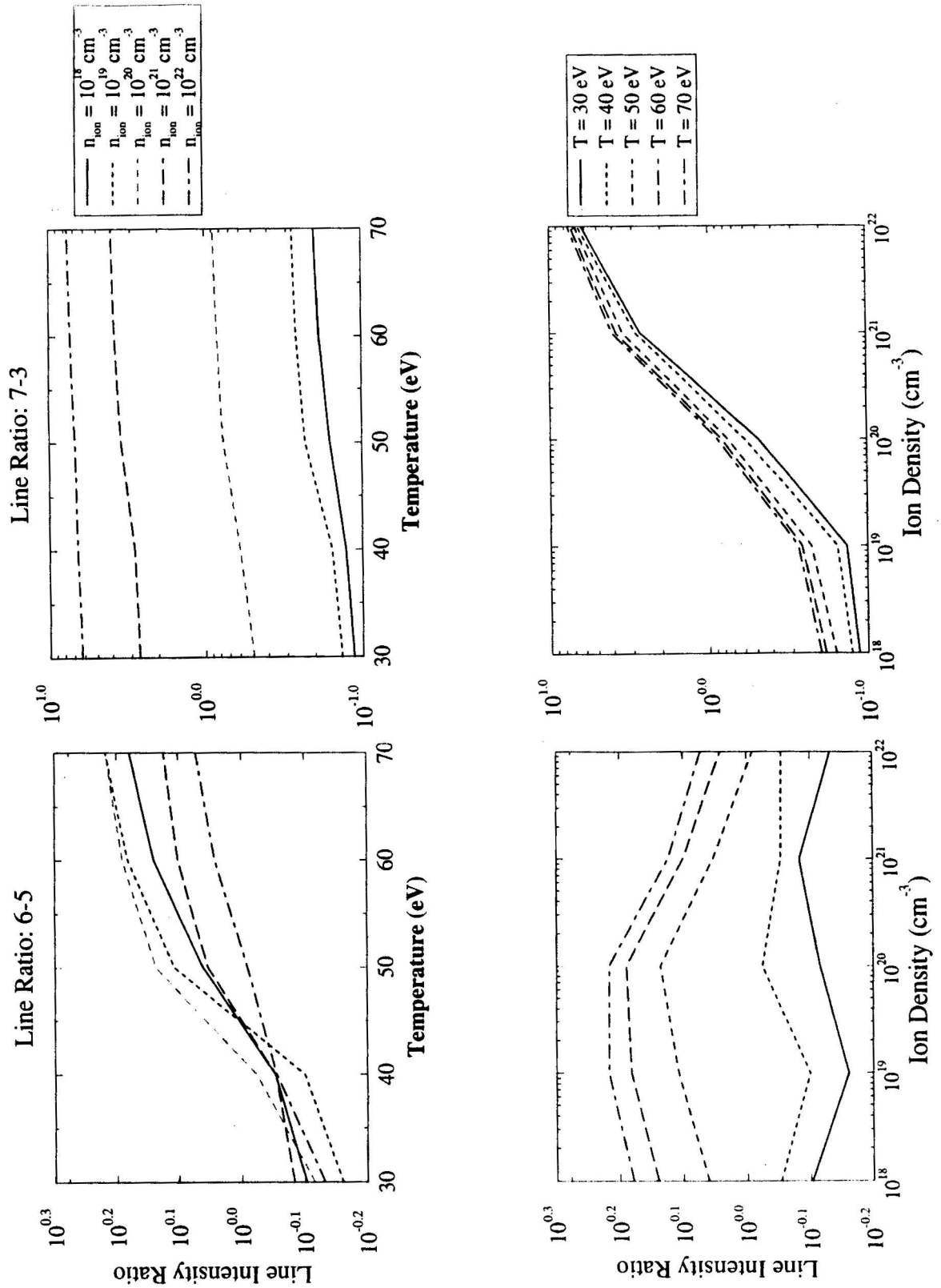

Figure 5.4(f). Calculated line intensity ratios for Al. Line definitions are given in Table 5.1.

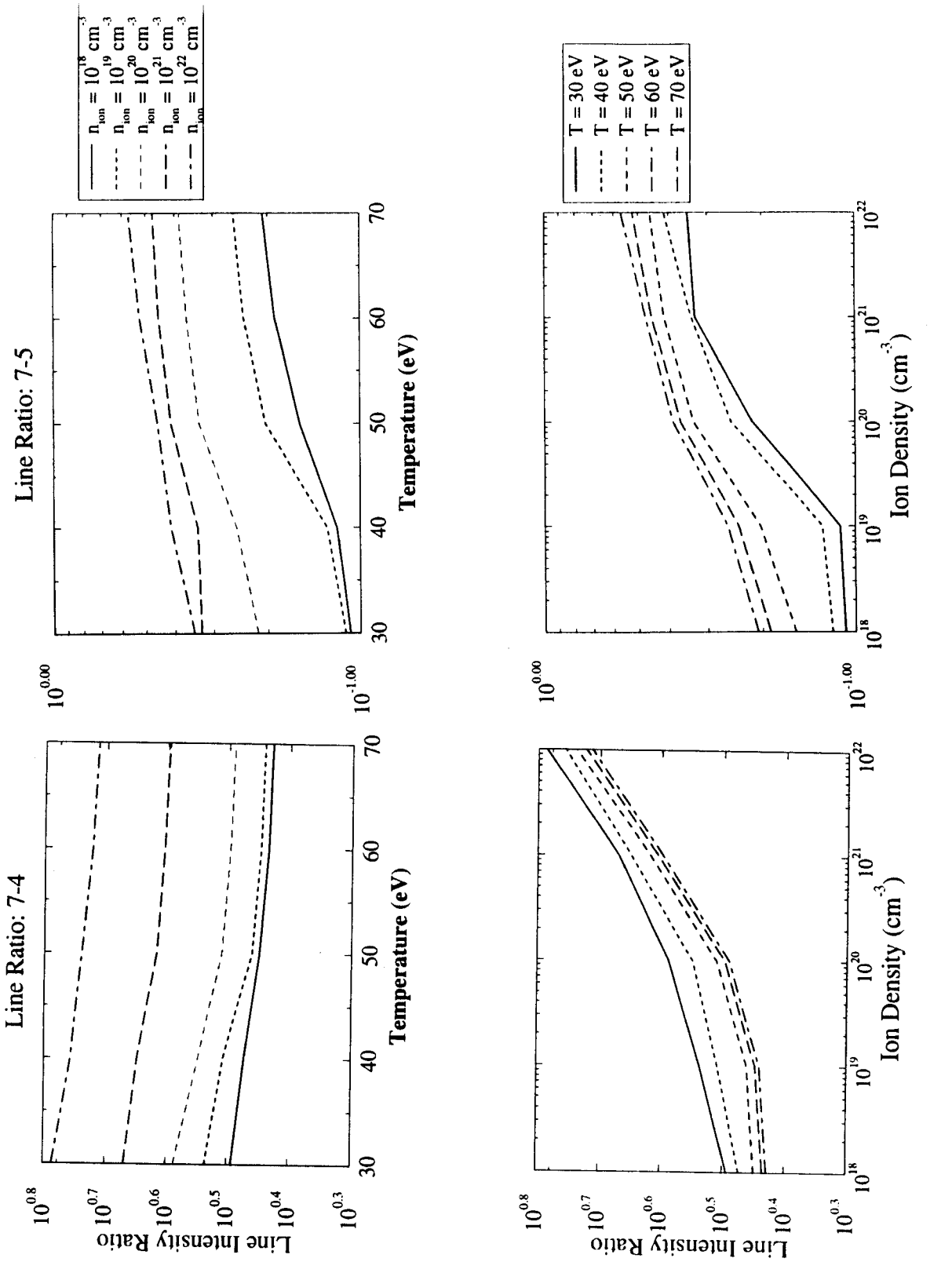

Figure 5.4(g). Calculated line intensity ratios for Al. Line definitions are given in Table 5.1.

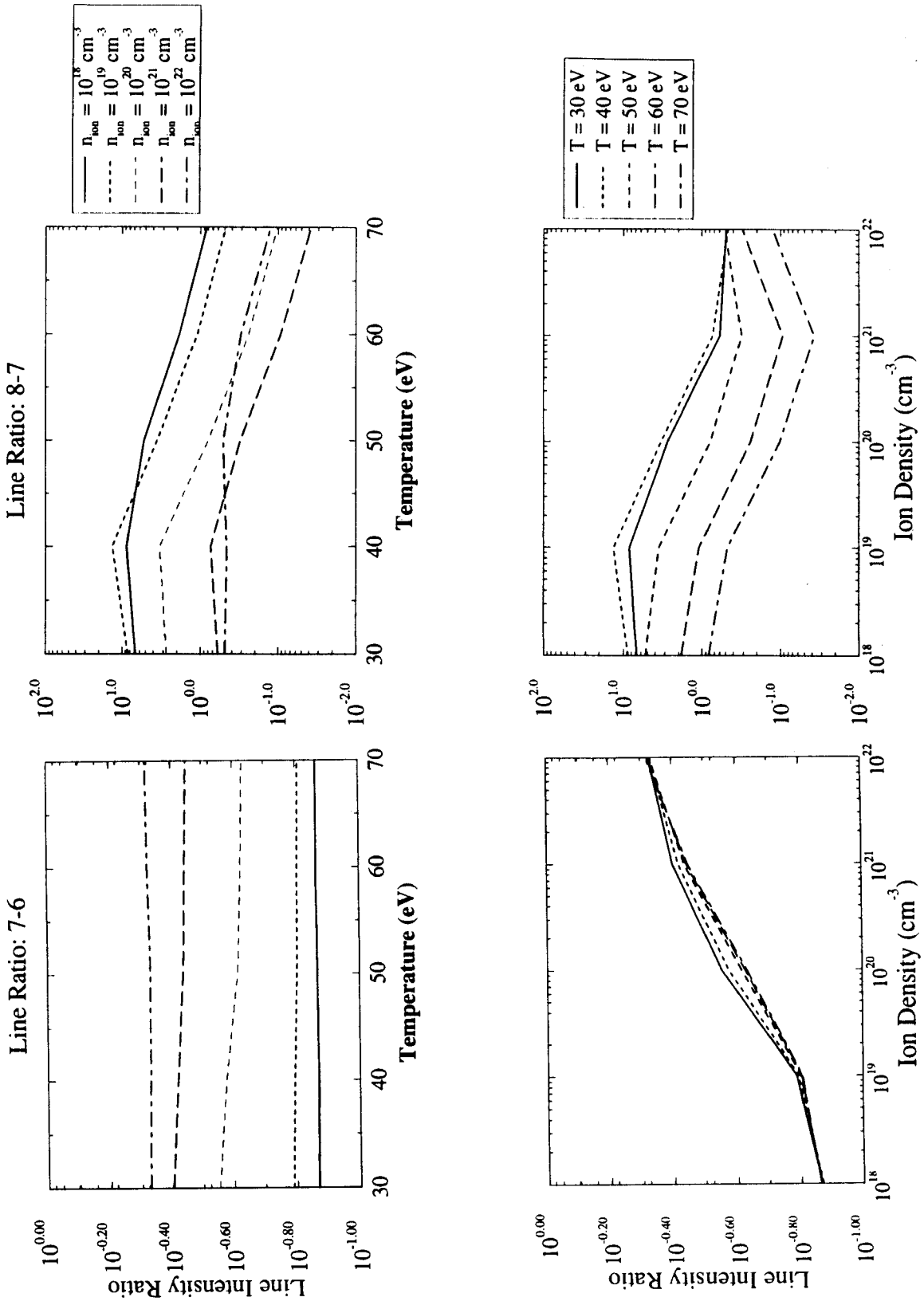

Figure 5.4(h). Calculated line intensity ratios for Al. Line definitions are given in Table 5.1.

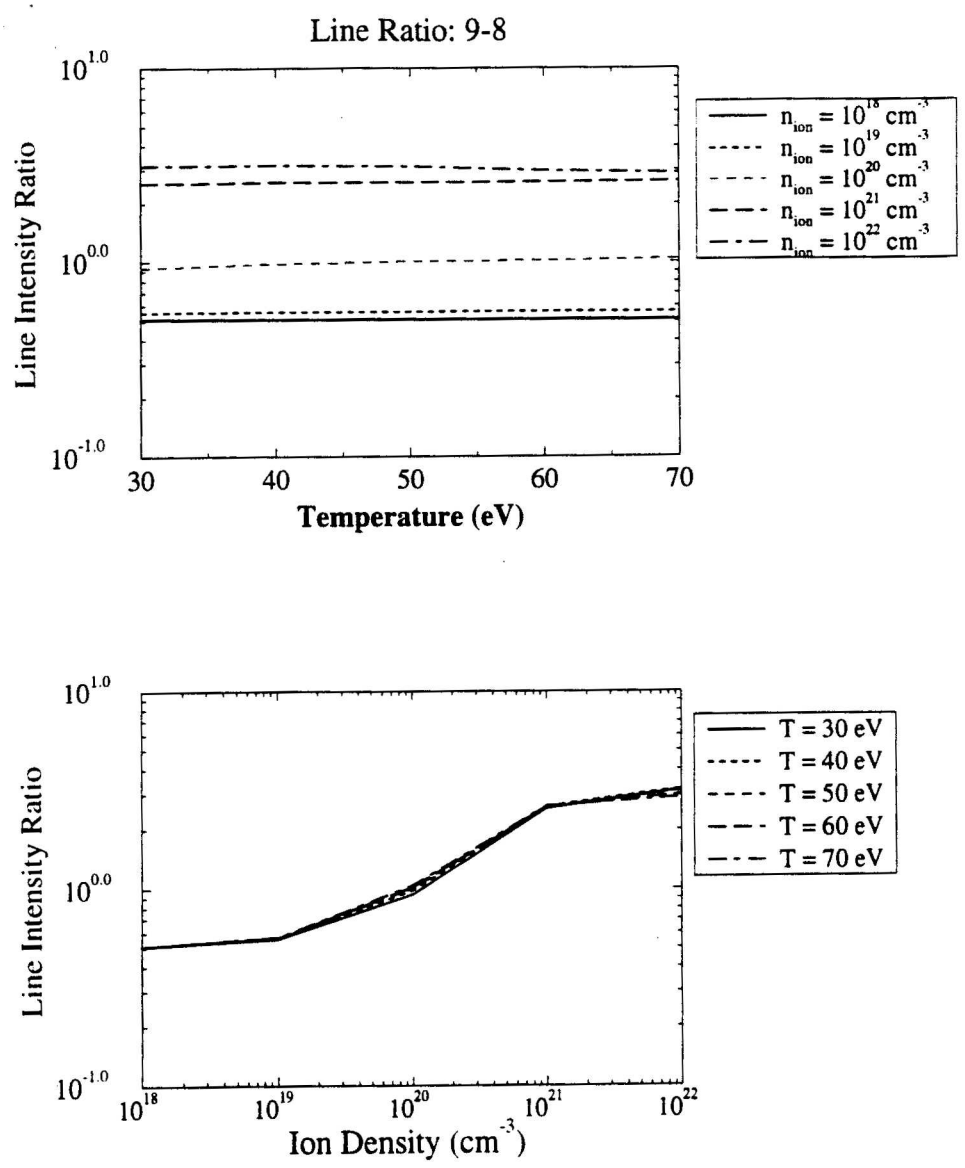

Figure 5.4(i). Calculated line intensity ratios for Al. Line definitions are given in Table 5.1.

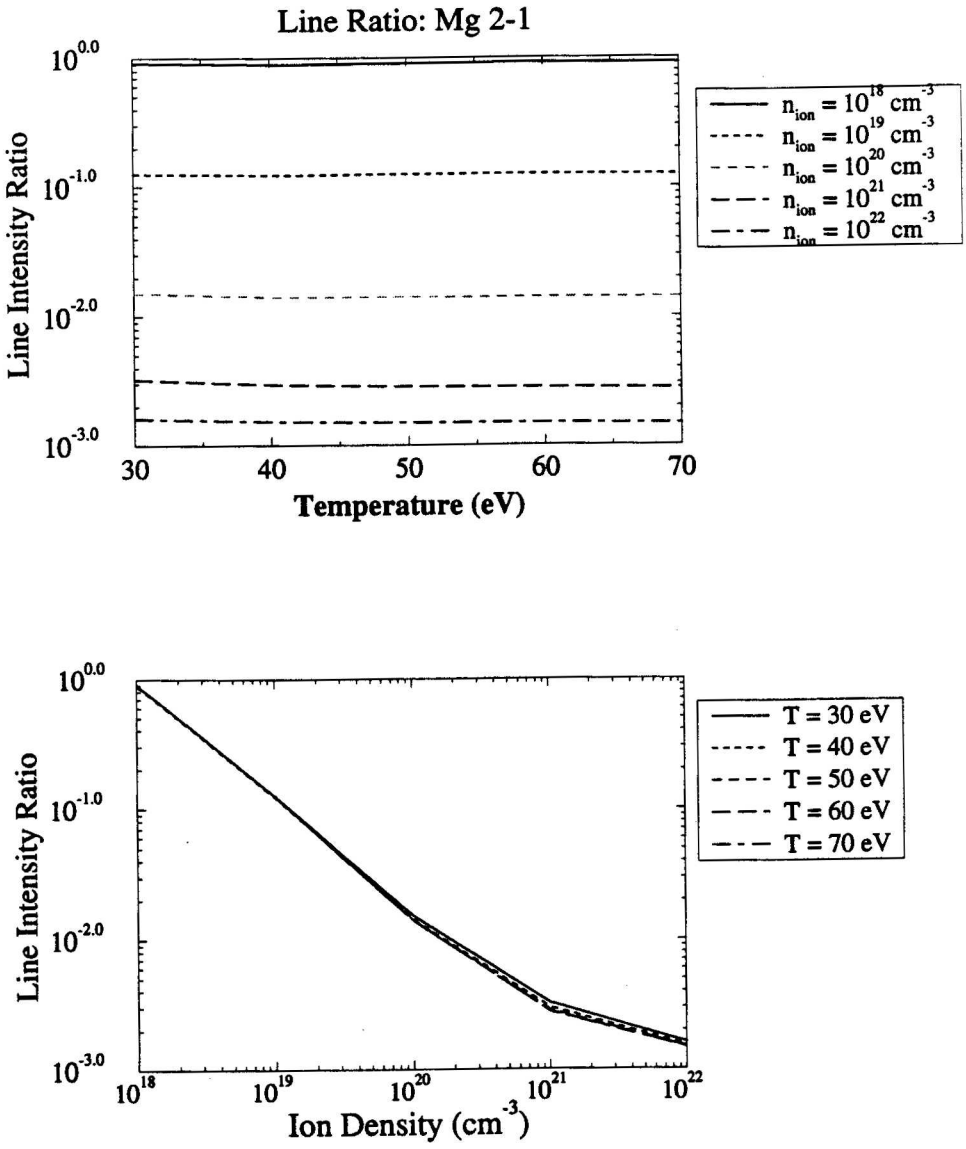

Figure 5.5(a). Calculated line intensity ratios for Mg. Line definitions are given in Table 5.1.

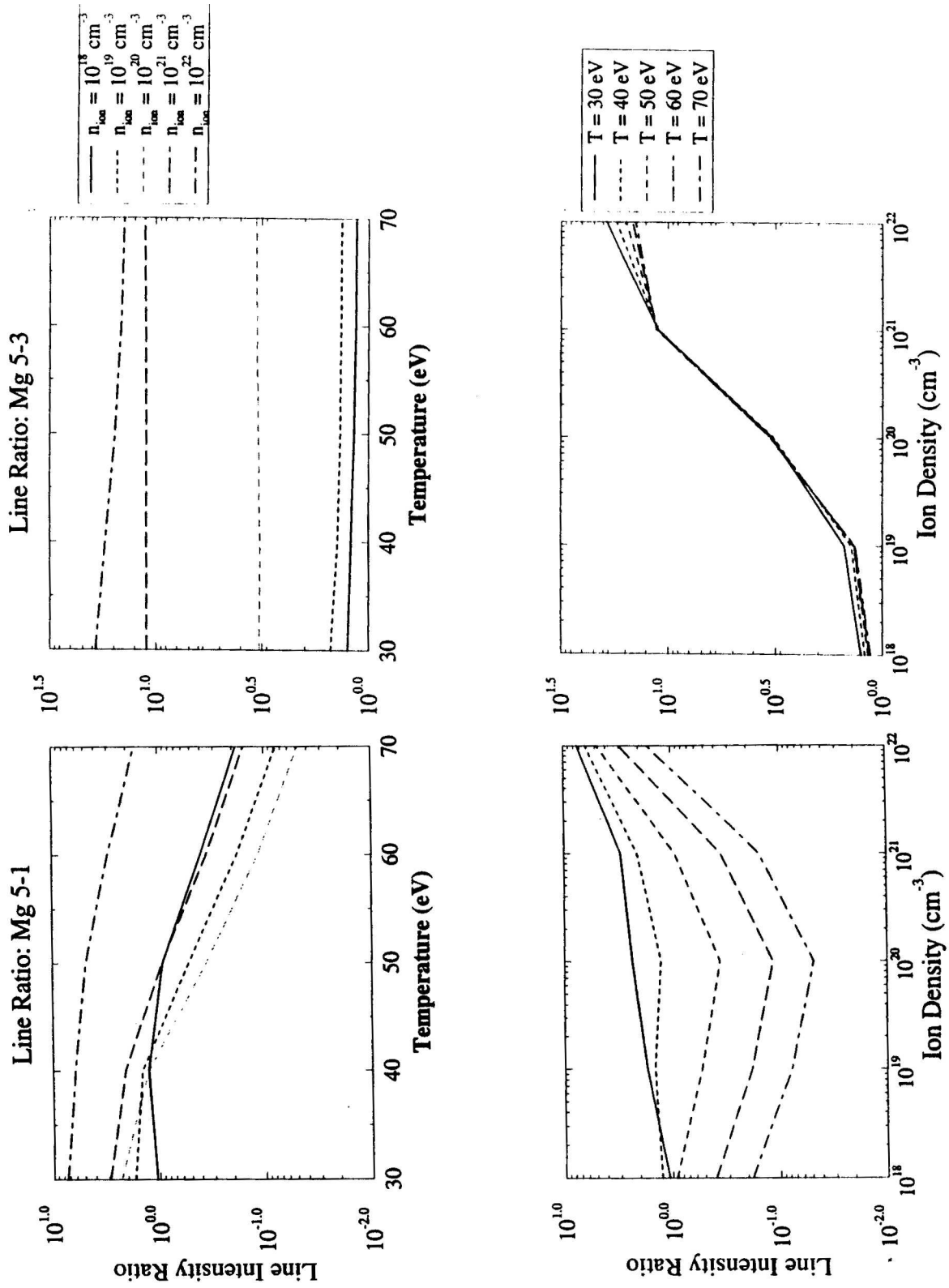

Figure 5.5(b). Calculated line intensity ratios for Mg. Line definitions are given in Table 5.1.

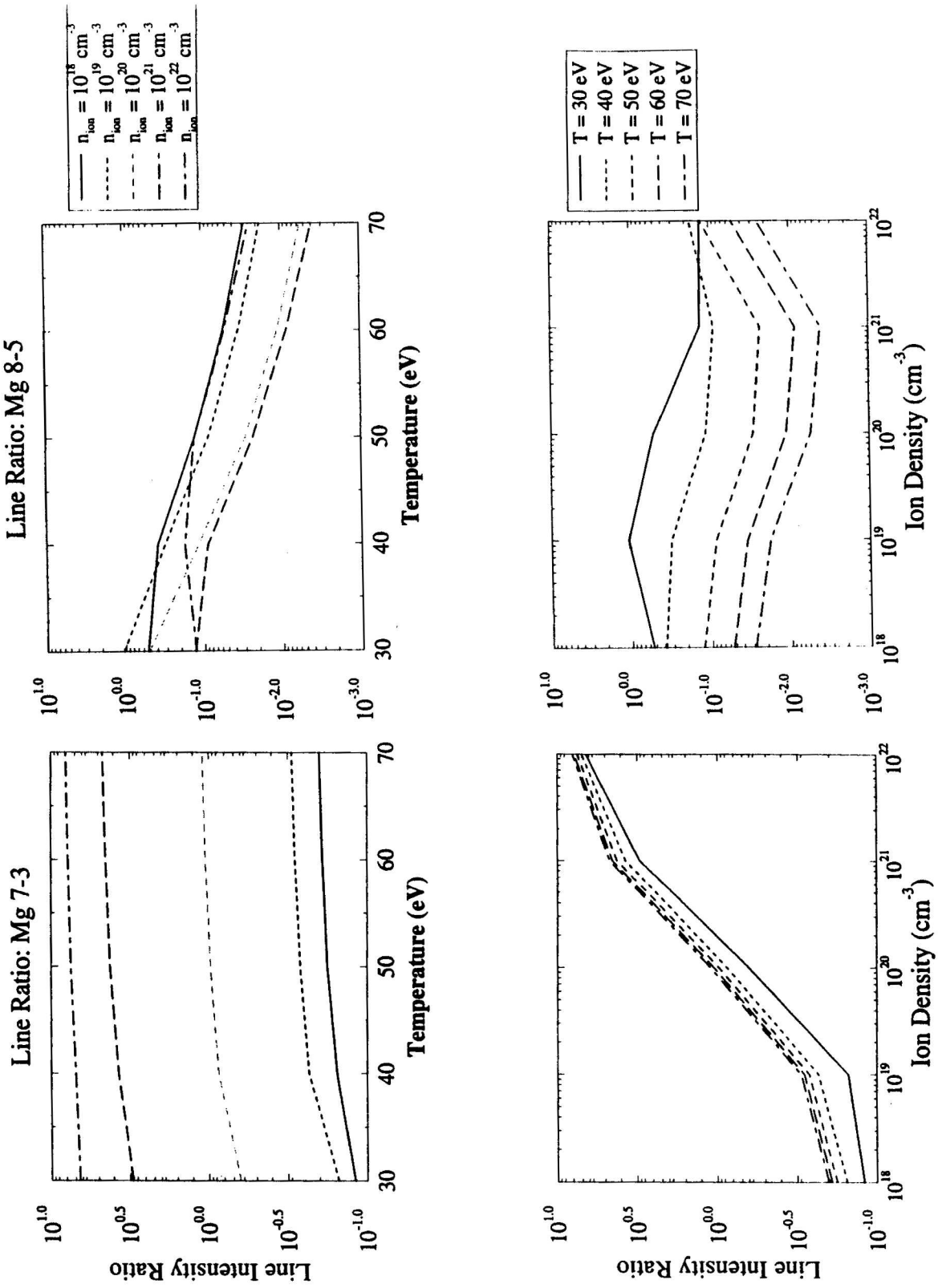

Figure 5.5(c). Calculated line intensity ratios for Mg. Line definitions are given in Table 5.1.

Figures 5.4 and 5.5 show some potentially useful density diagnostics; in particular the 5/3 and 7/6 Li-like ratios. The He-like intercombination-to-resonance line ratio could be used in principal, but it seems unlikely that the intercombination line would be strong enough in PBFA-II experiments to be useful. Note that lines 5 and 6 for Al correspond to the two features observed at about 7.85 Å in the recent experiments. The intensities for line 3 (λ = 7.868 Å) were probably slightly too low to be observed in previous experiments, but may be observed in future experiments.

The reason for the density dependence of the 7/6 ratio is that the populating mechanism for the autoionizing levels ($1s^1\,2p^2\,{}^2P$ and $1s^1\,2p^2\,{}^2D$) changes from being dominated by direct beam impact ionization at low densities, to be dominated by electron impact excitation from lower autoionizing levels at higher densities. The former is independent of the electron density while the latter is proportional to it.

The results to date should be considered preliminary. We anticipate looking in more detail at potential target plasma diagnostics in the coming year.

Acknowledgment

Support for this work has been provided by the U.S. Department of Energy.

References

Abramowitz, M., and Stegun, I.A., "Handbook of Mathematical Functions," (Dover, New York, 1965).

Bailey, J., Carlson, A.L., Chandler, G., Derzon, M.S., Dukart, R.J., Hummel, B.A., Johnson, D.J., Lockner, T.R., Maenchen, J., McGuire, E.J., Mehlhorn, T.A., Nelson, W.E., Ruggles, L.E., Stygar, W.A., and Wenger, D.F., *Lasers and Particle Beams* **8**, 555 (1990).

Bailey, J., personal communication (1993).

Basbas, G., Brandt, W., and Laubert, R., *Phys. Rev.* **A17**, 1655 (1978).

Bhalla, C.P., *Phys. Rev.* **A12**, 122 (1975).

Brandt, W., and Lapicki, G., *Phys. Rev.* **A23**, 1717 (1981).

Chen, M.H., and Crasemann, B., *Phys. Rev.* **A12**, 959 (1975).

Chen, M.H., Crasemann, B., Karis, K.R., and Mark, H., *Phys. Rev.* **A24**, 1852 (1981).

Combet Farnoux, F., in "Electronic and Atomic Collision" Abstracts of the 14th I.C.P.E.A.C, Palo Alto, California, USA, p.546 (1985).

Combet Farnoux, F., *Journal De. Physique* Colloque C9, Supplement 12, 199 (1987).

Cowan, R.D., "The Theory of Atomic Structure and Spectra," (University of California Press, Berkeley, 1981).

Datz, S., Duggan, J.L., Feldman, L.C., Laegsgaard, E., and Anderson, J.U., *Phys. Rev.* **A9**, 192 (1974).

Dukart, R.J., and Mehlhorn, T.A., personal communication (1993).

Duston, D., and Davis, J., *Phys. Rev. A* **21**, 1664 (1980).

Hansteen, J.M., and Hosebekk, O.P., *Phys. Rev. Lett.* **29**, 1361 (1972).

Hill, K.W., Doyle, B.L., Shafroth, S.M., Madison, D.H., and Deslattes, R.D., *Phys. Rev.* **A13**, 1334 (1976).

Hopkins, F., Elliott, D.O., Bhalla, C.P., and Richard, P., *Phys. Rev.* **A8**, 2952 (1973).

Hopkins, F., Brenn, R., Whittemore, A.R., Cue, N., Dutkiewicz, V., and Chatarredi, R.P., *Phys. Rev.* **A13**, 74 (1976).

Kauffman, R.L., McGuire, J.H., and Richard, P., *Phys. Rev.* **A8**, 1233 (1973).

Kessel, C., and Rudd, M.E., *Phys. Rev.* **A2**, 1327 (1970).

Lapicki, G., and Zander, A.R., *Phys. Rev.* **A23**, 2072 (1981).

MacFarlane, J.J., Wang, P., and Moses, G.A., University of Wisconsin Fusion Technology Institute Report UWFDM-822 (1990).

MacFarlane, J.J., Wang, P., and Henderson, D.L., University of Wisconsin Fusion Technology Institute Report UWFDM-847 (1991).

MacFarlane, J.J., Wang, P., Bailey, J., Mehlhorn, T.A., Dukart, R.J., and Mancini, R.C., *Phys. Rev. E*, in press (1993).

Madison, D.H., and Merzbacher, E., in "Atomic Inner-Shell Processes," edited by B. Crasemann (Academic Press, New York, 1975), Vol. 1, p. 1.

McGuire, E.J., *Phys. Rev.* **A10**, 32 (1974).

McGuire, E.J., *Phys. Rev.* **52**, 7075 (1981).

McGuire, J.H., and Richard, P., *Phys. Rev.* **A8**, 1374 (1973).

Nardi, E. and Zinamon Z., *J. Appl. Phys.* **A13**, 1334 (1976).

Richard, P., Kauffman, R.L., McGuire, E.H., Moore, C. Fred, and Olsen, D.K., *Phys. Rev.* **A8**, 1369 (1973).

Wang, P., MacFarlane, J.J., and Moses, G.A., submitted to *Phys. Rev.* (1993).

Watson, R.L., Benka, O., Parthasaradhi, K., Maurer, R.J., and Sanders, J.M., *J. Phys. B: At. Mol. Phys.* **16**, 835 (1983).

Appendix A

Analysis of K_α Line Emission from Aluminum Plasmas Created by Intense Proton Beams

J.J. MacFarlane, P. Wang, J. Bailey,
T.A. Mehlhorn, R.J. Dukart, R.C. Mancini

(Submitted to Physical Review)

Abstract

X-ray satellite line emission from targets irradiated by intense light ion beams can be used to diagnose plasma conditions and beam properties. We present results from our analysis of the first spectroscopic measurements of x-ray K_α satellites emitted from a target irradiated by an intense light ion beam. In this experiment, performed on the Particle Beam Fusion Accelerator-II device at Sandia, an Al target was irradiated with a 4-6 MeV proton beam with a peak power density of 1-2 TW/cm^2. Up to 15 percent of the beam electrical current was in the form of carbon contaminants. A time-integrated spectrum was obtained with a resolution of $\lambda/\Delta\lambda > 1200$. In our analysis, collisional radiative equilibrium (CRE) calculations were performed to study the dependence of the Al K_α emission spectrum on plasma and beam properties. Good agreement is obtained between calculated satellite spectra and the emission features observed in the experimental spectrum. We find that excited states with M-shell spectator electrons contribute significantly to K_α satellite emission spectra, exhibiting relatively broad lines at wavelengths blue-shifted with respect to those originating from ground state configurations. Because of opacity effects, it is likely that only radiation emitted from the outer skin of the target plasma was seen by the detector in the experiment. It is also shown that resonant self-absorption can skew the spectrum towards apparent higher ionization stage. Our results suggest that emission spectroscopy of x-ray satellite lines from thin tracer layers offers a potentially valuable technique for determining plasma conditions in intense light ion beam experiments.

I. Introduction

Spectroscopic observation of x-ray lines resulting from inner-shell transitions can be used to diagnose plasma conditions in targets irradiated by intense laser or ion beams. Absorption spectroscopy of K- and L-shell lines [1-7] has recently been used to diagnose plasma temperatures and densities in laser-produced plasmas and to measure opacities. For plasmas created by intense ion beams, emission spectroscopy can be used [8,9] because beam-induced ionizations produce K-shell vacancies which are subsequently filled during resonance fluorescence and autoionizing transitions. Thus, in addition to heating the target material the ion beam produces x-ray emission lines, thereby negating the need for a backlighter.

First spectroscopic observation of x-ray satellite lines in an intense proton beam experiment was recently made during a Particle Beam Fusion Accelerator II (PBFA-II) experiment at Sandia National Laboratories [8]. In this experiment an aluminum target was irradiated with a 4-6 MeV, 1-2 TW/cm^2 proton beam. An elliptic crystal spectrograph was used to obtain a time-integrated spectrum. Proton impact ionization of K-shell electrons populates autoionizing states, which then produce fluorescence line emission during K_α ($2p \rightarrow 1s$) transitions. Because of changes in electron screening effects, the K_α lines from Ne-like to He-like Al exhibit small, but detectable shifts to shorter wavelengths. The complete spectrum thus consists of neutral-atom K_α lines plus a series of blue-shifted satellites. K_α line spectra can therefore provide a measure of the ionization distribution in a plasma, and from that, constraints on plasma conditions.

The purpose of this investigation has been twofold: (1) to develop a good understanding of the physical processes that affect the K_α spectrum from targets heated by intense ion beams, and (2) to investigate the plasma conditions attained during the experiment reported in Ref. 8. In regards to the first item, we have studied several processes in detail. First, we have examined the contributions from excited states (i.e.,

states which were thermally excited prior to proton impact) to K_α emission spectra. Second, we have studied the relationship between temperature, ionization distribution, and K_α spectrum, and the effect line opacity has on skewing the resulting spectrum toward apparent higher ionization state. And third, in a separate set of calculations the sensitivity of K_α satellite line profiles to temperature and density was examined.

In regards to our second goal, two features about the target complicated our analysis: opacity and geometry. Part of this stems from the fact that the primary objective of the experiment reported in Ref. 8 was not to diagnose plasma temperatures. The thickness of the Al target (75 μm) was dictated by the stopping range of 5 MeV protons. At this thickness optical depths for both the x-ray continuum and K_α lines exceed unity. Additional complexity is introduced by the experiment geometry: the ions are accelerated from a barrel-shaped diode and irradiate a conical target. The shape of the expanding target plasma can only be calculated approximately with 1-D simulation codes. Despite these obstacles, we have been able to estimate the maximum plasma temperature attained in the *observable* part of the plasma, to qualitatively address the question of where the K_α photons seen by the detector originate, and the role of target heating by carbon ions in the beam. In addition, this study lays the groundwork for diagnosing plasma conditions in future experiments.

In our theoretical analysis, we have performed collisional-radiative equilibrium (CRE), atomic physics, line broadening, and hydrodynamic modelling calculations. Single-configuration and multiconfiguration Hartree-Fock calculations were performed to identify lines in the observed spectrum. Level populations and spectra were computed using a CRE code which models the effects of proton-impact ionization and radiation-induced transitions on the atomic level populations in addition to the usual collisional and radiative processes occuring in any hot laboratory plasma. The effects of opacity and the contribution of excited states with M-shell spectator electrons have been examined

in detail. To study the sensitivity of line profiles to the plasma conditions, Stark line broadening calculations were performed for several of the F-like and O-like Al lines using a code which includes broadening effects due to both electrons and ions. Radiation-hydrodynamic simulations were performed to predict the time-dependent evolution of the target plasma conditions and to assess the potential for target heating by contaminant carbon ions in the beam. Beam properties for the hydrodynamics simulations were obtained from particle-in-cell (PIC) calculations.

The outline of this paper is as follows. In Section II we summarize the experimental setup and spectroscopic measurements. An overview of our theoretical models is presented in Section III. In Section IV we discuss in detail physical processes which affect the K_α spectrum. In Section V we present results from hydrodynamic simulations of the PBFA-II experiment and a series of CRE calculations based on hydrodynamic predictions. We compare calculated and experimental spectra, and discuss the ramifications of our results for determining experimental plasma conditions. A summary of this investigation is presented in Section VI.

II. Experimental Setup and Measurements

An experiment to assess the potential for using K_α satellite emission as a plasma diagnostic has recently been performed with an intense proton beam generated by PBFA-II [8,10,11]. The accelerator electrical power pulse is converted into an ion beam using the applied-B diode [12] shown schematically in Fig. 1. This configuration is known as a "barrel" diode because ions accelerate radially inward from the azimuthally symmetric anode (the "barrel") toward a target at the center. Present target experiments use a proton beam generated with this diode, while focussing of intense lithium beams is under development. The beam parameters during this target experiment were not measured directly because the target geometry and diagnostic package were optimized for target response, rather than determining the focal quality of the beam. Nominal parameters on

shots with similar diode voltage and current were determined with an extensive array of beam diagnostics [13]. These shots delivered 50-75 kJ of protons to a 1 cm diameter spot with a pulse width of 15-20 ns and a voltage at peak ion power of 4-6 MV. The specific power density incident on the target described in this paper was thus approximately 50-100 TW/g, providing a unique opportunity for exploring ion beam heated matter.

The x-ray spectrograph used for this experiment is designed to obtain high spectral resolution while coping with the severe experimental environment on PBFA-II. The rate of performing experiments on PBFA-II is presently limited to one per day. Another difficulty is the 5-10 MeV endpoint bremsstrahlung, generated by electron losses in the diode, that bathes instruments 1 m from the diode with a dose rate of $10^{12} - 10^{13}$ Rad(Si)/s. We overcome this problem by using a 1000 kg tungsten housing to provide about 10 cm of shielding around the spectrograph.

Time-integrated space-resolved x-ray spectra are acquired on PBFA-II using an elliptical crystal spectrograph [14] operated in the Johann focussing mode [14-16]. This essentially renders source broadening negligible, a crucial consideration since the scale size of the plasma heated by the ion beam is of order 1 cm, in contrast to laser-produced plasmas which are typically of order 100 μm. The elliptical geometry also has the advantage that the detector is isolated from the line of sight by the structure of the slit placed at the ellipse focus, reducing both the debris and the scattered x-rays incident on the detector. This is important because the debris created by the large energy delivered to the diode routinely destroys the x-ray crystal, but the elliptical geometry preserves the detector. A 0.5 mm space-resolving slit provides 1 mm space resolution at the target (magnification = 1), in addition to reducing the debris which enters the instrument itself. The PET crystal was curved [17] to an ellipse with eccentricity 0.9188 and height parameter 4.1656 cm. The range covered in first order was 6.4-8.66 Å. The experimentally-determined spectral resolution was $\lambda/\Delta\lambda > 1200$. The spectrum was

recorded on Kodak DEF film, developed 5 min in Kodak Liquid X-Ray developer at 68°F. The data below is corrected for the film response [18,19], including the dependence on the angle of incidence in the Johann geometry.

A K_α spectrum from an aluminum target heated by the PBFA-II ion beam is shown in Fig. 2. The target was a 75 μm thick aluminum cone, with a half-angle of 15° and a midplane diameter of 14 mm. This thickness corresponds to one-half the range of 5 MeV protons in the cold material. The satellites corresponding to an increasing number of L-shell vacancies are clearly visible in Fig. 2. Analysis described in Ref. 8 ruled out the possibility that the satellites could have been produced via multiple ionization induced by carbon contamination in the beam. These satellites thus are due to vacancies produced by thermal ionization in the target, followed by proton-induced inner-shell ionization. The labeling of the satellite peaks corresponds to the ionization stage prior to the inner-shell ionization; the details of the line identifications are given below.

The wavelength scale in Fig. 2 is applied using the properties of the elliptical geometry, with the Al I K_α line (8.340 Å) serving as the standard. Imperfections in the Johann curve or the ellipse may cause deviations of the wavelength scale from the expected functional dependence. Calibration spectra obtained using a Manson source were used to evaluate the accuracy of the wavelength scale. We found that in the region 7.9-8.34 Å, the wavelengths were accurate to better than ±4 mÅ. In addition, there is a wavelength uncertainty due to the assignment of the peak intensity of the strongest line in the PBFA-II spectrum to be Al I. It is possible that the peak intensity actually corresponds to a higher ionization state (e.g., Al II or III), which would result in a systematic red shift of the entire spectrum by 2-3 mÅ [20]. The total experimental wavelength uncertainty is therefore comparable to the uncertainty in the theoretical wavelength predictions described below.

An estimate of the absolute measured photon flux emitted by the target was made in order to assist in interpreting the target opacity. We used the geometrical factors given in Ref. 18 and a crystal reflectivity of 0.5 mR [21]. Assuming uniform emission into 4π, the energy emitted in the Al I–IV line was estimated to be 0.16 J. The faintest line emission observed was about 2 mJ (the peak labeled Al VIII in Fig. 2), close to the estimated threshold for detection with this instrument. In the absence of an absolute calibration, these estimates are probably reliable to a factor of three.

III. Theoretical Models

To study the physical processes affecting the K_α spectrum we have used a combination of atomic physics, collisional-radiative equilibrium, and hydrodynamics codes. We now briefly describe the major features of each model.

A. CRE Model

In our CRE model atomic level populations are determined by solving multilevel, steady-state atomic rate equations [22]. Transitions considered include collisional excitation, deexcitation, ionization, and recombination; radiative and dielectronic recombination; and spontaneous decay. We also include the effects of the beam (proton beam impact ionization of inner-shell electrons and autoionization), and in some cases, the radiation field (photoexcitation and photoionization). In this detailed configuration accounting model each state of a given ion was coupled to all other states (ground and excited) of that ion, as well as all states of the next high ionization stage. Radiation is transported using either of 2 models: (1) an angle- and frequency-averaged escape probability model [22,23], or (2) a multiangle, multifrequency model [24] which solves a second order form of the transfer equation. Several calculations were performed with radiation effects included for a range of plasma conditions relevant to the PBFA-II experiment discussed in Section II. It was found that there was virtually no difference

in calculated K_α satellite spectra between these calculations and those in which LTE populations were assumed. (This is not expected to be the case in future experiments in which significantly higher plasma temperatures will be achieved.)

To compute spectral properties we consider emission and absorption from bound-bound, bound-free (including inner-shell attenuation), and free-free transitions. Voigt line profiles are used which include the effects of natural, Auger, Doppler, and Stark broadening. In the CRE calculation, Stark line broadening is modeled in the electron impact approximation. The semiclassical model of Griem [25] is used in conjunction with Hartree-Fock results for radial matrix elements and transition energies to the nearest dipole-allowed levels. More detailed Stark broadened line profiles were computed for some of the K_α lines; these results will be presented in Section IV.

The proton-impact ionization rate can be expressed as

$$R^P_{ii^*} = n_i \, J \, \sigma_K(E_B) \,, \tag{1}$$

where J is the current number density (particles cm^{-2} s^{-1}), σ_K is the K-shell ionization cross section, E_B is the beam energy, n_i is the number density of particles in the initial state i, and i^* represents the index of the final (autoionizing) state. In the CRE calculations described below we have assumed the beam to be spatially uniform and monoenergetic. Autoionizing states are depopulated by two mechanisms: a resonance fluorescence in which a photon of energy ≈ 1.5 keV is emitted, or an autoionization in which a second electron is ejected. The two rates are given by:

$$\begin{aligned} R_{i^*j} &= n_{i^*} \, A_{i^*j} && \text{(fluorescence)} \\ R_{i^*\kappa} &= n^*_i \left(\tfrac{1-Y_{i^*}}{Y_{i^*}}\right) \textstyle\sum_j A_{i^*j} && \text{(autoionization)} \end{aligned} \tag{2}$$

where A_{i^*j} is the Einstein coefficient for $i^* \rightarrow j$, and Y_{i^*} represents the fluorescence yield. For each ionization stage we have used the configuration-averaged fluorescence yields of McGuire, which are tabulated in Ref. 26. The final state of all autoionization

transitions, κ, is assumed to be the ground state of the next higher ionization stage (for Al, multi-electron ejection via Coster-Kronig transitions is unimportant).

B. Atomic Physics Models

In our spectral calculations two different model atoms were used: one with fewer atomic levels and higher accuracy, the other with more levels but less accuracy. In the first case, our Al model atom consisted of 184 levels distributed over all 14 ionization stages. Of these 34 were autoionizing levels (Al I-XI ions with K-shell vacancies). Atomic structure calculations for levels involving K_α transitions were performed using a multiconfiguration Hartree-Fock (MCHF) code [27] with relativistic mass and Darwin corrections [28]. An L-S coupling scheme was used to define the angular momentum coupling of electrons. Details of these calculations are presented elsewhere [29]. The purpose of these calculations was to confidently determine the transitions most responsible for the observed peaks in the PBFA-II spectrum. Our second model atom consisted of a total of 750 energy levels distributed over all ionization stages. Roughly half of these were autoionizing levels. The additional levels primarily included excited state configurations with valence electrons in the $n = 3$ shell and their autoionizing counterparts. For this second data set, single configuration Hartree-Fock (SCHF) calculations were performed for all levels to determine transition energies and oscillator strengths. Reasonably accurate transition energies were obtained by including relativistic corrections for levels in ground state configurations. For excited state configurations no corrections were made as it was assumed that blue-shifting relativistic corrections are essentially cancelled by red-shifting electron correlation interactions [29]. Using this model we find good agreement with other published experimental results [7], indicating these approximations are quite reasonable.

Rate coefficients for collisional and radiative transitions were calculated as follows. Collisional excitation and ionization rates were computed using a combination

of semiclassical impact parameter, Born-Oppenheimer, and distorted wave models [30-32]. The corresponding inverse processes were specified from detailed balance arguments. Rate coefficients for dielectronic recombination were computed using a Burgess-Mertz model [33] in conjunction with Hartree-Fock energies and oscillator strengths. Photoionization cross sections and radiative recombination rates were obtained from Hartree-Fock calculations.

Proton impact ionization of K-shell electrons were calculated for each ionization stage of Al using a plane wave Born approximation (PWBA) model [34]. Computed cross sections for Al I, Al V, and Al X are shown in Fig. 3 as a function of proton energy. Also shown are experimental data for Al I [35,36]. The differences between the calculated and experimental data for Al I are seen to be comparable to the differences between the two sets of experimental data ($\sim$ a few tens of percent) at proton energies relevant to the PBFA-II experiment (> 1 MeV). Our calculations indicate that the cross section decreases with increasing ionization stage in a roughly linear fashion. A linear approximation was used in our CRE calculations.

C. Hydrodynamic and Beam Energy Deposition Models

Input required for performing the hydrodynamic simulations is an energy source term which describes the ion beam heating of the target. This was obtained by performing transport simulations for the experimental diode voltage and currents using the PICDIAG code [37] to determine the ion energy and intensity time histories of the beam striking the Al cone. Input to these simulations included the experimental geometry, such as the anode shape and gas cell configuration, as well as the diode voltage and currents for the specific shot. Beam divergence, current neutralization fractions, and ion species information from related setup shots were used. The effects of applied- and self-field bending of the multispecies ion beam (assumed to be composed of protons and C^{3+})

were included in the simulations, as were the effects of finite source divergence, multiple scattering during transport, and time-of-flight dispersion.

The target was modeled as a cylinder with a diameter equal to that of the cone midplane. Time- and space-dependent ion energies and beam intensities were tallied at the target location for each ion species. This information was then used as input to the hydrodynamic simulations.

A 1-D radiation-hydrodynamics code was used to calculate the time history of the temperature and density distributions in the target plasma. An analytic equation of state was used for the Al plasma [38]. The spatial dependence of the ion energy deposition was calculated for each species of the ion beam using a ion stopping model [39] which includes the effects of collisions between ions and free electrons in a hot plasma (range shortening effect).

IV. Physical Processes Affecting K_α Spectral Emission

A. Role of Excited State Transitions

K_α line radiation in light ion beam experiments is emitted as a result of two processes: ion-impact ionization of a $1s$ electron followed by a spontaneous fluorescence transition. We now examine the production of K_α line emission from ions of excited state configurations. (The role of such configurations in absorption experiments was recently reported in Ref. 6.) Consider the transition:

$$1s^2\,2s^2\,2p^3\,3\ell \underset{p-impact}{\rightarrow} 1s^1\,2s^2\,2p^3\,3\ell \underset{K_\alpha}{\rightarrow} 1s^2\,2s^2\,2p^2\,3\ell$$

where ℓ represents an s, p, or d subshell. K_α lines of this type differ in 2 important respects from those produced by ions originally in ground state configurations. First, the wavelength of a transition involving excited states is similar to that for a low-lying level of the next higher ionization stage. This occurs because the valence electron in the outer shell has little effect on the electronic wavefunctions in the inner regions of the

ion (an effect analogous to the Li-like dielectronic satellites which commonly appear in laser-produced plasma spectral lines on the long-wavelength side of the He-like resonance lines). This is illustrated in Fig. 4, where stick spectra (oscillator strength vs. wavelength) of the K_α lines for Al I-IX are shown. The ions are referred to by their stage prior to ion-impact ionization. The wavelengths were obtained from the SCHF calculations described above. The wavelength regions dominated by excited state configurations are bracketed by arrows while the remaining lines generally involve ground state and low-lying excitation state configurations. Looking at the region near 8.2 Å it is clear that many excited state lines from Al V reside in the same wavelength region as those from low-lying states of Al VI.

The second important difference between these two types of lines is that the plasma broadening effect on the lines involving excited states can be considerably larger. To study this effect in detail we have performed Stark broadened line profile calculations using a recently developed multielectron line shape formalism and code [40,41]. Broadening effects due to both electrons and ions were considered. The electron broadening effect was computed using a second order quantum relaxation theory while ion broadening was calculated using a microfield distribution function and the static ion approximation. In these calculations atomic physics data was computed using the atomic structure codes of Cowan and included multiconfiguration effects [42].

Figure 5 shows results from several sets of line profile calculations for low-lying states of O-like and F-like Al (Al V and IV prior to ion-impact ionization, respectively; in this paper we shall refer to the ionization stage after inner-shell ionization as O-like, F-like, etc., and the stages prior to inner-shell ionization as Al V, Al VI, etc.). The line shapes are area normalized; opacity effects are not included. Figure 5(a) shows the contribution from several broadening mechanisms for the K_α lines of O-like Al at $T = 20$ V and $n_e = 10^{23}$ cm^{-3}. For these calculations, 6 upper energy levels

(corresponding to configurations $1s^1\,2s^2\,2p^5$ and $1s^1\,2s^1\,2p^6$) and 10 lower energy levels (corresponding to configurations $1s^2\,2s^2\,2p^4$, $1s^2\,2s^1\,2p^5$, and $1s^2\,2p^6$) were considered. The relative transition strengths were calculated assuming LTE. The 3 prominent features are dominated by transitions from upper energy levels in the configuration $1s^1\,2s^2\,2p^5$. The solid curve includes the effects of Stark and Doppler broadening. The long-dashed curve includes the additional effects due to the widths associated with radiative and Auger decay using the model described in Ref. 43. The widths associated with Doppler broadening and radiative decay are relatively small (0.6 mÅ and 0.06 – 0.16 mÅ, respectively). However, the Auger decay effects are much larger (widths ~1.6 – 2.2 mÅ) and have a significant impact on the line shape. The short-dashed line represents the profile convolved with a Gaussian of 5.3 mÅ FWHM to approximate instrumental broadening effects in the PBFA-II experiment. Figure 5(b) shows a series of calculations at different densities for O-like Al with all broadening effects described above included. It is clear from these results that Stark broadening is not important for these lines at electron densities below about 2×10^{23} cm^{-3}. At the lower densities the Auger and eventually, instrumental widths dominate.

Figure 5(c) shows the density sensitivity of line profiles for transitions arising in excited state configurations of F-like Al; that is, with one spectator electron in the $n = 3$ shell. Upper energy levels of these transitions have configurations of the type $1s^1\,2s^2\,2p^5\,3\ell$ and $1s^1\,2s^1\,2p^6\,3\ell$ ($\ell = s, p, d$). The spectrum is dominated by transitions coming from the $1s^1\,2s^2\,2p^5\,3\ell$ configuration. For the results displayed in Fig. 5(c) we considered 48 upper energy levels of the type $1s^1\,2s^2\,2p^5\,3\ell$ and 57 lower energy levels of the type $1s^2\,2s^2\,2p^4\,3\ell$. These lines show a much more pronounced dependence on electron density than those for the O-like case at these densities. The presence of the $n = 3$ electron makes these states easier to perturb by the plasma microfields. Thus,

the K_α lines resulting from excited state configurations offer better opportunities for diagnosing plasma densities in the range of densities relevant to the PBFA-II experiment.

To determine whether lines from excited state configurations should make a significant (observable) contribution to K_α emission spectra obtained in light ion beam experiments, we performed two CRE calculations which were identical except for the number of autoionizing states in our atomic model. In the first calculation only autoionizing states which originated as ground state configurations were considered, while in the second calculation we included autoionizing states of the type $1s^1\,2s^1\,2p^{w-1}$ and $1s^1\,(2s\,2p)^{w-1}3\ell$. In the latter case a total of 624 energy levels were considered in the atomic model. In each calculation the plasma was assumed to be a planar slab of width $L = 0.1$ μm, $T = 30$ eV, and $n = 10^{-1}\,n_0$ ($n_0 \equiv$ solid density).

The resulting satellite spectra are shown in Fig. 6. Comparison of the spectra calculated with (solid curve) and without (dotted curve) excited state configurations included shows that excited states are clearly important contributors. In addition to more relatively narrow features appearing in the spectrum from $1s^1\,2s^1\,\,2p^{w-1}$ configurations, broader features from the $1s^1\,(2s\,2p)^{w-1}3\ell$ configurations are very apparent.

As a direct comparison with the time-integrated PBFA-II spectrum a similar set of calculations was performed for the following conditions: $T = 20$ eV, $n = 10^{-1}\,n_0$, and $L = 100$ μm. (These conditions are consistent with those predicted from hydrodynamic simulations of the PBFA-II experiment.) In the first calculation we used the MCHF atomic data set which included only low-lying and ground state configurations. Figure 7 shows the calculated (short-dashed curve) and experimental (solid curve) spectra in the narrow wavelength range which corresponds to emission from the ground state configuration of Al V. Note that the calculated spectrum exhibits much more narrow and pronounced peaks than the observed spectrum. The peak resulting from the $^1P \rightarrow\ ^1S$ transition is slightly higher than that of the $^1P \rightarrow\ ^1D$ transition — just the opposite of

what is observed in the experiment. It is also clear that in this calculation the intensity between the peaks is much lower than observed.

In the second calculation we used the SCHF data set, which is slightly less accurate but included many more excitation levels. The calculated spectrum for this case is given by the dashed line in Fig. 7. The most noticeable feature from this calculation is that the intensity between the peaks is filled in by K_α transitions involving excited states. This radiation is due to the superposition of many broad lines produced by transitions of the type $1s^1\,2s^2\,2p^5\,3\ell \rightarrow 1s^2\,2s^2\,2p^4\,3\ell$ and $1s^1\,2s^1\,2p^6\,3\ell \rightarrow 1s^2\,2s^1\,2p^5\,3\ell$. It is also seen that the peak of the ${}^1P \rightarrow {}^1S$ line is lower than that of the ${}^1P \rightarrow {}^1D$ line, which is in qualitative agreement with the experimental spectrum. This is caused by greater opacity for the ${}^1P \rightarrow {}^1S$ line arising from the other relatively broad lines. The calculated spectrum in this case shows the ${}^3P \rightarrow {}^3P$ and ${}^1P \rightarrow {}^1D$ lines to be somewhat narrow compared to experiment. This, at least in part, is due to instrumental broadening, which is not included in these calculations. Note, however, that instrumental broadening is not sufficient to fill the gaps between the peaks (see Fig. 5(a)) when excited states are not included.

B. Opacity Effects

In the PBFA-II experiment the thickness of the conical Al target was 75 μm, which is approximately equal to the half-range of 5 MeV protons in cold Al. This leads to two significant sources of opacity. First, the continuum optical depth due to L-shell photoabsorption for this thickness is about 7 – 8 over the frequency range of K_α emission. Because of this the spectrometer, which was located above the top of the cone, could see only those photons emitted from the outer "skin" of the plasma. Second, we find that optical depths for the K_α lines range up to $10^3 - 10^4$. This indicates that resonant self-absorption had a very significant impact on the observed spectrum.

One of the effects line opacity has is to skew the observed satellite spectrum toward higher ionization stages [9]. That is, ions with ionization stage higher than the most abundant stage can emit the greatest flux. This is shown in Fig. 8, where the calculated spectral intensity is plotted for planar Al plasmas of varying thickness. In each case the temperature was 35 eV and the density was $10^{-2}\, n_0$. The plasma thickness ranged from 10^{-4} cm to 1 cm, which corresponds to a solid density thickness of 100 Å to 100 μm. For the $L = 10^{-4}$ cm case, the optical depth at all frequencies was less than unity, and was greater than 10^{-1} for only the strongest lines. Therefore opacity has a relatively minor effect on its spectrum. In this case, the peak intensities come from N-like and C-like Al, which originate from the most abundant ionization stages. As the plasma thickness increases, the intensities of the B-like and Be-like Al lines increase, while those of the N-like and C-like Al lines do not because their optical depths exceed unity at $L \gtrsim 10^{-3}$ cm. (Note that the $L = 10^{-4}$ and $L = 10^{-2}$ intensities have been multiplied by 30 and 1.5, respectively.) For the $L = 1$ cm case B- and Be-like lines exhibit the greatest intensities even though they originate from ions whose fractions are calculated to be 0.10 and 0.007, respectively.

The optical depth for the $L = 1$ cm case is plotted in Fig. 9 as a function of wavelength. Optical depths are measured along a line of sight normal to the plane of the plasma. The optical depths are greatest for O-like and N-like lines. Even the strongest B-like lines — which involve $1s^1\, 2s^1\, 2p^2 \rightarrow 1s^2\, 2s^1\, 2p^1$ transitions — have optical depths ranging to $\sim 10^2$. The continuum optical depth from L-shell photoabsorption is about 7 - 8. The L-shell photoabsorption cross section is not extremely sensitive to ionization stage for Al I - Al X, and therefore the continuum opacity is only a weak function of the temperature. It is also important to note that for targets $\gtrsim 10^2$ μm thick the continuum opacity can significantly affect the observed line profiles. This causes

additional complications when trying to deduce plasma conditions from individual line profiles.

The results for the 1 cm case in Figs. 8 and 9 are relevant to the experiment described in Section II. That is, the line center optical depths for the strongest lines had values ranging up to $\sim 10^4$. Thus, the features labeled Al VIII and Al IX in the observed spectrum (Fig. 2) likely originated from a region of the plasma where Al VI and Al VII were the dominant ionization stages. Obviously, neglecting resonant self-absorption effects for such plasma conditions can lead to overestimating the actual plasma temperature. Opacity effects in future experiments can be mitigated by using thin tracer layers ($\sim$100-1000 Å thick) as the diagnostic medium.

V. Numerical Simulations of PBFA-II Experiment

In the radiation-hydrodynamic simulations the Al cone was modeled in 1-D as a 75-μm thick, 14-mm diameter cylinder with a central void. The target thickness corresponded to approximately one-half the range for protons at 5 MeV. Therefore, the protons initially deposit energy while travelling through one side of the cone and stopping in the other side. As the target is heated, the ion range decreases and the primary energy deposition then occurs only in the near side of the cone.

The current and particle flux of the carbon contaminant beam were $\lesssim 15\%$ and 5% of the total beam, respectively. Because of these seemingly low values only heating from protons was considered in our first series of calculations. These simulations, however, were not able to produce an electron temperature in the target plasma high enough to be consistent with the Al K_α satellite lines observed by the x-ray spectrometer. When heating by C^{+3} was added to the simulations the outer surface of the target plasma was heated to significantly higher temperatures. This occurs because C^{+3} ions have a significantly shorter stopping range than protons. Thus, the interior regions of the conical

target were heated primarily by protons in these simulations while the outer skin was heated by carbon ions.

For our hydrodynamic simulations a peak proton intensity of 2.4 TW/cm^2 and a peak C^{+3} intensity of 0.7 TW/cm^2 were used. The time history for the C^{+3} ions was predicted from PICDIAG simulations. About two-thirds of the energy deposited in the target was carried by the proton beam. However, since the carbon ions deposit their energy near the outer surface, they can have a strong effect on the temperature of that region. Because of the significant effect of opacity on the measured K_α spectrum, it is expected that the spectrometers observed emission only from the outermost skin of the target plasma.

Results from the radiation-hydrodynamic simulations which included effects of carbon heating are shown in Fig. 10. Shown are the temperature and density distributions as a function of radius at simulation times from 40 to 80 ns ($t = 0$ in the simulations corresponds to the time at which the machine is triggered.). The hollow cylindrical target starts at $r = 0.76$ cm and expands as it is heated. The peak temperatures in the interior regions of the target — i.e., the region heated by protons — are about 20 eV. The temperatures in the outermost regions reach a peak of about 55 eV at 90 ns. The maximum temperature in this region is attained at relatively late times because the peak current for the C ions lags that of the protons by about 25 to 30 ns. The target expands by a factor of roughly $10^2 - 10^3$ while the beam irradiates the target.

Using the results from the hydrodynamic simulations as a guide we performed a series of CRE calculations using characteristic plasma conditions at several stages of the target plasma evolution. The goal was to examine whether calculated spectra are consistent with the time-integrated experimental spectrum. In each case calculations were performed for isothermal slabs of width $L = 100\,\mu$m. (The results are insensitive to L if $L \gtrsim 30\,\mu$m because the plasma is optically thick at all wavelengths in the K_α spectral

region.) For the purpose of calculating beam impact ionization, the beam was assumed to be a spatially uniform, monoenergetic beam of 5 MeV protons. The following parameters were chosen to represent early, middle, and late stages of the plasma evolution:

T (eV)	n/n_0	$J_{protons}$ (MA/cm^2)
2.5	0.20	0.15
25	0.05	0.30
35	0.01	0.30

These conditions correspond roughly to the C-heated region of the plasma at simulation times of 45, 60, and 70 ns. Plasma conditions corresponding to later times (higher temperatures) are not included here because: (1) the proton current — i.e., the particles most responsible for producing the K_α emission — drops significantly at the later times; and (2) higher temperatures produce K_α satellites at shorter wavelengths than those observed by the x-ray spectrometer. While the C ions may play a significant role in heating the outer skin of the plasma — which, due to opacity effects, is likely the source of K_α photons seen by the detector — proton-impact ionization is primarily responsible for the observed spectrum [8].

Figure 11 shows the emission spectra computed for the T = 2.5 eV (top), 25 eV (middle), and 35 eV (bottom) cases. Note that the scale for the T = 2.5 eV case is reduced by a factor of 10. At 2.5 eV, the dominant ionization stages are Al I and II. The K_α lines for these ions lie very close together and appear as a single feature. The radiation from these lines is not inhibited by opacity effects because there are very few ions with $2p$ vacancies at this temperature. Because of this, the intensities from K_α lines from the lowest ionization stages are about an order of magnitude higher than the satellites from higher ionization stages. This indicates that the large flux coming from the Al I–IV peak in the experimental spectrum (see Fig. 2) very likely occurred during the early phases of the plasma evolution when temperatures were $\lesssim$ 5 eV.

For the $T = 25$ eV case the dominant ionization stage is Al IV. Despite this the highest intensity comes from K_α transitions in N-like Al which originates as Al VI. This effect is caused by resonant self-absorption. The line intensities in this case are ~ 10 times lower than in the $T = 2.5$ eV case due to line opacity effects. The peak flux from the $T = 35$ eV case is from Be-like and B-like Al. This wavelength region — which may also contain contributions from lines originating from excited states of Al VIII — corresponds to the shortest wavelength peak observed in the PBFA-II spectrum. Similar calculations were run at several other densities ($n = 2 \times 10^{-3}\, n_0$ to $5 \times 10^{-2}\, n_0$) to find the range of temperatures at which an appreciable K_α flux appeared at $\lambda = 7.9$-8.0 Å, but not at shorter wavelengths. This temperature range was found to be 30 eV to 45 eV.

Because the continuum is optically thick the radiation measured by the spectrometer originated in the outermost regions of the expanding target plasma. We therefore expect that both the protons and carbon ions contributed to the *heating* of the target plasma regions observed by the spectrometer. Earlier analysis [8], however, suggests that the satellite line *emission* is primarily a product of proton-impact ionizations, as opposed to multiple ionization events produced by carbon ions. In addition, the carbon particle flux was believed to be only $\lesssim 5\%$ of the proton flux in the experiment. This suggests that the plasma emitted K_α lines at a detectable level only while the proton current density was sufficiently high. Our calculations therefore suggest that temperatures of 30-45 eV were attained in the outer regions of the plasma while the proton current was relatively high. It remains possible that somewhat higher temperatures were reached either deeper inside the target plasma (regions which could not be probed because of opacity effects) or at later times after the proton current dropped (if additional heating from the carbon contaminants occurred).

Because of the experimental complexities (e.g., geometry, opacity effects, time-integrated spectral measurements), a more detailed comparison of synthetic spectra with

experiment has little added value at this time. We have demonstrated that computed K_α spectra, based on temperatures predicted from hydrodynamic simulations, are consistent with experimental measurements. In future experiments it is expected that time-resolved x-ray spectra will be obtained. Also, targets with thin tracer (diagnostic) layers or dopants can be implanted in targets to provide additional spatial resolution and mitigate opacity effects. These features will make it possible to more precisely determine the evolution of target plasma conditions from x-ray spectra.

VI. Summary

We have reported on our analysis of the first spectroscopic observations of K_α x-ray satellites from a moderately ionized target heated by an intense ion beam. A combination of atomic physics, CRE, line broadening, and hydrodynamic calculations were performed to investigate the physical processes that affect K_α emission spectra, and to deduce the plasma conditions attained in the PBFA-II experiment. A primary goal of this investigation is to lay the groundwork for diagnosing plasma conditions from inner-shell line radiation in future light ion beam experiments.

We have studied the relative contributions of ground state and excited state configurations to K_α emission spectra. Lines originating from excited state configurations were shown to make a very significant contribution. Calculations performed with these configurations included produced much better agreement with the PBFA-II spectrum. Transitions originating in excited states with $n \geq 3$ electrons result in relatively broad K_α lines which are blue-shifted relative to those of ground state configurations. In addition, excited state lines tend to be primarily Stark broadened and are sensitive to the electron density. The line widths of K_α transitions involving ground and low-lying excited states are dominated primarily by Auger rates below densities of $n_e \approx 2 \times 10^{23}$ cm^{-3}.

Opacity was found to have a significant effect on the K_α emission spectrum. For Al targets with thicknesses $\sim 10^2$ μm line optical depths were found to range as high as

10^4, while the continuum optical depth from L-shell photoabsorption was $\sim$ 5 –10. This indicates that the photons observed by the spectrometer were emitted from the outer "skin" of the Al plasma. It was also shown that resonant self-absorption can lead to a skewing of the K_α spectrum so that the intensities from lines of the dominant ionization stages are lower than those of less abundant higher ionization stages.

CRE analysis of the PBFA-II spectrum indicates that the relatively high intensities from the Al I–IV lines occurred early in the plasma evolution when temperatures were low ($T \lesssim 5$ eV). At these temperatures resonant self-absorption is negligible because of the lack of vacancies in the $2p$ shell. The intensities from the Al V–Al IX satellites were significantly reduced by self-absorption effects. Our analysis suggests that the maximum temperatures attained in the outer (observable) part of the target plasma were about 30 to 45 eV.

Hydrodynamic and PIC simulations of the PBFA-II experiment suggest that carbon ions in the beam played an important role in heating the outer skin of the target plasma. Although carbon-induced ionizations cannot at this point be absolutely ruled out as contributing to the observed K_α spectrum, both the lack of any evidence for multiple ionization events [8] and the low particle flux for the carbon contaminants suggest the spectrum is primarily produced as a result of proton-impact ionization.

K_α emission spectroscopy may offer important opportunities for diagnosing both plasma and beam properties in future light ion beam experiments. However, because of opacity effects it is important to reduce the size of the emitting region. This can be accomplished by placing thin tracer layers or dopants ($\sim 100 - 1000$ Å thick) into the primary target material. It is also of course crucial to obtain time-resolved spectra. These aspects will be pursued in future experiments.

Acknowledgements

We wish to thank the entire PBFA II experimental group for their efforts. This work has been supported in part by the U.S. Department of Energy under Contract No. DE-AC04-76DP00789, and by Kernforschungszentrum Karlsruhe (FRG) through Fusion Power Associates. Computing support was provided in part by the National Science Foundation through the San Diego Supercomputer Center.

References

1. A. Hauer, R. D. Cowan, B. Yaakobi, O. Barnouin, and R. Epstein, Phys. Rev. **A 34**, 411 (1986).

2. C. Chenais-Popovics, C. Fievet, J. P. Geindre, J. C. Gauthier, E. Luc-Koenig, J. F. Wyart, H. Pepin, and M. Chaker, Phys. Rev. **A 40**, 3194 (1989).

3. J. Bruneau, C. Chenais-Popovics, D. Desenne, J.-C. Gauthier, J.-P. Geindre, M. Klapisch, J.-P. Le Breton, M. Louis-Jacquet, D. Naccache, and J.-P. Perrine, Phys. Rev. Lett. **65**, 1435 (1990).

4. S. J. Davidson, J. M. Foster, C. C. Smith, K. A. Warburton, and S. J. Rose, Appl. Phys. Lett. **52**, 847 (1988).

5. D. M. O'Neil, C. L. S. Lewis, D. Neely, and S. J. Davidson, Phys. Rev. **A 44**, 2641 (1991).

6. J. Abdallah, Jr., R. E. H. Clark, and J. M. Peek, Phys. Rev. **A 44**, 4072 (1991).

7. T. S. Perry, S. J. Davidson, F. J. D. Serduke, D. R. Bach, C. C. Smith, J. M. Foster, R. J. Doyas, R. A. Ward, C. A. Iglesias, F. J. Rogers, J. Abdallah, Jr., R. E. Stewart, J. D. Kilkenny, and R. W. Lee, Phys. Rev. Lett. **67**, 3784 (1991).

8. J. Bailey, A. L. Carlson, G. Chandler, M. S. Derzon, R. J. Dukart, B. A. Hammel, D. J. Johnson, T. R. Lockner, J. Maenchen, E. J. McGuire, T. A. Mehlhorn, W. E. Nelson, L. E. Ruggles, W. A. Stygar, and D. F. Wenger, Lasers and Particle Beams **8**, 555 (1990).

9. E. Nardi, and Z. Zinamon, J. Appl. Phys. **52**, 7075 (1981).

10. J. P. Van Devender and D. L. Cook, Science **232**, 831 (1986).

11. D. L. Cook et al., Plasma Phys. and Controlled Fusion **28**, 1921 (1986).

12. D. J. Johnson et al., *Proc. of the 7th IEEE Pulsed Power Conf.*, Monterey, CA, 944 (1989).

13. R. J. Leeper et al., *Proc. of Workshop on Diag. for Cont. Fusion Exp.* (ed. by P. E. Stott, D. K. Akulina, G. Gorini, and E. Sindoni, Societa Italiana di Fisica Press, Bologna, Italy, 1991), p. 1051.

14. B. L. Henke, H. T. Yamada, and T. J. Tanaka, Rev. Sci. Instrum. **54**, 1311 (1983).

15. B. A. Hammel and L. E. Ruggles, Rev. Sci. Instrum. **60**, 2861 (1989).

16. B. A. Hammel, D. W. Phillion, and L. E. Ruggles, Rev. Sci. Instrum. **61**, 1920 (1990).

17. X-ray Optics Inc., Jacksonville, Fl.

18. B. L. Henke et al., J. Opt. Soc. Am. B **3**, 1540 (1986).

19. P. D. Rockett et al., Appl. Opt. **24**, 2536 (1985).

20. L. L. House, Astrophys. J. Suppl. **18**, 21 (1969).

21. B. L. Henke, private communication.

22. J. J. MacFarlane and P. Wang, Laser and Particle Beams, in press (1992). More details on CRE model are provided in University of Wisconsin Fusion Technology Institute Reports UWFDM-822 (1990), UWFDM-847 (1991), and UWFDM-873 (1992).

23. J. P. Apruzese, J. David, D. Duston, and K. G. Whitney, J.Q.S.R.T. **23**, 479 (1980).

24. J. J. MacFarlane, Astron. Astrophys. **264**, 153 (1992).

25. H. Griem, Phys. Rev. **165**, 258 (1968).

26. D. Duston, R. W. Clark, J. Davis, and J. P. Apruzese, Phys. Rev. A **27**, 1441 (1983).

27. C. F. Fischer, Comput. Phys. Commun. **14**, 145 (1978).

28. R. Glass and A. Hibbert, Comput. Phys. Commun. **16**, 19 (1978).

29. P. Wang, J. J. MacFarlane, and G. A. Moses, submitted to Phys. Rev. A (1992).

30. A. Burgess and M. C. Chidichchimo, Mon. Not. R. Astr. Soc. **203**, 1269 (1983).

31. M. J. Seaton, in *Atomic and Molecular Processes*, p. 374, edited by D. R. Bates (Academic Press, New York, 1962).

32. I. I. Sobelman, L. A. Vainshtein, and E. A. Yukov, *Excitation of Atoms and Broadening of Spectral Lines* (Springer-Verlag, New York, 1981).

33. D. E. Post, R. V. Jensen, C. B. Tarter, W. H. Grasberger, and W. A. Lokke, Atomic Data Nucl. Data Tables **20**, 397 (1977).

34. E. Merzbacher and H. W. Lewis, in *Handbuch der Physik, Vol. 34*, edited by S. Flugge (Springer-Verlag, Berlin, 1958).

35. C. H. Rutledge and R. L. Watson, Atomic Data Nucl. Data Tables **12**, 195 (1973).

36. J. M. Kahn, D. L. Potter, and R. D. Worley, Phys. Rev. A **13**, 1735 (1965)

37. T. A. Mehlhorn, W. E. Nelson,, J. E. Maenchen, W. A. Stygar, C. L. Ruiz, T. R. Lockner, and D. J. Johnson, Rev. Sci. Instrum. **59**, 1709 (1988).

38. S. L. Thompson, Sandia National Laboratories Report No. SC-RR-710714, Albuquerque, NM (1972).

39. T. A. Mehlhorn, J. Appl. Phys. **52**, 6522 (1981).

40. L. A. Woltz and C. F. Hooper, Jr., Phys. Rev. A **38**, 4766 (1988).

41. R. C. Mancini, D. P. Kilcrease, L. A. Woltz and C. F. Hooper, Jr., Comp. Phys. Comm. **63**, 314 (1991).

42. R. D. Cowan, *The Theory of Atomic Structure and Spectra*, University of California Press (Berkeley, 1981).

43. L. A. Woltz, V. L. Jacobs, C. F. Hooper, Jr. and R. C. Mancini, Phys. Rev. A **44**, 1281 (1991).

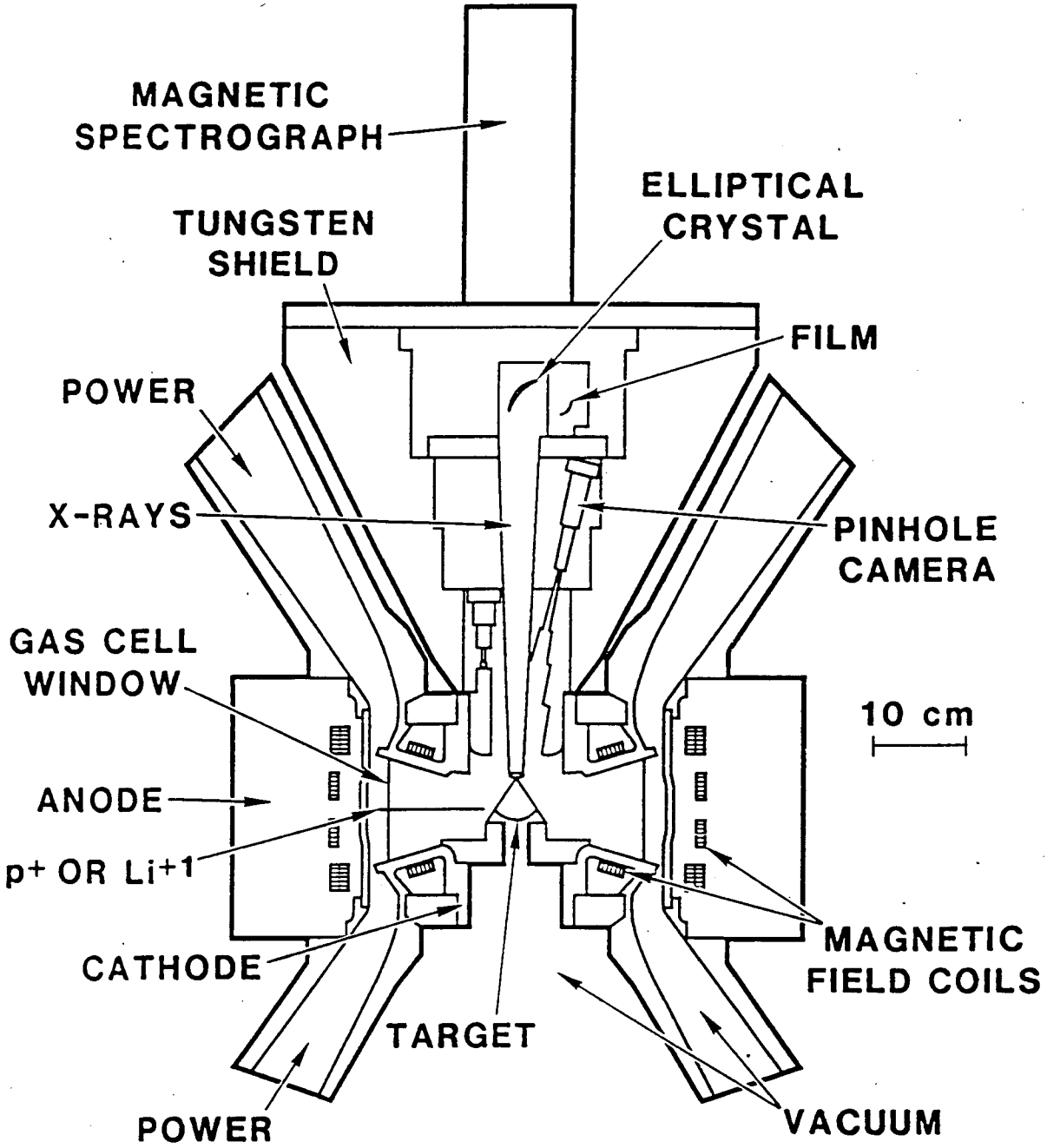

Figure 1. Schematic of the PBFA-II diode region. The diagnostics are packaged inside a tungsten shield to protect them from the hard x-ray background.

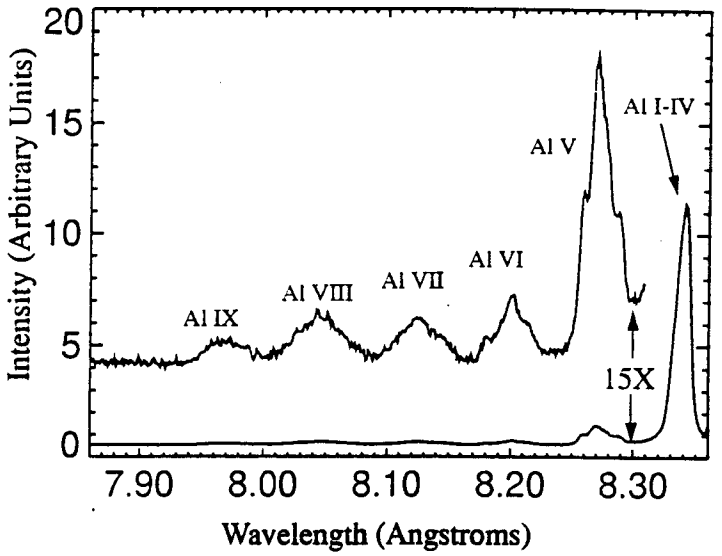

Figure 2. K_α spectrum from aluminum target irradiated by the PBFA-II ion beam. The top spectrum is the same as the bottom spectrum, but with the amplitude multiplied by a factor of 15. The labels refer to the ionization stages prior to beam-induced inner-shell ionization.

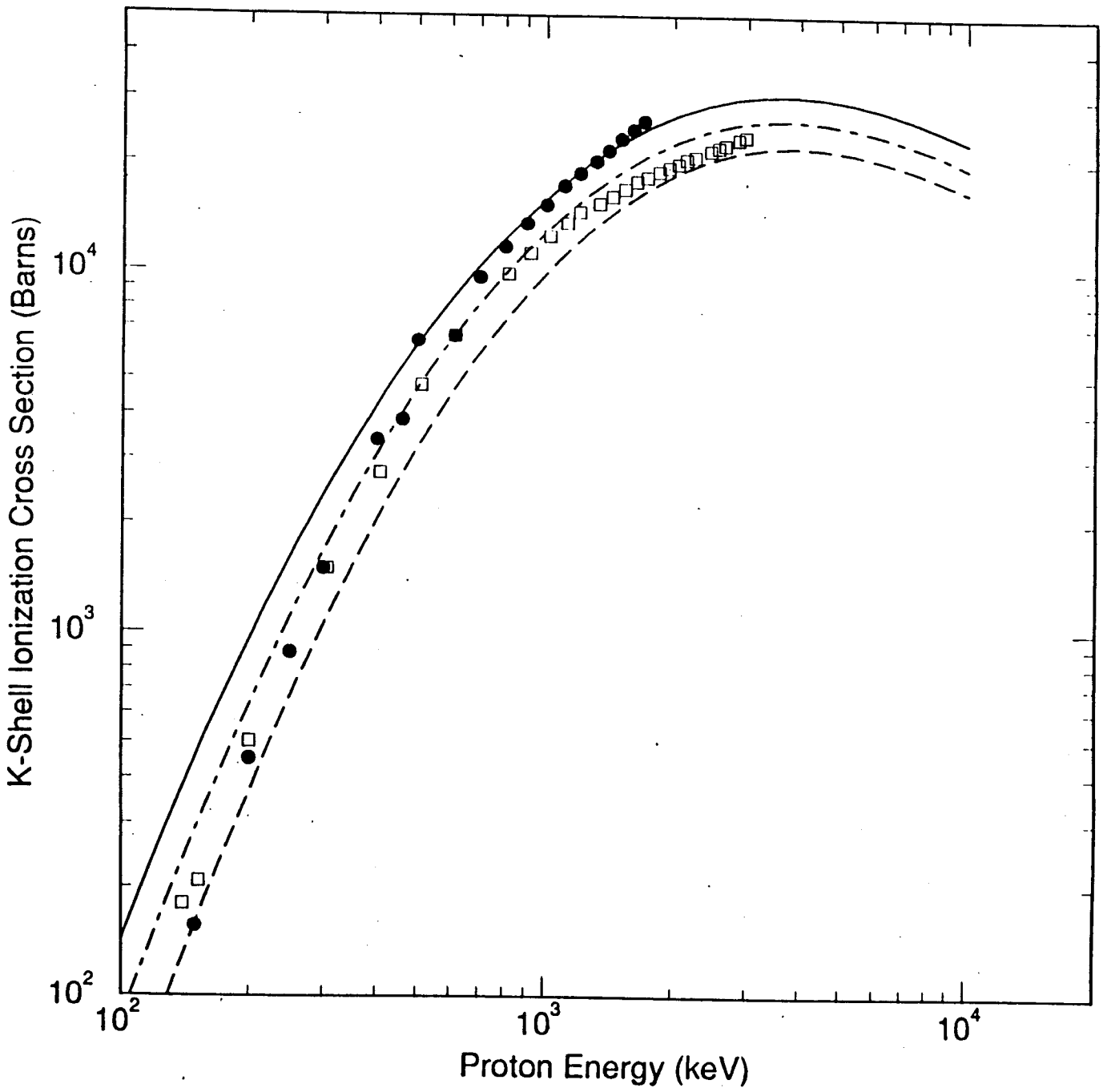

Figure 3. K-shell proton impact ionization cross sections calculated for Al I (solid curve), Al VI (dash-dotted curve), and Al IX (dashed curve). Also shown are experimental data for Al I from Ref. 35 (□) and Ref. 36 (•).

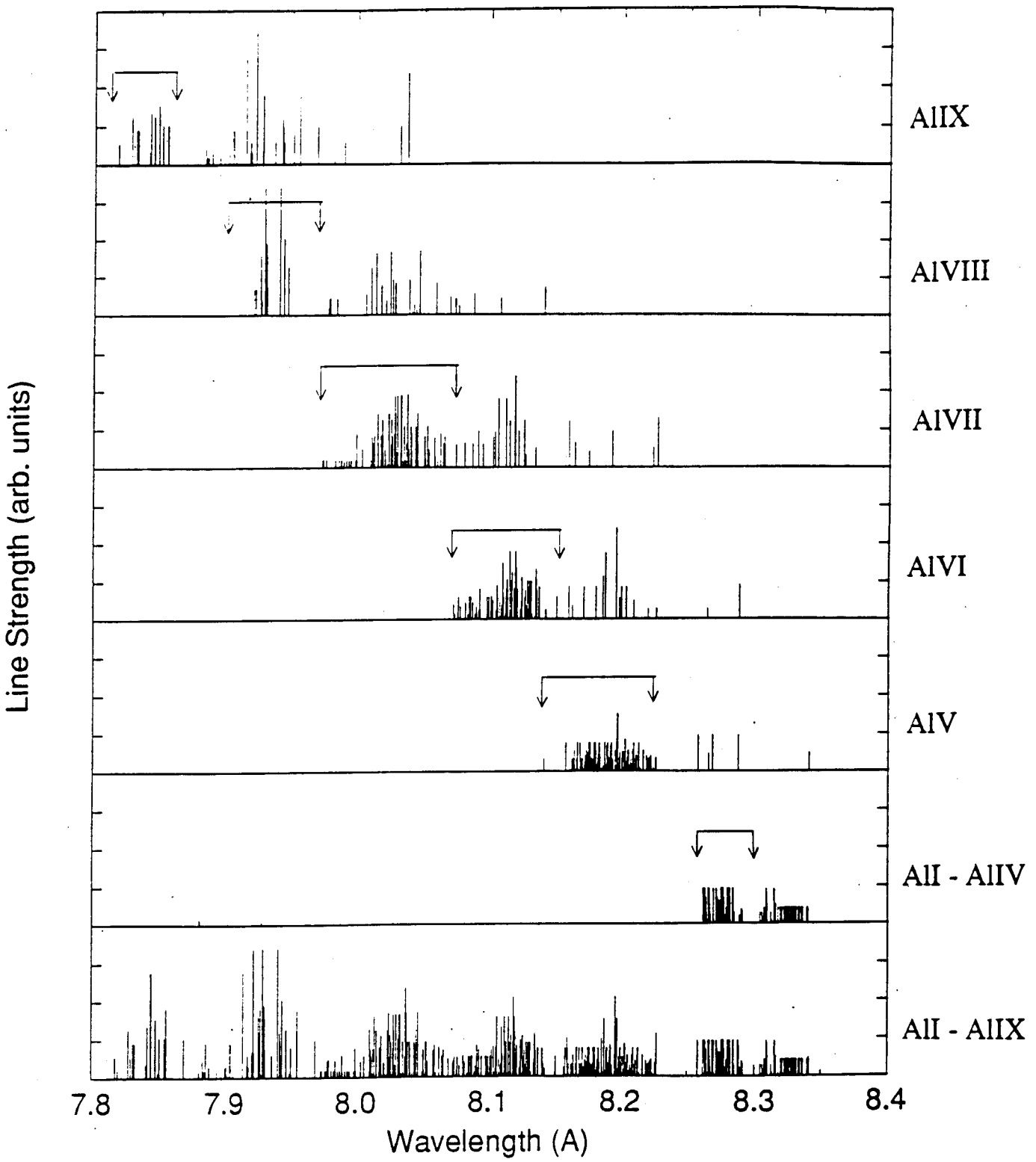

Figure 4. Stick spectrum showing K_α line wavelengths for Al I–IX. The regions bracketted by arrows represent wavelength regions dominated by excited state configurations (with $n = 3$ valence electrons).

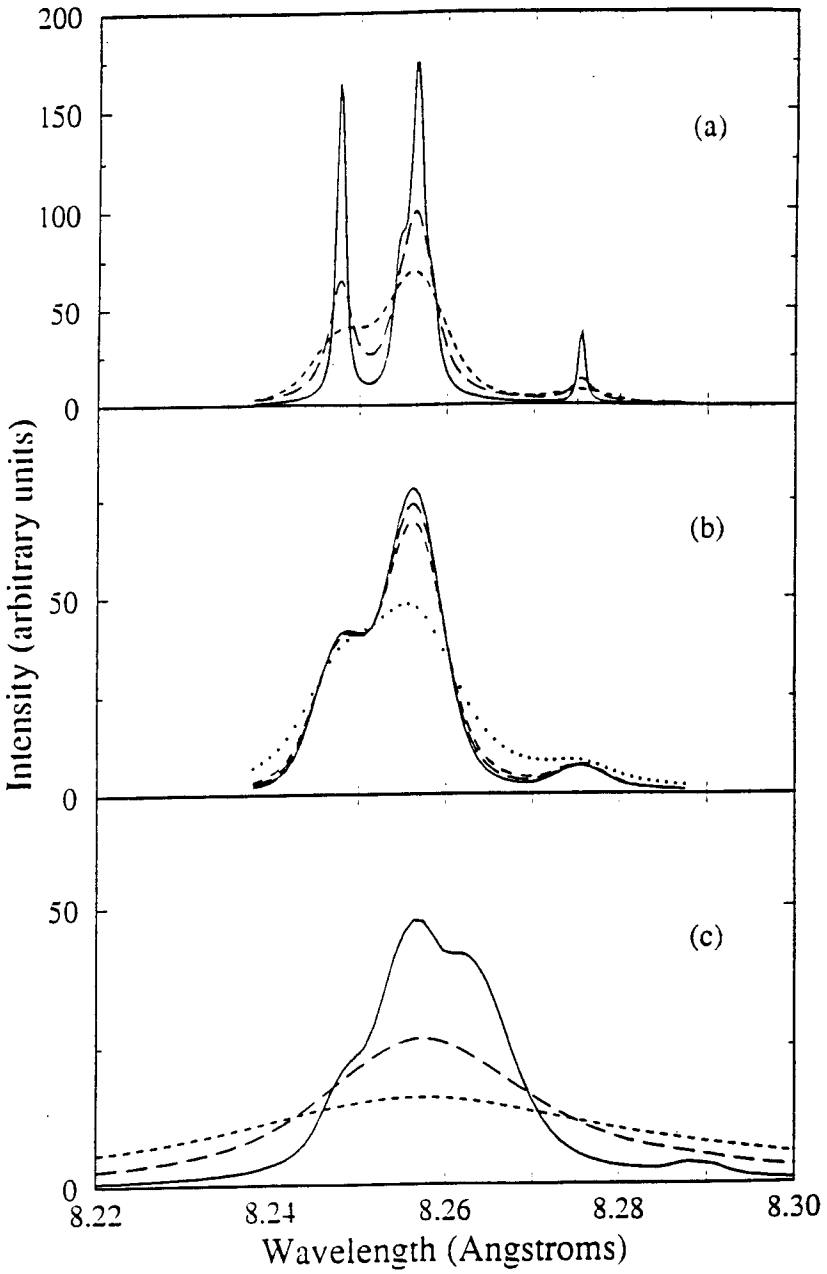

Figure 5. (a) Line profiles for K_α transitions in O-like Al at $T = 20$ eV and $n_e = 10^{23}$ cm^{-3}: (solid) Stark plus Doppler broadening; (long-dashed) same as solid but also includes Auger and radiative decay widths; (short-dashed) same as long-dashed but with instrumental broadening. (b) Stark broadened line profiles at $T = 20$ eV including Auger and radiative decay widths, and instrumental broadening for $n_e = 1 \times 10^{22}$ cm^{-3} (solid), 5×10^{22} cm^{-3} (long-dashed), 1×10^{23} cm^{-3} (short-dashed), and 5×10^{23} cm^{-3} (dotted). (c) Stark broadened profiles in F-like Al with one spectator electron in $n = 3$ shell at $T = 20$ eV and $n_e = 5 \times 10^{21}$ cm^{-3} (solid), 2×10^{22} cm^{-3} (long-dashed), and 5×10^{22} cm^{-3} (short-dashed).

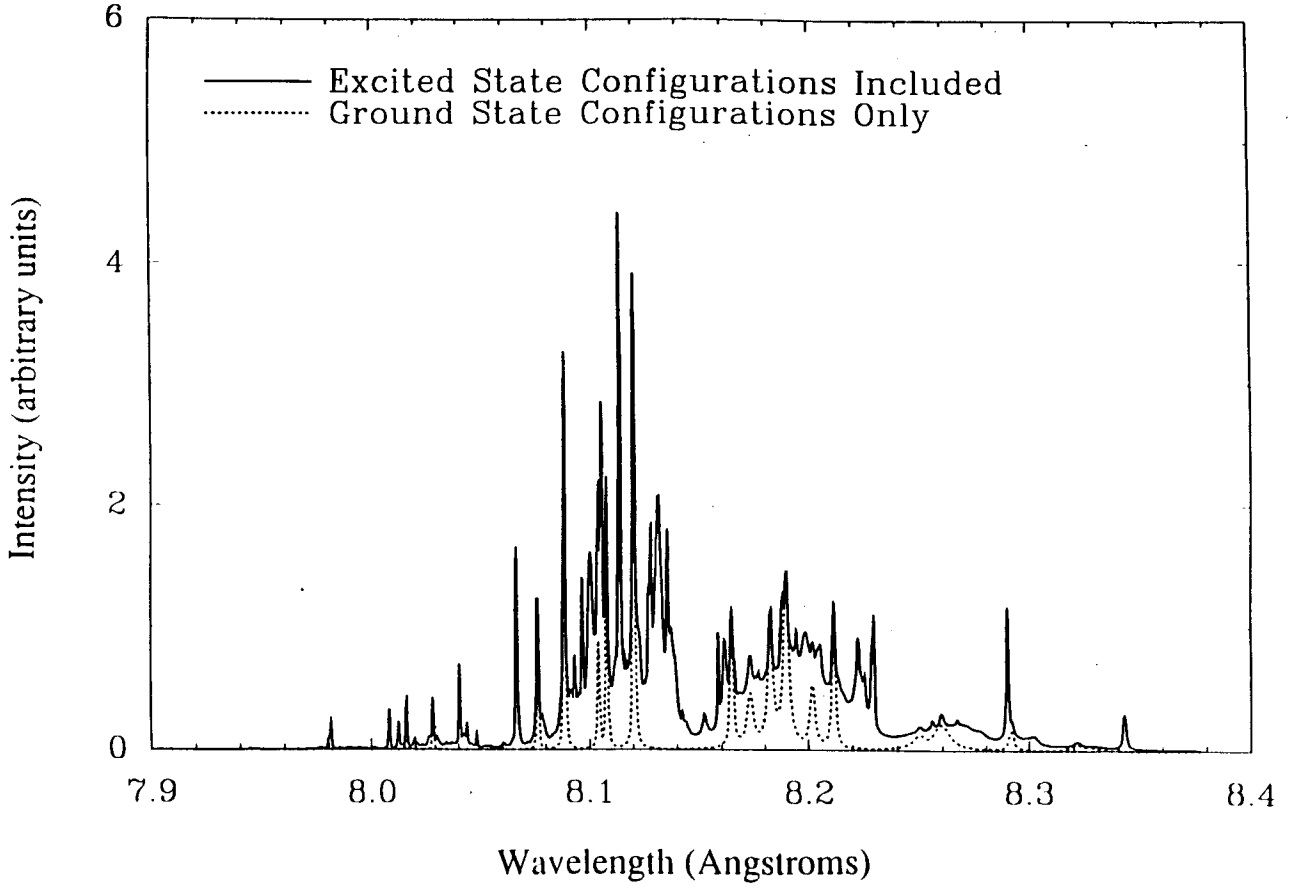

Figure 6. Calculated K_α emission spectrum for an Al plasma at $T = 30$ eV, $n = 10^{-1}\, n_0$, and $L = 0.1\,\mu$m; (dotted) includes ground state configurations only; (solid) also includes excited state configurations up to $n = 3$.

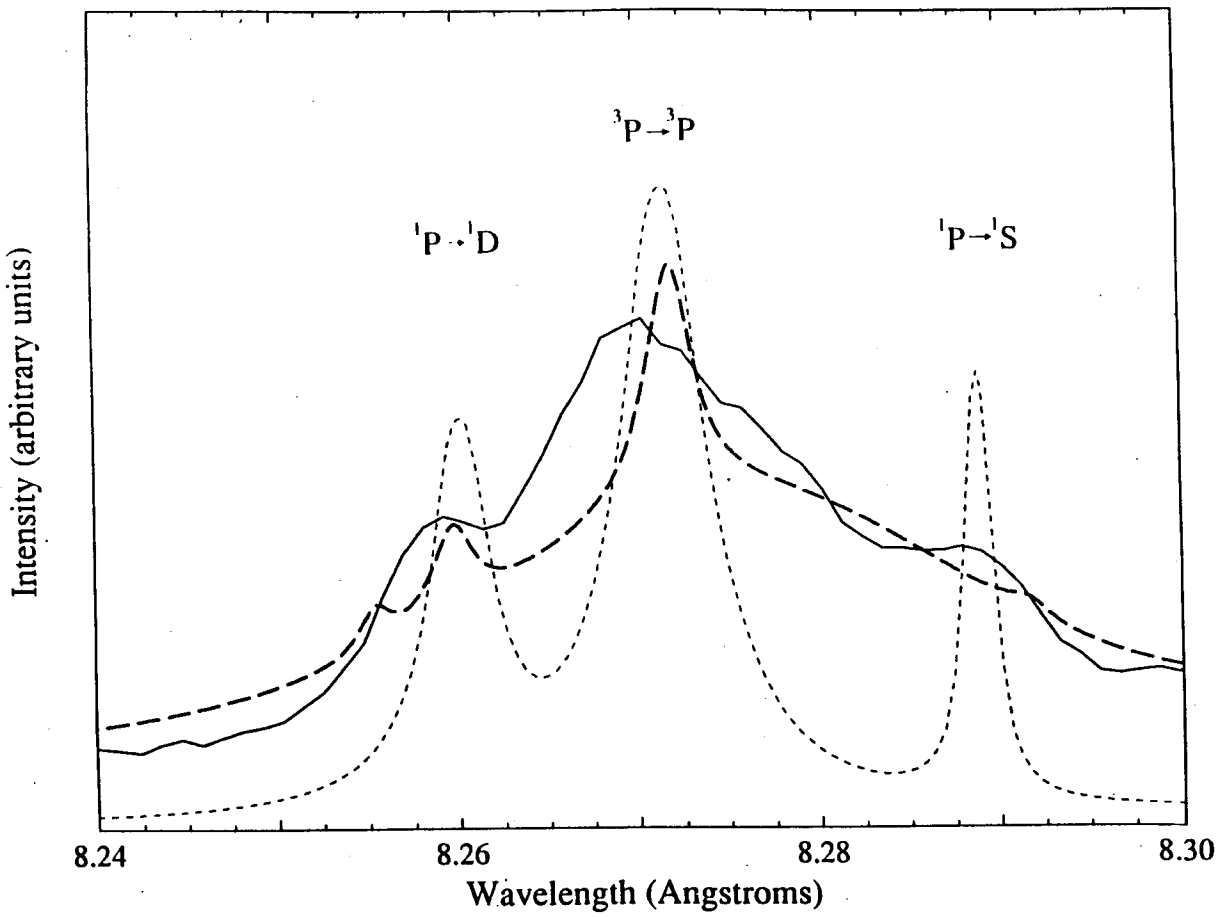

Figure 7. Comparison of calculated and experimental K_α spectra in region dominated by ground state configurations of O-like Al (prominent features are labelled) and excited states of F-like Al: (solid) experimental spectrum; (long-dashed) calculation including $n = 3$ excited state configurations; (short-dashed) calculation with ground state configurations only.

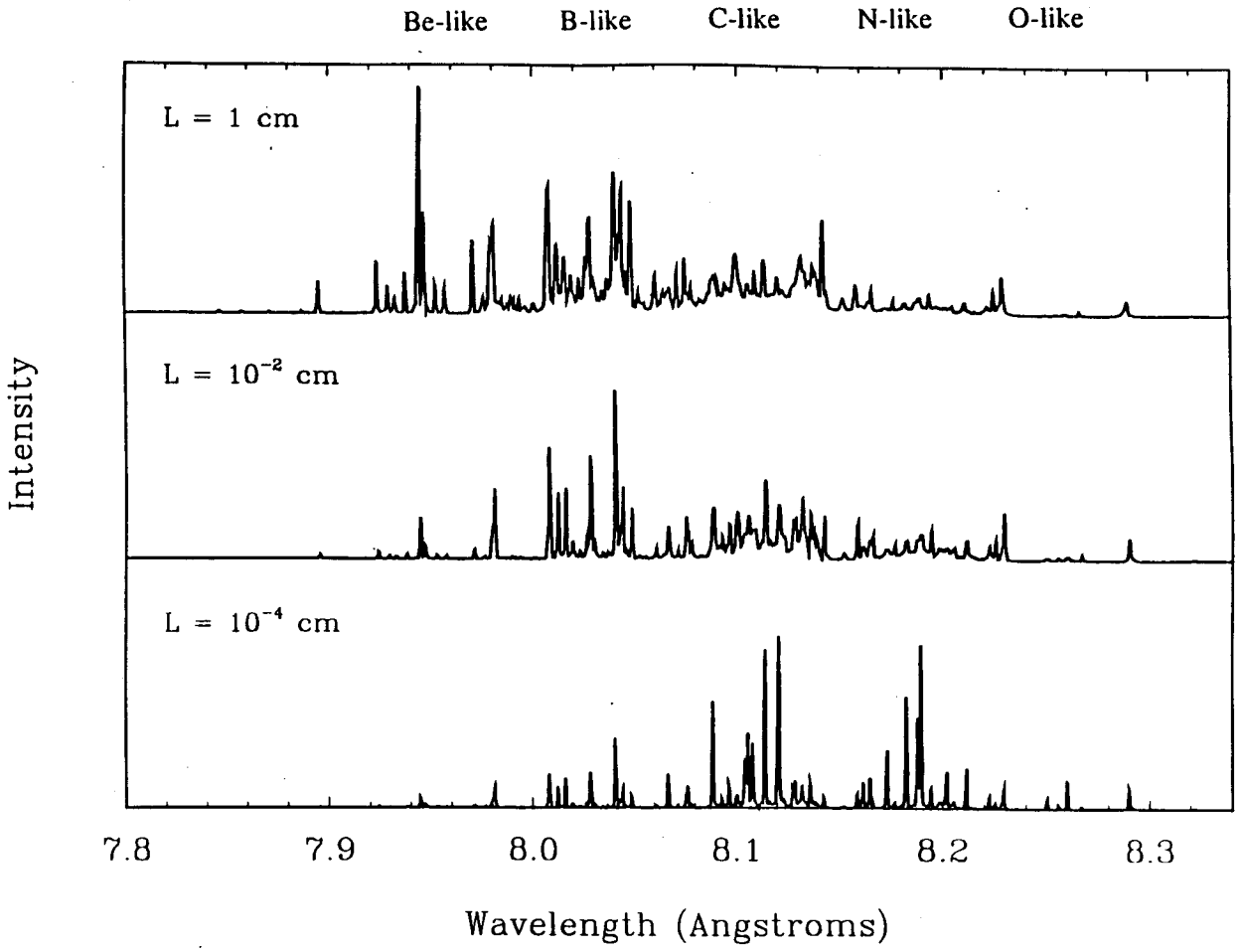

Figure 8. Calculated K_α spectra for Al plasmas at $T = 35$ eV and $n = 10^{-2}\, n_0$. Widths of the plane-parallel plasmas range from $L = 1\,\mu$m (bottom) to 1 cm (top). Opacity effects tend to skew the spectrum toward higher ionization stages. $L = 10^{-2}$ cm and $L = 10^{-4}$ cm intensities are multiplied by 1.5 and 30, respectively. The labels refer to the ionization stage after beam-induced inner-shell ionization.

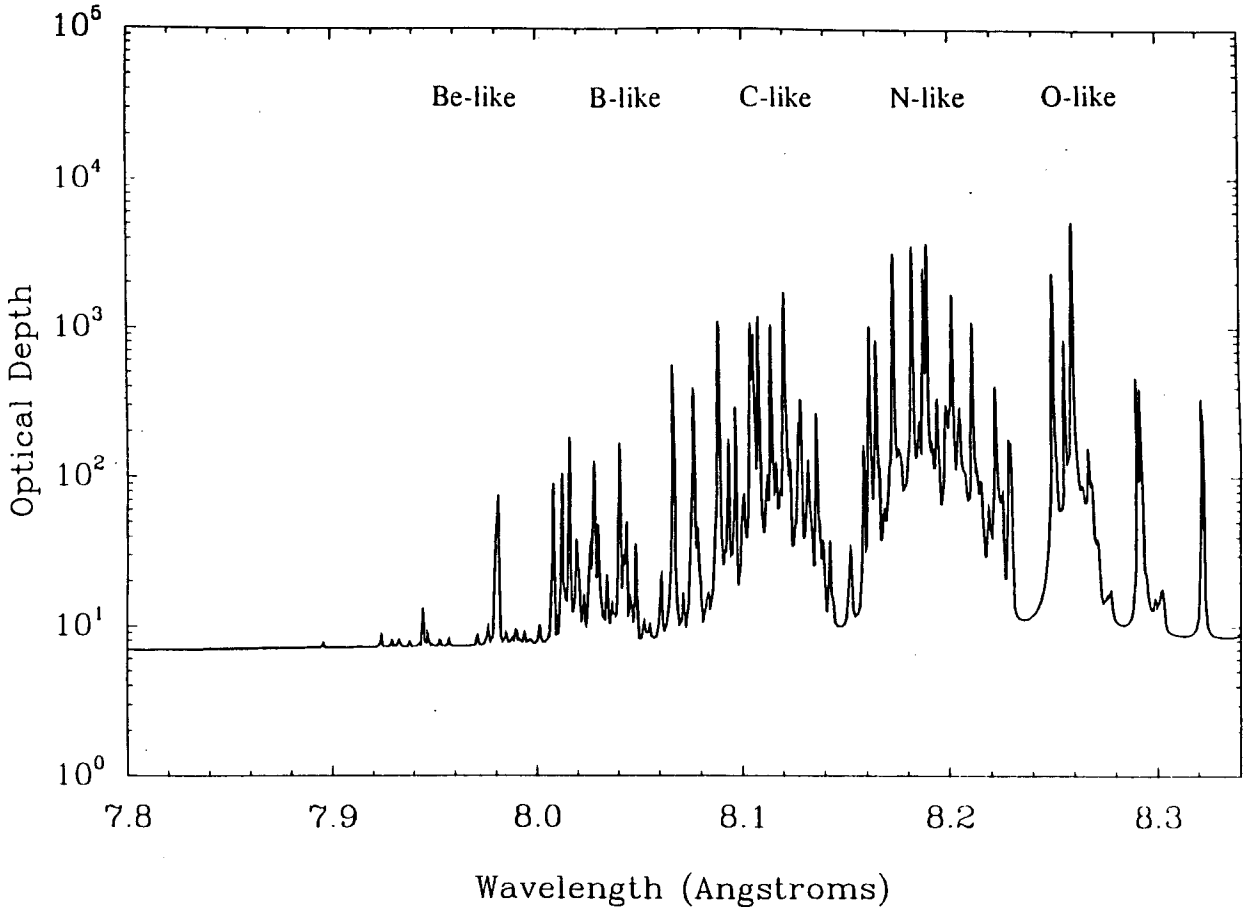

Figure 9. Wavelength dependent optical depth for the $L = 1$ cm case in Figure 8.

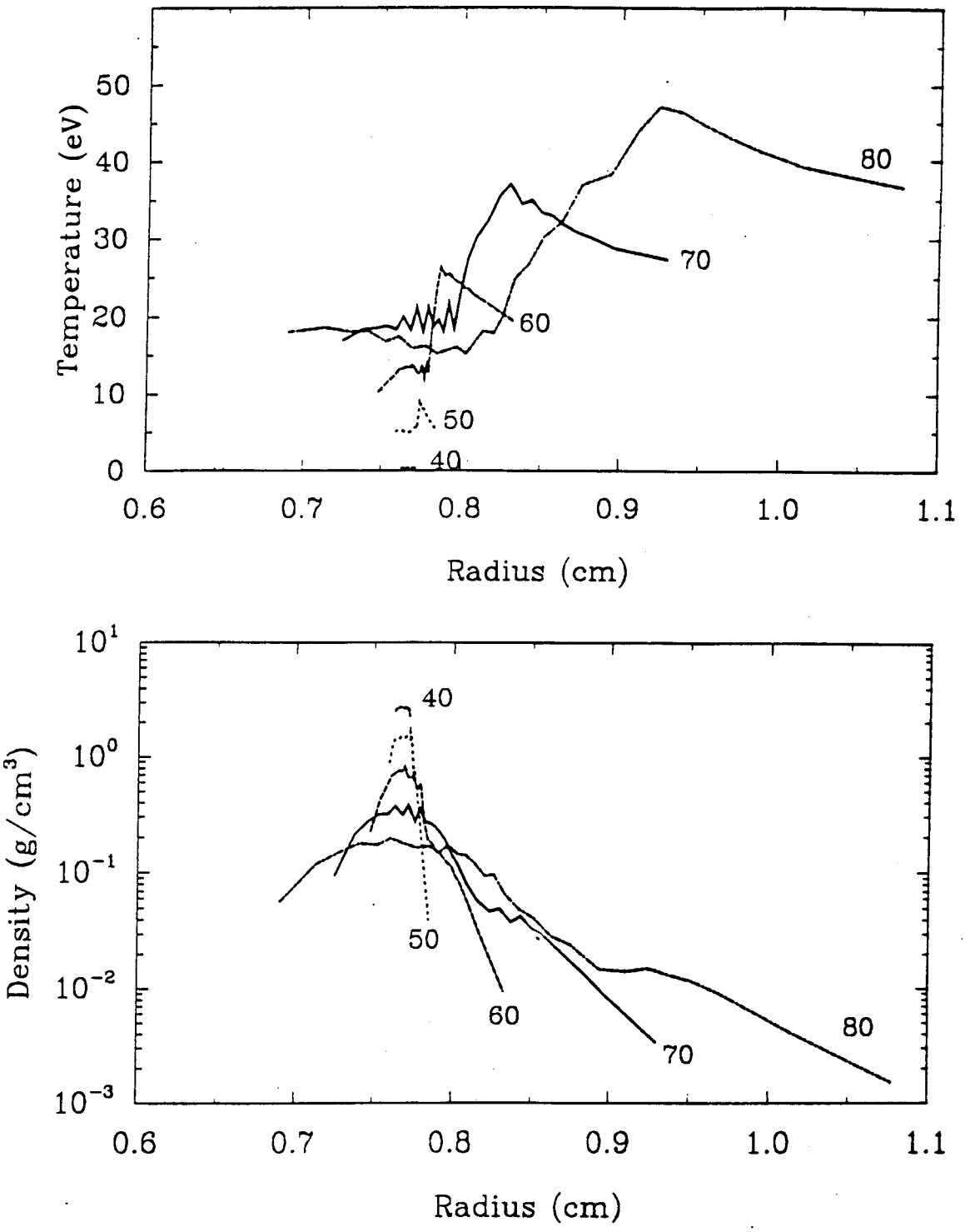

Figure 10. Time evolution of temperature (top) and density (bottom) distributions predicted from radiation-hydrodynamic simulations. The ion beam irradiates the target from the right in this figure. The curves are labelled by the simulation time in ns.

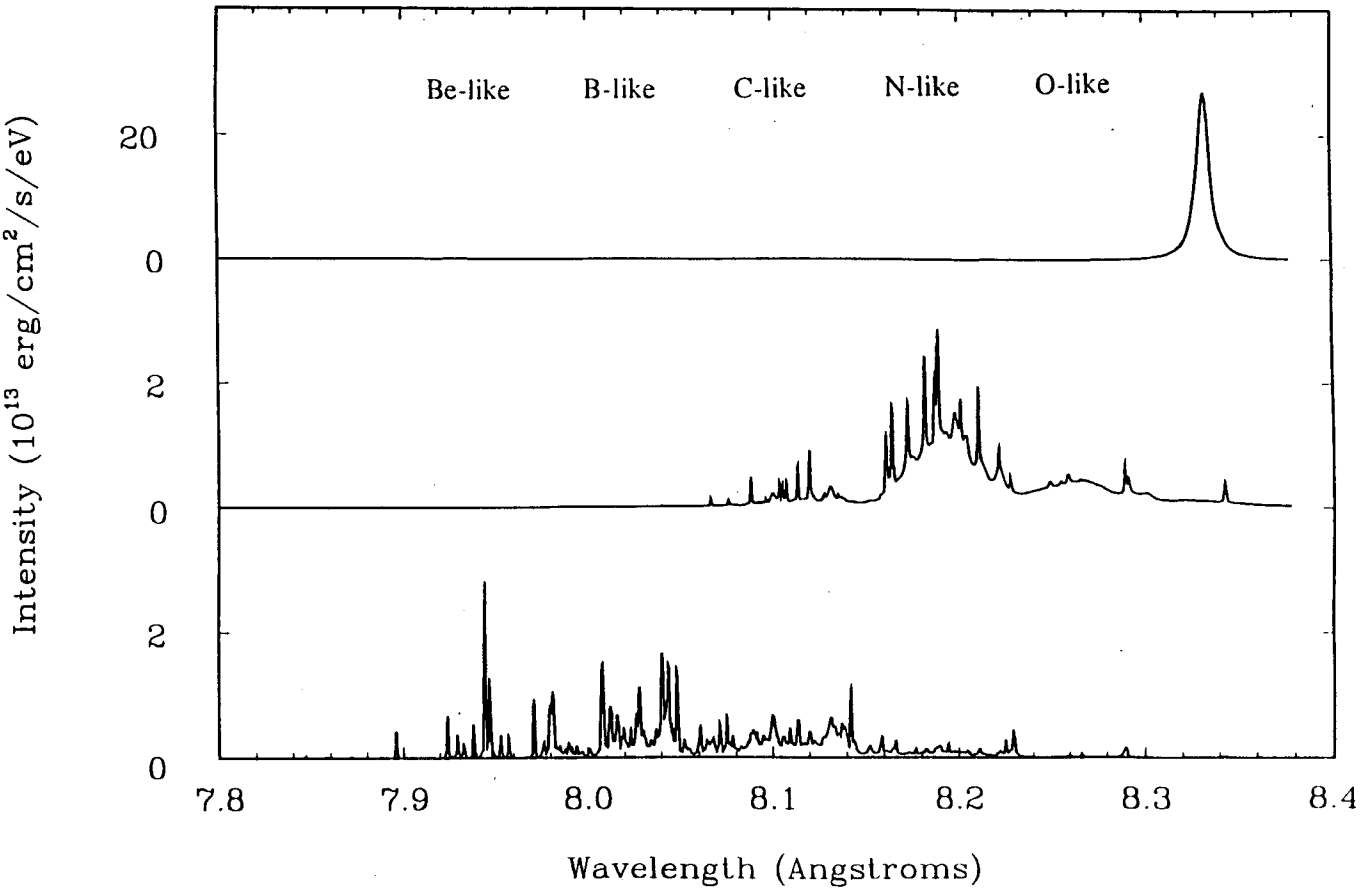

Figure 11. Calculated K_α spectra for Al plasmas with the following conditions: (top) $T = 2.5$ eV, $n = 0.2\,n_0$, $J = 0.15$ MA/cm^2; (middle) $T = 25$ eV, $n = 0.05\,n_0$, $J = 0.3$ MA/cm^2; (bottom) $T = 35$ eV, $n = 0.01\,n_0$, $J = 0.3$ MA/cm^2. Note the $T = 2.5$ eV intensities have been reduced by a factor of 10.

Appendix B

Relativistic Configuration Interaction Calculations for K_α Satellite Properties of Aluminum Ions

P. Wang, J.J. MacFarlane, G.A. Moses

(Submitted to Physical Review)

Abstract

Configuration interaction calculations with Breit-Pauli relativistic corrections have been carried out for aluminum ions to study the properties of Kα satellite spectra produced by proton beam heated aluminum plasmas. Detailed calculations have been performed both for transitions involving the ground configuration states and for transitions involving low excited configuration states. Calculated wavelengths for the Kα transitions are compared with a spectrum obtained during a PBFA-II proton beam/plasma interaction experiment. Our calculations show that the Kα satellite lines can be classified into two distinct groups: one involving transitions of type $1s^1 2s^m 2p^n \rightarrow 1s^2 2s^m 2p^{n-1}$, the other $1s^1 2s^m 2p^{n-1} 3l \rightarrow 1s^2 2s^m 2p^{n-2} 3l$. The former gives the 'characteristic' satellite line position of an ion, while the latter overlaps with lines of the next higher ionization stage. The 'overlap' group can significantly affect the observed line shape of the Kα spectra. Examination of correlation effects and relativistic corrections on the Kα transition energies indicates that both corrections are important.

1. Introduction

Kα lines result from transitions between an atomic state having at least one vacancy in the $1s$ shell and a state in which an electron from the $2p$ subshell fills this vacancy. The Kα lines corresponding to transitions from initial states having one hole in the K shell and n holes in the L shell are the satellite Kα lines. These satellite Kα lines are blue-shifted with respect to the principal Kα lines because of the reduced screening of the nucleus which results when there are fewer spectator electrons. In the case of light elements (atomic number Z less than 20), the energy shift (the distance between the consecutive satellites) caused by introducing an additional hole in the L shell is readily observable in present day laboratory plasma experiments ($\Delta\lambda/\lambda \sim 10^{-2}$). It has been suggested that this characteristic of Kα satellite spectra can be used as a temperature diagnostic for plasmas heated by particle beams in inertial fusion experiments [1]. Light-ion impact ionization of K-shell electrons populates autoionizing states, which then produce fluorescence Kα line emission. Since the Kα satellite lines from Ne-like to He-like ions exhibit detectable shifts to shorter wavelengths, Kα satellite line spectra can provide a measure of the ionization distribution in a plasma, and from that, constraints on plasma conditions.

The first spectroscopic observation of Kα x-ray satellite lines in an intense proton beam experiment was recently made during a Particle Beam Fusion Accelerator II (PBFA-II) experiment at Sandia National Laboratories [2]. In this experiment an aluminum target was irradiated with a $4 - 6$ MeV, $1 - 2$ TW/cm^2 proton beam. An elliptic crystal spectrograph was used to obtain a time-integrated spectrum (see Figure 1). Two important features should be noted in this experimental Kα satellite spectrum. First, there is a high degree of structure which is likely caused by term-dependent Kα transitions. In addition, the satellite line shapes are very broad. It has been suggested [3] that this broad line shape may come from the overlap of the Kα satellite lines from the

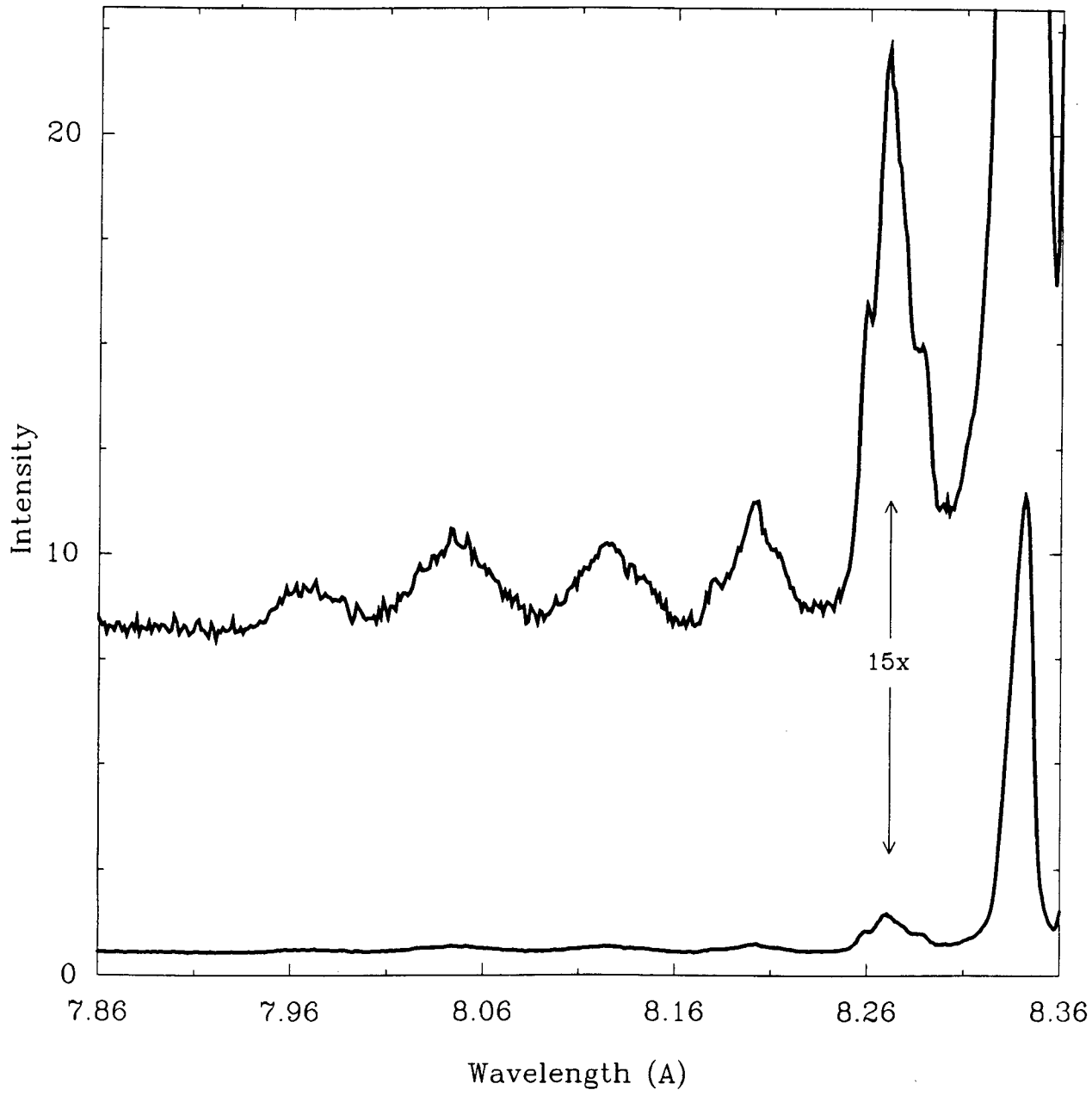

Figure 1. Kα spectrum from an aluminum target irradiated by the PBFA-II ion beam. The top spectrum is the same as the bottom spectrum, but with the amplitude multiplied by a factor of 15.

transitions involving the excited configuration states containing M-shell electrons because of the significant Stark broadening for these lines.

Detailed calculations of the wavelengths and transition probabilities of the Kα lines for aluminum ions has been carried out by Chenais-Popovics et al. [4] using a relativistic parametric potential method [5]. However, we found that some disagreements exist between their results and the PBFA-II experimental spectrum. This may be because the correlation effects were neglected in their calculation. To accurately compute wavelengths for transitions between the K- and L- shells of moderate-Z ions, both relativistic and correlation effects must be included in determining the transition energies. To date, the number of such relativistic configuration interaction (CI) calculations for the Kα transitions of aluminum ions is very small. Also, very few studies have been done for aluminum Kα satellite line structure with the inclusion of the transition involving the excited configuration states containing M- and higher shell electrons.

In the present study, configuration interaction calculations with Breit-Pauli relativistic corrections have been carried out for the Kα transitions of aluminum ions, including both the transitions involving the ground configuration states and those involving the low excited configuration states. The purpose of the calculations is to provide accurate transition energies and oscillator strengths for analyzing aluminum Kα spectra in light ion fusion experiments. In our calculations, we first performed multiconfiguration Hartree-Fock (MCHF) calculations [6] to determine a basis for the representation of the states of interest. Then a configuration-interaction calculation within the Breit-Pauli approximation was performed. In this way, both relativistic and correlation effects can be properly accounted for.

2. Calculations

All our calculations have been performed using the CI code CIBASE which is based on the modification of Fraga's configuration interaction program RIAS [7]. A brief overview of the calculation method used is given in this section.

The CI wavefunctions for each atomic state are represented by expansions of the form

$$\Psi(J, M_J) = \sum_i^N a_i \Phi(\alpha_i L_i S_i, J M_J) \tag{1}$$

where N is in principle infinite, but for all practical calculations is finite; $\{\Phi_i\}$ is a set of 'configuration wavefunctions' - each describing a configuration and is constructed from one-electron functions with $\{\alpha_i\}$ defining the coupling scheme of angular momenta of the electrons. The Hamiltonian matrix, with typical element $< \Phi_i|H|\Phi_j >$ can be diagonalized to give eigenvalues $E_1 < E_2 < \cdots < E_N$. Then from the Hylleraas-Undheim-MacDonald theorem [8], we have

$$E_k \geq E_k^{exact}. \tag{2}$$

The wavefunction associated with a particular eigenvalue (eigen-energy E_k) is then given by Eq. (1) with the $\{a_i\}$ taken to be the corresponding eigenvector components:

$$\sum_j^N (H_{ij} - E_k \delta_{ij}) a_j = \ 0, \quad j = 1, 2, \ldots, N. \tag{3}$$

In the intermediate-coupling scheme the sum over i in the expansion includes N configurations in which the orbital L_i and spin S_i angular momenta couple to give the total angular momenta

$$J = L_i + S_i. \tag{4}$$

Each one-electron function is the product of a radial function, a spherical harmonic and a spin function. The configuration functions $\{\Phi_i\}$, and hence the eigenvalues $\{E_k\}$, depend on the choice of radial functions $\{P(nl|r)\}$. The inequalities of Eq. (2) allow any of the

eigenvalues to be used as the functional to be minimized with respect to variations in the radial functions. In this study, the multiconfiguration Hartree-Fock were performed using Froese Fischer's program MCHF77 [6]. The calcultions were carried out for the lowest state of each principal configuration under consideration, including configurations that involved all the orbitals to be used in the CI calculations. The radial functions obtained in such a way are ensured to be orthonormal automatically. It should be noted that we used the Breit-Pauli Hamiltonian only for determining the mixing coefficients a_i appearing in CI expansions and not for the optimization of the radial functions.

The Hamiltionian operator considered in this work may be written as

$$H = H_{el} + H_{SM} + H_{rel} \tag{5}$$

where H_{el} denotes the electronic Hamiltonian (consisting of the electron kinetic, nuclear attraction, and electrostatic repulsion energy terms), H_{SM} denotes the operator for specific mass effect, and

$$H_{rel} = H_{LS} + H_{fs} \tag{6}$$

includes the usual relativistic corrections: H_{LS} consists of the so-called LS-non-splitting terms (mass variation, Darwin corrections, and electron spin-spin contract and orbit-orbit interactions), H_{fs} includes the fine-structure (electron spin-own orbit, spin-other orbit and spin-spin dipole) couplings. Detailed expressions for each of these operators have been given in the literature [9,10].

Once wavefunctions in the form of Eq. (1) have been determined, they are used to obtain transition oscillator strengths for transitions between initial and final states Ψ^i and Ψ^j with energies E^i and E^j:

$$g_i f(i \rightarrow j) = \frac{2\Delta E}{3} | < \Psi^i | \sum_p \mathbf{r}_p | \Psi^j > |^2 \tag{7}$$

where $\Delta E = |E^i - E^j|$, $g_i = (2L_i + 1)(2S_i + 1)$ for L-S coupling and $g_i = 2J_i + 1$ for intermediate coupling.

3. Results And Discussion

3.1. Effects of correlation and relativistic corrections on the Kα transition energies

The salient feature of Kα transitions is the inclusion of K- and L-shell electrons. It is therefore important to examine the effects of both correlation and relativistic corrections on the Kα transition energies.

To study this problem, we have used four different approaches to calculate the transition energies for the term-dependent transitions of $1s^12s^22p^5 \rightarrow 1s^22s^22p^4$ and $1s^12s^12p^6 \rightarrow 1s^22s^12p^5$ in AlV (throughout the rest of this paper, the designation for ions is for the ionization stage before the K-shell ionization by proton impact): (1) nonrelativistic single-configuration Hartree-Fock (HF), (2) single-configuration Hartree-Fock with Breit-Pauli relativistic corrections (HF+BP), (3) nonrelativistic multiconfiguration Hartree-Fock (MCHF) and (4) configuration interaction with Breit-Pauli relativistic corrections (CI +BP). The calculated results are collected in Table I. Also given in Table I are the calculated values of Chenais-Popovics et al. The corresponding configurations used in the CI expansions are listed in Table II.

Two things should be noted in comparing the data in Table I. First, our HF+BP results are very close to those of Chenais-Popovics et al. This is because both calculations neglected the correlation effect but included the relativistic corrections. Second, if we take the results of CI+BP as a reference, it is easy to find that the wavelengths obtained from the MCHF calculation have a redshift while the wavelengths obtained from HF+BP calculation have a blueshift. The results of the HF calculation are closer to the results of the CI+BP than the others. In general, the relativistic effects are the strongest for inner-shell electrons, while the correlation effects are the strongest for outer atomic shells. Hence, it can be expected that the correlation corrections for the upper state ($1s^12s^22p^5$ and $1s^12s^12p^6$) energies are stronger than those for the lower state ($1s^22s^22p^4$

TABLE I

Calculated Wavelengths for the Term-Dependent Transitions of Al V

Transitions	HF	HF + BP	MCHF	CI + BP	Chenais-Popovics[4]
$1s^1 2s^2 2p^5 \rightarrow 1s^2 2s^2 2p^4$					
$^1P^o - {}^1S$	8.293	8.281	8.295	8.287	—
$^1P^o - {}^1D$	8.261	8.248	8.264	8.258	8.249
$^3P^o - {}^3P$	8.273	8.257	8.278	8.269	8.259
$1s^1 2s^1 2p^6 \rightarrow 1s^2 2s^1 2p^5$					
$^3S - {}^3P^o$	8.270	8.265	8.272	8.267	8.264
$^1S - {}^1P^o$	8.357	8.343	8.359	8.349	–

TABLE II

Configurations Used in the CI Expansions for Al V Calculations

$^1P^o$, $^3P^o$	^1S	^1D, ^3P
$1s^1 2s^2 2p^5$	$1s^2 2s^2 2p^4$	$1s^2 2s^2 2p^4$
$1s^1 2p^5 3s^2$	$1s^2 2p^6$	$1s^2 2p^4 3s^2$
$1s^1 2s^2 2p^3 3s^2$	$1s^2 2p^4 3s^2$	$1s^2 2s^2 2p^2 3s^2$
$1s^1 2s^2 2p^3 3p^2$	$1s^2 2s^2 2p^2 3s^2$	$1s^2 2s^2 2p^2 3p^2$
$1s^1 2s^2 2p^3 3d^2$	$1s^2 2s^2 2p^2 3p^2$	$1s^2 2s^2 2p^2 3d^2$
$1s^1 2s^2 2p^4 3p^1$	$1s^2 2s^2 2p^2 3d^2$	$1s^2 2s^2 2p^3 3p^1$
$1s^1 2s^2 2p^4 4f^1$	$1s^2 2s^2 2p^3 3p^1$	$1s^2 2s^2 2p^3 4f^1$
$1s^1 2s^1 2p^5 3d^1$	$1s^2 2s^1 2p^4 3d^1$	$1s^2 2s^1 2p^4 3d^1$

and $1s^22s^12p^5$) energies, and vice versa for the relativistic corrections. This is why we can see a blueshift to the Kα transition energies when we included the relativistic corrections, while a redshift when we included the correlation corrections. Because the relativistic and correlational effects cause contrary shifts to the Kα transition energies, they cancel each other to some degree. Hence, the nonrelativistic single-configuration Hartree-Fock calculation can give reasonably good results. However, it must be noted that the relativistic corrections and the correlation correction do not cancel each other *exactly*. For the transitions considered here, the net adjustment to the wavelengths is about 4 - 6 mÅ. This suggests that to have reliable term-dependent Kα transition energies, both relativistic and correlation effects should be properly accounted for.

Figure 2 shows a comparison of the calculated wavelengths of CI+BP for AlV Kα satellites and the PBFA-II experimental data. The three features in the AlV satellites are attributed to the term-dependent transitions of $1s^12s^22p^5 \rightarrow 1s^22s^22p^4$ and $1s^12s^12p^6 \rightarrow 1s^22s^12p^5$. Very good agreement is achieved. The good agreement between the calculated wavelengths and experimental data allows us to determine with confidence transitions responsible for peaks in an experimental spectrum.

3.2. Structure of the Kα satellites of aluminum ions

Kα radiation in light ion beam experiments is emitted as a result of two processes: ion-impact ionization of a 1s electron followed by a spontaneous fluorescence transition, while the shift of the Kα satellite lines is produced by removing electrons from the L shell. Electrons can be removed from the L shell by both ionization and excitation of thermal electrons and ion beams. For the aluminum plasma considered here, the effect of ionization and excitation of L-shell electrons by ion beams is much smaller than that by thermal electrons because of the lower values of ion impact cross sections. It should be noted the ionization process not only removes an electron from the L shell but also

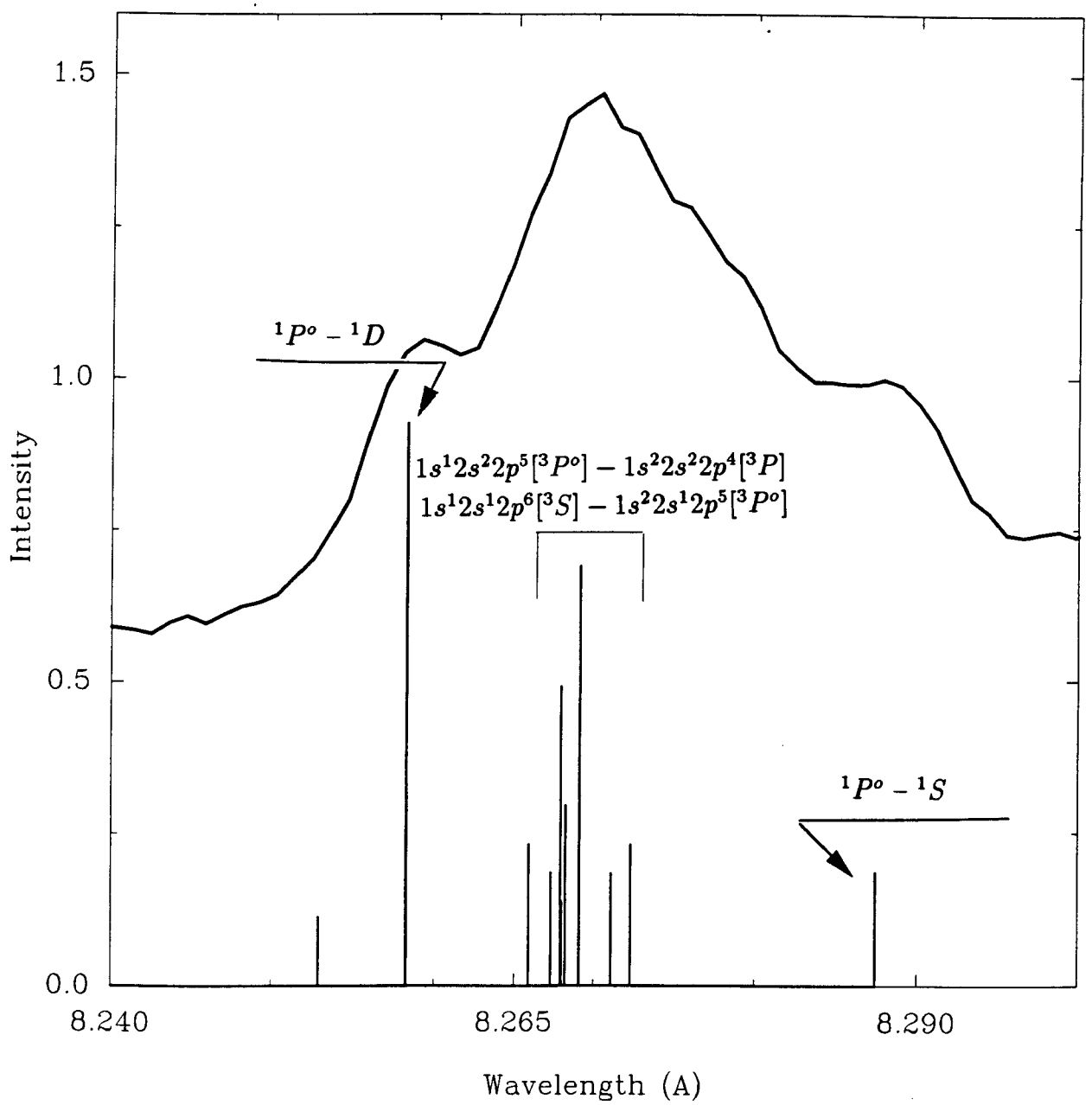

Figure 2. Comparison of the calculated wavelengths and relative intensities (gf) with the PBFA-II experimental data. The stick spectrum represents the lines associated with the transitions $1s^12s^22p^5 \rightarrow 1s^22s^22p^4$ and $1s^12s^12p^6 \rightarrow 1s^22s^12p^5$.

introduces a new ionization stage. In other words, Kα satellite lines shifted by ionization and those shifted by excitation represent two different ionization stages.

Let us look at the processes of Kα emission from ions with one L shell hole created by thermal ionization and excitation in a proton beam heated Al plasma:

$$1s^2 2s^2 2p^6 \overset{thermal\ ionization}{\longrightarrow} 1s^2 2s^2 2p^5 \tag{8}$$

$$1s^2 2s^2 2p^5 \overset{beam\ ionization}{\longrightarrow} 1s^1 2s^2 2p^5 \overset{K\alpha\ fluorescence\ decay}{\longrightarrow} 1s^2 2s^2 2p^4 \tag{9}$$

$$1s^2 2s^2 2p^6 \overset{thermal\ excitation}{\longrightarrow} 1s^2 2s^2 2p^5 nl^1 \tag{10}$$

$$1s^2 2s^2 2p^5 nl^1 \overset{beam\ ionization}{\longrightarrow} 1s^1 2s^2 2p^5 nl^1 \overset{K\alpha\ fluorescence\ decay}{\longrightarrow} 1s^2 2s^2 2p^4 nl^1 \tag{11}$$

For ions with the L shell being an outer shell, if the thermal ionization process in (8) is important, it can be expected that the thermal excitation process in (10) will be appreciable. Hence, to interpret the structure of a Kα satellite line spectrum of a plasma, it is necessary to include the contributions of the transitions involving the excited configuration states of type $1s^1 2s^2 2p^N nl^1$.

We first consider the Kα transitions of AlI to AlIII, i.e., the Kα lines of those ions with no holes in the L shell and with spectator electrons in the M shell. For these ions, the L shell is not an outer shell. It is expected that the transitions involving the excited configuration states with a $2p$ electron excited to the M shell have little contribution to the Kα satellite line spectra. Hence, we only considered the Kα transitions involving ground configuration states, i.e., the transitions of type:

$$1s^1 2s^2 2p^6 3l^N \longrightarrow 1s^2 2s^2 2p^5 3l^N. \tag{12}$$

The calculated wavelengths and gf values of Kα lines are given in Table III. The corresponding stick spectrum is given in Figure 3. It can be seen that the effect of removing electrons from the M shell on the Kα lines is relatively unimportant as the corresponding energy shifts of Kα transitions from AlI to AlIII are small. The Kα lines

cover a rather small range from 8.325 Å to 8.340 Å. By comparing with the PBFA-II experimental spectrum, these Kα satellite lines are unresolvable and give a broad line which is asymmetric toward the short wavelength side.

In the case of AlIV, there are no holes in the L shell in the ground configuration. Two Kα lines are associated with the transition

$$1s^1 2s^2 2p^6 \longrightarrow 1s^2 2s^2 2p^5. \tag{13}$$

Our calculation shows that these two lines overlap the wavelength range of AlI-AlIII. On the other hand, when the L shell is an outer shell, an L shell hole can be easily produced by exciting a 2p electron to the M shell. In this case, we have Kα lines related to the transition group

$$1s^1 2s^2 2p^5 3l^1 \longrightarrow 1s^2 2s^2 2p^4 3l^1, \tag{14}$$

where l represents the s, p, or d subshell. There are about two hundred lines associated with this transition group. The calculated line positions and the corresponding oscillator strengths for these Kα lines will be published elsewhere [11]. In Figure 4, we present the stick spectrum of Kα lines for AlIV, along with the Kα lines for the transitions $1s^1 2s^2 2p^5 \rightarrow 1s^2 2s^2 2p^4$ and $1s^1 2s^1 2p^6 \rightarrow 1s^2 2s^1 2p^5$ of AlV. As shown, the structure of Kα satellite lines for the transition group of $1s^1 2s^2 2p^5 3l^1 \rightarrow 1s^2 2s^2 2p^4 3l^1$ is very complex. These satellite lines are blueshifted with respect to the Kα lines of the ground configuration states of AlIV and strongly overlap the Kα lines of AlV. The blueshift effect is caused by the reduced screening of the nucleus, which results when a 2p electron is excited to the M shell or a higher shell. The overlap effect is because the valence electron in M or a higher shell has little effect on the electronic wavefunctions in the inner regions of the ion, and therefore the effect of removing an electron from the M shell on Kα transition energies is very small. Hence there is no significant shift from $1s^1 2s^2 2p^5 3l^1 \rightarrow 1s^2 2s^2 2p^4 3l^1$ to $1s^1 2s^2 2p^5 \rightarrow 1s^2 2s^2 2p^4$. This overlap phenomenon of Kα

TABLE III

Calculated Wavelengths and gf Values for the
Characteristic Kα Lines from Al I to Al IV

Ion	Transition				Wavelength (Å)	gf
Al I	$1s^2 2s^2 2p^5 3s^2 3p^1$	$[^3D_1]$ –	$1s^1 2s^2 2p^6 3s^2 3p^1$	$[^3P_o]$	8.3373	0.163
		$[^3P_1]$ –		$[^3P_2]$	8.3399	0.104
		$[^3S_1]$ –		$[^3P_2]$	8.3329	0.103
		$[^1P_1]$ –		$[^1P_1]$	8.3374	0.113
		$[^3D_2]$ –		$[^3P_1]$	8.3365	0.326
		$[^3P_2]$ –		$[^1P_1]$	8.3379	0.167
		$[^1D_2]$ –		$[^1P_1]$	8.3363	0.196
		$[^3P_2]$ –		$[^3P_2]$	8.3396	0.246
		$[^1D_2]$ –		$[^3P_2]$	8.3380	0.135
		$[^3D_3]$ –		$[^3P_2]$	8.3359	0.578
Al II	$1s^2 2s^2 2p^5 3s^2$	$[^2P_{1/2}]$ –	$1s^1 2s^2 2p^6 3s^2$	$[^2S_{1/2}]$	8.3369	0.164
		$[^2P_{3/2}]$ –		$[^2S_{1/2}]$	8.3346	0.328
Al III	$1s^2 2s^2 2p^5 3s^1$	$[^3P_1]$ –	$1s^1 2s^2 2p^6 3s^1$	$[^3S_1]$	8.3321	0.237
		$[^3P_2]$ –		$[^3S_1]$	8.3298	0.431
		$[^1P_1]$ –		$[^1S_1]$	8.3303	0.235
Al IV	$1s^2 2s^2 2p^5$	$[^2P_{1/2}]$ –	$1s^1 2s^2 2p^6$	$[^2S_{1/2}]$	8.3270	0.173
		$[^2P_{3/2}]$ –		$[^2S_{1/2}]$	8.3256	0.346

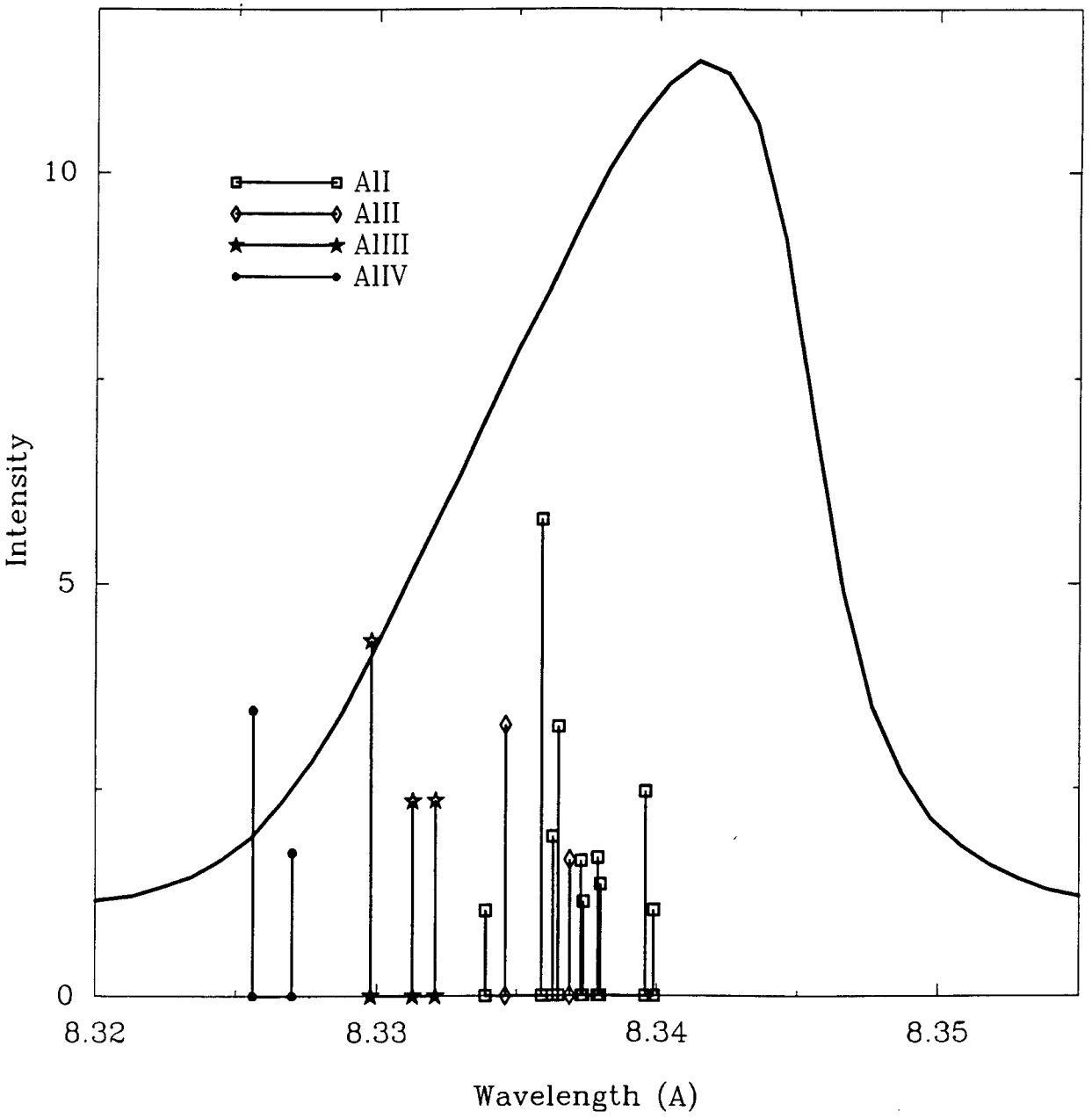

Figure 3. Kα lines for the transitions involving ground configuration states from AlI to AlIV. The broad line is the PBFA-II experimental spectrum.

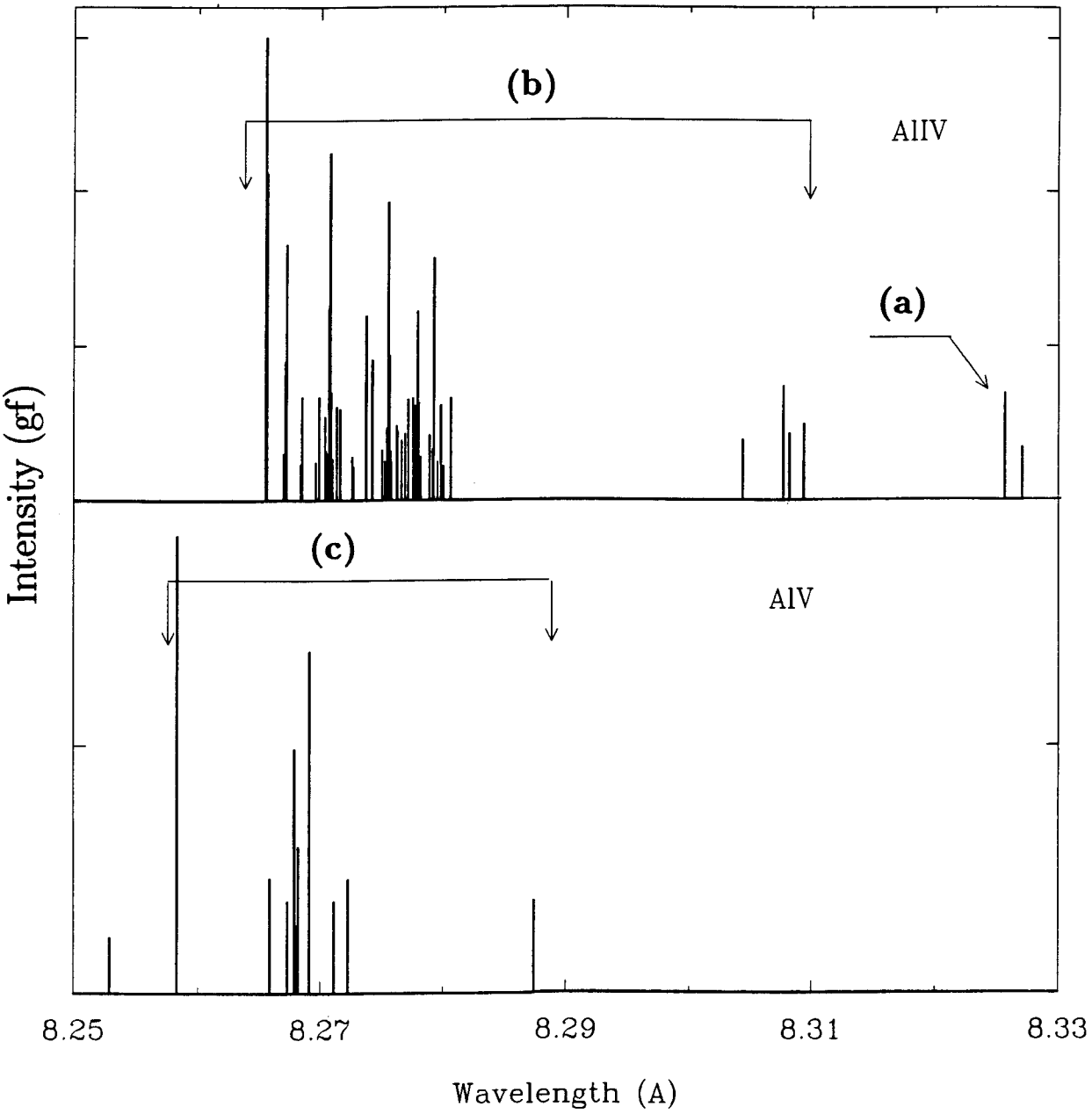

Figure 4. Calculated wavelengths and relative intensities of Kα satellite lines from AlIV and AlV. The lines are classified into groups: (a) $1s^1 2s^2 2p^6 \rightarrow 1s^2 2s^2 2p^5$, (b) $1s^1 2s^2 2p^5 3l^1 \rightarrow 1s^2 2s^2 2p^4 3l^1$, and (c) $1s^1 2s^2 2p^5 \rightarrow 1s^2 2s^2 2p^4$ and $1s^1 2s^1 2p^6 \rightarrow 1s^2 2s^1 2p^5$.

lines of AlIV and AlV may partially explain why the central peak of AlV lines in the PBFA-II experimental spectrum is asymmetric toward the long wavelength side.

Our calculation shows that this overlap phenomenon also appears for other ions in higher ionization stages. All the calculated results are summarized in Figure 5, Figure 6, and Figure It can be seen from the figures that the Kα lines for a specific ionization stage can be classified into two groups. One is the 'characteristic group', which represents the characteristic Kα line position of the ionization stage. The Kα lines of this group are from the transitions involving the ground configuration states and the transitions involving excited configuration states with a 2s electron excited to a 2p subshell. Another is the 'overlap group', which overlaps the characteristic Kα lines of the next higher ionization stage and affects the whole characteristic line shape. The Kα lines of this group are from the transitions involving the excited configuration states with a 2p electron excited to the M shell or a higher shell. This overlap phenomenon of Kα lines of two consecutive ionization stages is important for the spectroscopy analysis of Kα satellite spectra. It has been found [3,12] that the Stark broadening effect for the lines in the overlap group is much stronger than that for the lines in the characteristic group. In a plasma of moderate to high density, the lines in overlap groups show a much more pronounced dependence on electron density than those in characteristic groups. Thus, the Kα lines in overlap groups offer better opportunities for diagnosing plasma densities.

In Figure 8, we present a stick spectrum which includes the Kα lines of AlI to AlXI and compare with the PBFA-II experimental spectrum. It can be seen that the overlap effect of the Kα satellite lines of two consecutive ionization stages plays an important role for the broad feature of the Kα satellite lines in the experimental spectrum. Other effects, such as the opacity effect and time integration effect, can also have contributions to the broad line shape. Detailed discussions of these effects have been given elsewhere [12]. Our calculation also shows that the peak with the shortest wavelength in the experimental

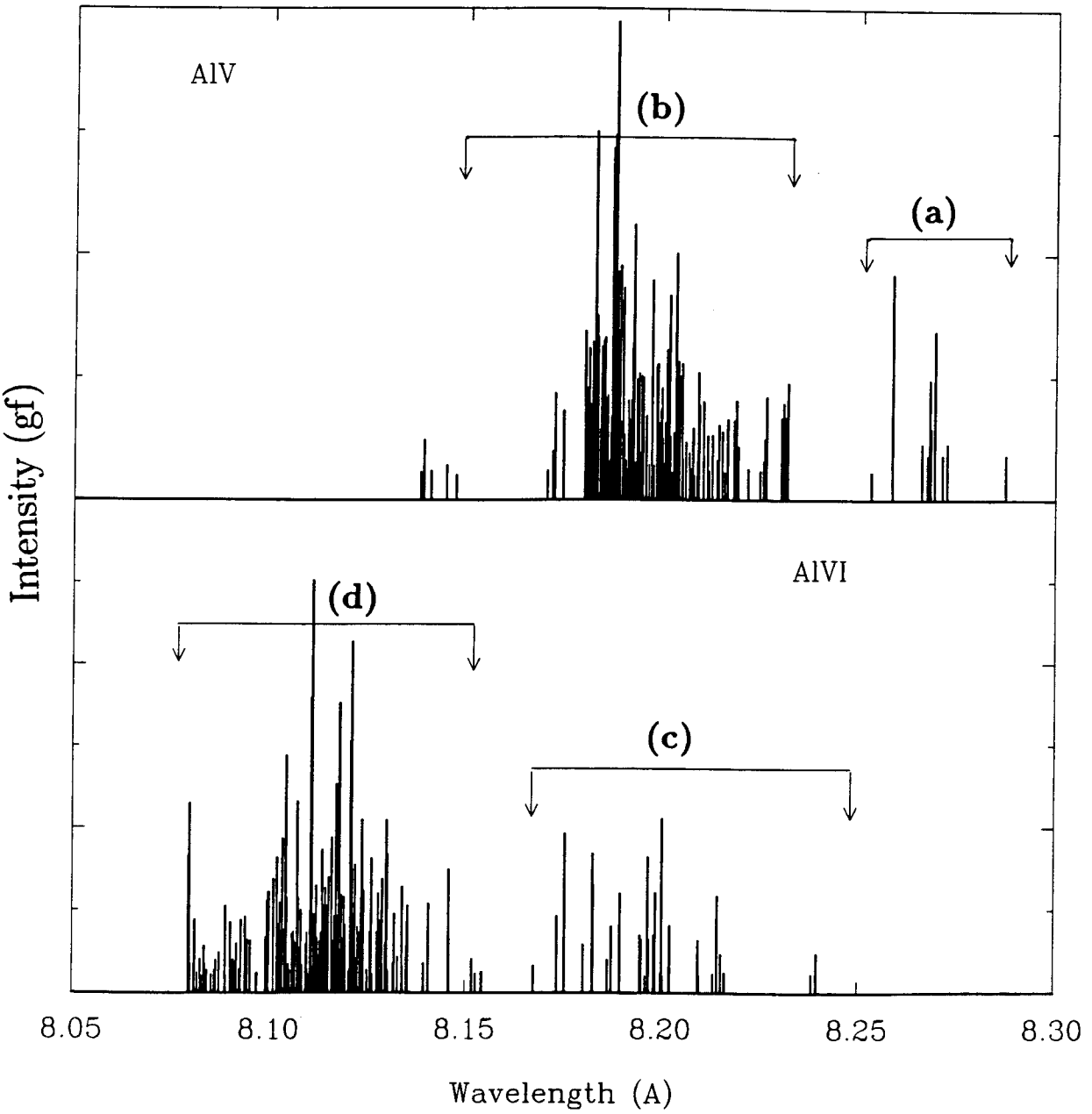

Figure 5. Calculated wavelengths and relative intensities of Kα satellite lines from AlV and AlVI. The lines are classified into groups: (a) $1s^1 2s^2 2p^5 \rightarrow 1s^2 2s^2 2p^4$ and $1s^1 2s^1 2p^6 \rightarrow 1s^2 2s^1 2p^5$, (b) $1s^1 2s^2 2p^4 3l^1 \rightarrow 1s^2 2s^2 2p^3 3l^1$, (c) $1s^1 2s^M 2p^N \rightarrow 1s^2 2s^M 2p^{N-1}$, and (d) $1s^1 2s^2 2p^3 3l^1 \rightarrow 1s^2 2s^2 2p^2 3l^1$.

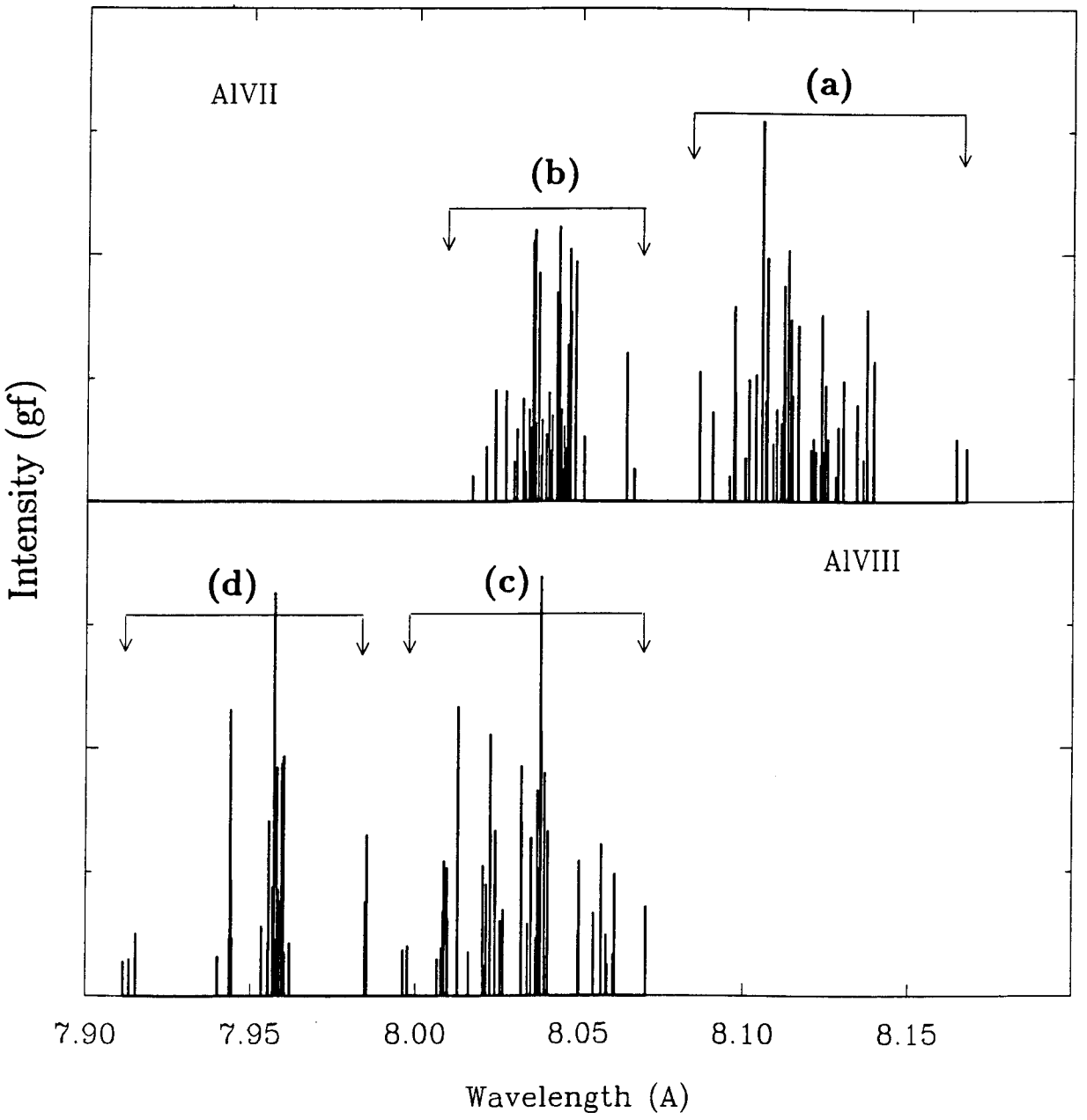

Figure 6. Calculated wavelengths and relative intensities of Kα satellite lines from AlVII and AlVIII. The lines are classified into groups: (a) $1s^1 2s^M 2p^N \rightarrow 1s^2 2s^M 2p^{N-1}$, (b) $1s^1 2s^2 2p^2 3l^1 \rightarrow 1s^2 2s^2 2p^1 3l^1$, (c) $1s^1 2s^M 2p^N \rightarrow 1s^2 2s^M 2p^{N-1}$, and (d) $1s^1 2s^2 2p^1 3l^1 \rightarrow 1s^2 2s^2 3l^1$.

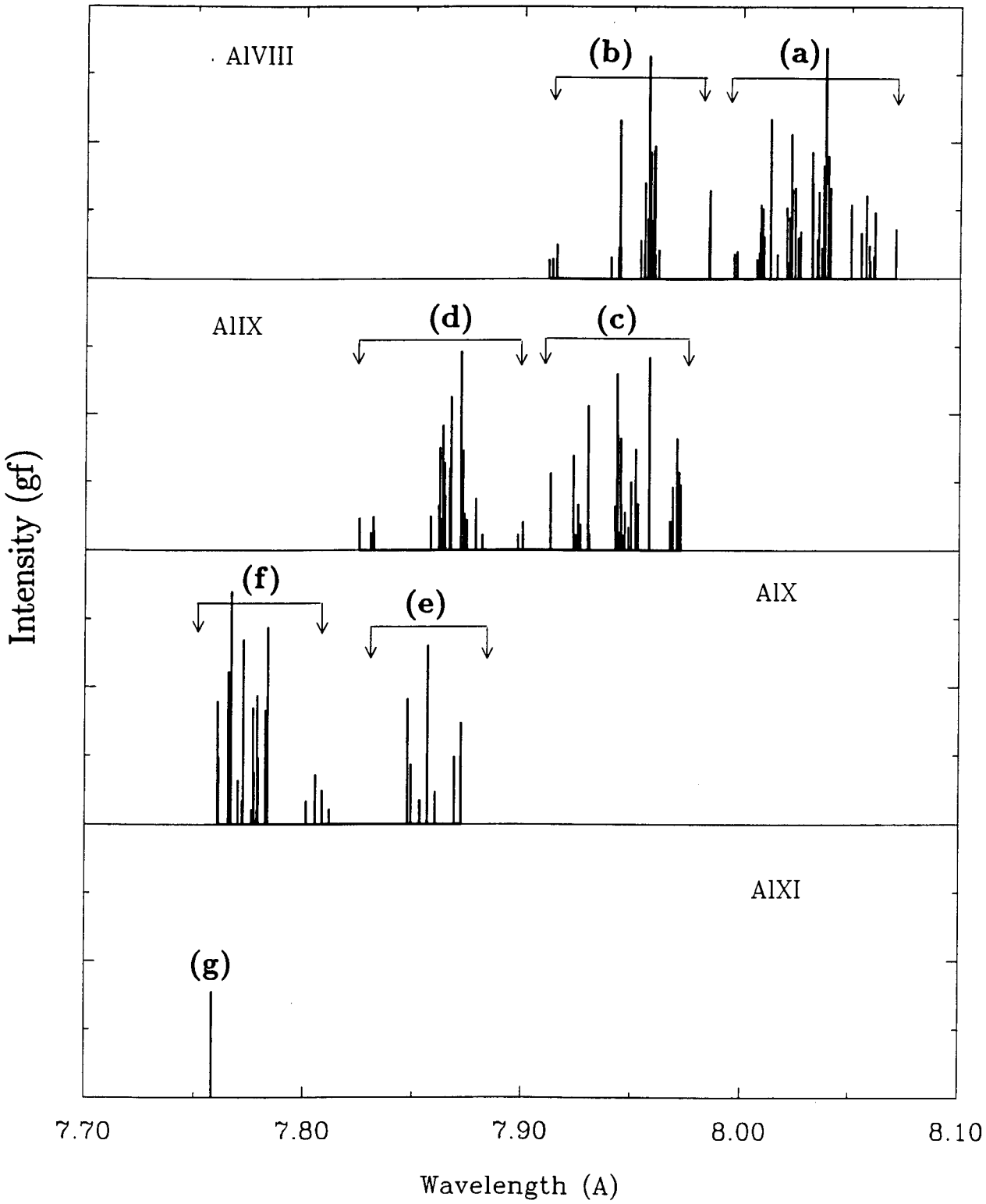

Figure 7. Calculated wavelengths and relative intensities of Kα satellite lines from AlVIII to AlXI. The lines are classified into groups as shown.

spectrum is actually attributed to the Kα transitions of ground configuration states of AlIX, excited states of AlVIII, and the Kβ transition of AlI.

4. Conclusions

In order to analyze the experimental aluminum Kα spectrum of a PBFA-II experiment, it is necessary to understand the detailed structure of Kα satellite lines of aluminum ions. In this paper, we have used the CI+BP method to calculate the transition energies and oscillator strengths for the Kα transitions of aluminum ions. Our calculated wavelengths for the most prominant Kα transitions agree well with the PBFA-II experimental data. In particular, we have calculated the properties for Kα lines involving excited configuration states. It has been found from our calculations that for ions with the L shell being an outer shell (AlIV to AlXI), the corresponding Kα satellite lines can be classified into 'characteristic' and 'overlap' groups. The 'characteristic' group, which is associated with the lines of transitions involving ground configuration states, can be used for characterizing the ionization stage, while the 'overlap' group, which is associated with the Kα lines of transitions involving excited configuration states with a 2p electron excited to the M shell or higher shells, can have important effects on the line shape of Kα satellite lines.

Our calculated results have been used to simulate the Kα experimental spectrum of a PBFA-II experiment with a collisional-radiative-equilibrium (CRE) model post-processed by hydrodynamics simulations. Good agreement with the experimental spectrum is achieved. The simulation results are described elsewhere [12].

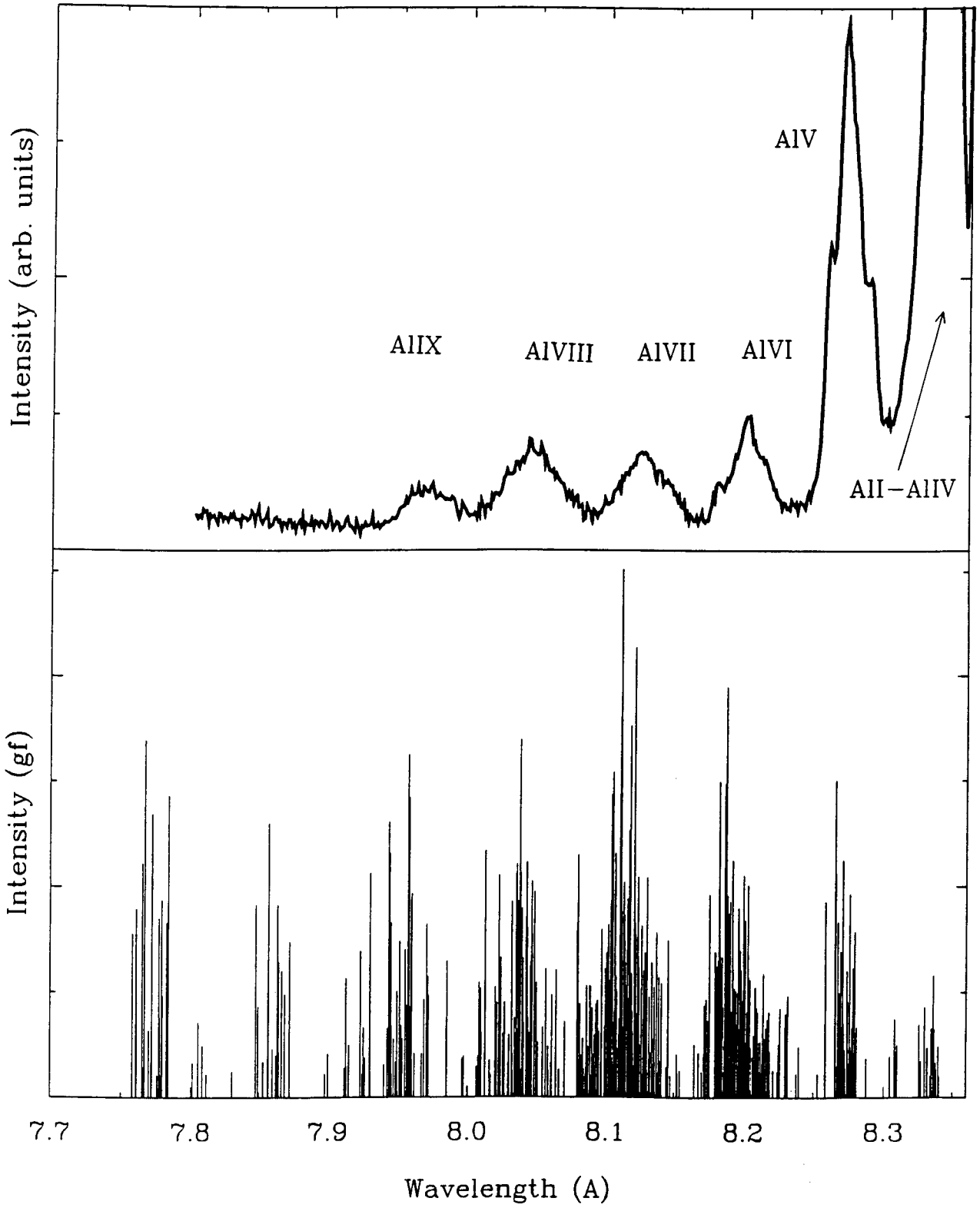

Figure 8. Theoretically calculated Kα satellite spectrum of aluminum. Upper: PBFA-II experimental Kα spectrum.

Acknowledgements

This work has been supported in part by the Sandia National Laboratories and by Kernforschungszentrum Karlsruhe (FRG) through Fusion Power Associates. Computing support was provided in part by the National Science Foundation through the San Diego Supercomputer Center.

References

1. E. Nardi, Z. Zinamon, *J. Appl. Phys.* **52**, 7075 (1981).

2. J. Bailey, A.L. Carlson, G. Chandler, M.S. Derzon, R.J. Dukart, B.A. Hammel, D.J. Johnson, T.R. Lockner, J. Maenchen, E.J. McGuire, T.A. Mehlhorn, W.E. Nelson, L.E. Ruggles, W.A. Stygar, and D.F. Wenger, *Lasers and Particle Beams* **8**, 555 (1990).

3. R. Mancini, *Priviate Communication*, (1991).

4. C. Chenais-Popovics, C. Fievet, J.P. Geindre, and J.C. Gauthier, *Phys. Rev.* **40**, 3194 (1989).

5. M. Klapisch, J.L. Schwob, B.S. Fraenkel, and J. Oreg, *J. Opt. Soc. Am.* **67**, 148 (1977).

6. C.F. Fischer, *Comp. Phys. Commun.* **14**, 145 (1978).

7. S. Fraga, M. Klobukowski, J. Muszynsha, K.M.S. Saxena, J.A. Sordo, and J.D. Climenhaga, *Comp. Phys. Commun.* **47**, 159 (1987).

8. J.F. Perkins, *J. Chem. Phys.* **45**, 2156 (1965).

9. R. Glass, A. Hibbert, *Comp. Phys. Commun.* **16**, 19 (1978).

10. S. Fraga, M. Klobukowski, J. Muszynsha, K.M.S. Saxena, and J.A. Sordo, *Phys. Rev.* **34**, 23 (1986).

11. P. Wang, J.J. MacFarlane, and G.A. Moses, *Atomic Data and Nuclear Data Tables*, to be submitted (1992).

12. J.J. MacFarlane, P. Wang, J. Bailey, T.A. Mehlhorn, R.J. Dukart, and R. Mancini, *Phys. Rev.* submitted (1992).

Appendix C

Theoretical Spectroscopic Analysis of Intense Ion Beam-Plasma Interaction in the PBFA-II Gas Cell

P. Wang, J.J. MacFarlane, G.A. Moses, J.E. Bailey

(Proceedings of the Beams '92 Conference, Washington, DC, 1992)

Theoretical Spectroscopic Analysis of Intense Ion Beam-Plasma Interaction in the PBFA II Gas Cell

P. Wang, J. J. MacFarlane, and G. A. Moses
Fusion Technology Institute, University of Wisconsin, Madison, WI 53706

J. E. Bailey
Sandia National Laboratories, Albuquerque, NM 87185

Abstract

Time-resolved visible emission spectra from the PBFA II argon gas cell were measured in recent light ion beam-target interaction experiments. These emission spectra may be used to study the physics of beam transport and diagnose the cell plasma conditions. We discuss the theoretical analysis of the emission spectra in the wavelength region from 4300 to 4420 Å, where several ArII lines are observed. We examine opacity effects on the emission lines and assess the importance of beam excitation effects. Theoretical spectra are compared with the experimental data.

Introduction

Visible spectral line emission from the PBFA II argon gas cell is of current interest because it can be used as a diagnostic for both light ion beam properties and cell plasma conditions[1]. For example, spectral line profiles emitted by atoms in the transport region may be sensitive to the electron density. By measuring and modeling the line profiles one may be able to determine electron densities in the gas cell, which in turn can be used to estimate the extent of beam neutralization. Spectral lines can potentially be produced by both ion-impact excitation and thermal electron collisional excitation. If one can identify transitions dominantly produced by ion-impact excitation, then the time-dependent line intensity can be used to measure beam current and beam divergence. It is expected that the ranges for cell plasma conditions are $T_e = 0.5 - 5$ eV and $N_e = 10^{16} - 10^{18}$ cm^{-3}. Under such conditions, opacity effects for the emission lines may be important. If the emission lines are optically thick, spectral line profile interpretation must be in conjunction with the radiation transport analysis.

In this paper, we study the opacity effects on the line emissions from the PBFA II argon gas cell and compare calculated emission spectra with the experimental data. We present results of

calculations comparing the effects of beam excitation versus thermal excitations. We also examine the effects of carbon impurity of ion beam on level populations.

Theoretical Models

We present in this section a brief overview of the theoretical models used to compute the spectral properties and related atomic data. A detailed description of these models is presented elsewhere.[2-5]

In our calculations, we use a collisional-radiative equilibrium (CRE) code[2] in which steady-state ionization and excitation populations can be computed by solving multilevel atomic rate equations self-consistently with the radiation field. For the plasma conditions discussed in this paper, the distribution of atomic level populations were found to be close to local thermodynamic equilibrium (LTE). We have therefore neglected photoexcitation and photoionization effects in level population calculations.

Our atomic model for Ar consists of 192 levels distributed over the first five ionization stages (ArI–ArV). Energies for levels related to the lines of interest were selected from National Bureau of Standards tables[6]. Other level energies were obtained from Hartree-Fock calculations. The collisional couplings are complete for the resonant transitions from the ground state to the higher levels and the cross sections are calculated with the Born-Coulomb approximation, while the less important cross sections of the remaining transitions among the excited levels were approximated by a semi-classical impact parameter model, valid for dipole-allowed transitions. Ion impact excitation and ionization cross sections are calculated using a plane wave Born approximation (PWBA) model. It is necessary to indicate that the beam excitation and ionization effects were not directly included in the CRE calculation in this preliminary study. The beam effects are checked separately by comparing the excitation rate with those of the corresponding thermal electron process.

After the level populations are obtained, emission spectra are computed using an escape probability radiative transfer model which includes contributions from bound-bound, bound-free, and free-free transitions. In examining the opacity effects of spectral emission lines, spectral line widths are critical. Voigt line profiles are used to model line shapes. Natural, Doppler and Stark broadening effects are considered. Stark width is calculated in the electron impact approximation using the semi-empirical method of Griem[7]. By comparing the calculated Stark widths with available experimental data[8], the agreement is typically within a factor of 2.

Calculations and Discussion

In this study, calculations were run for the plasma conditions of $n_{ion} = 1.8 \times 10^{17}$ cm^{-3}, T_e =1, 2, 2.5, 3, and 4 eV. In each case we assumed a planar plasma of width 4 cm which represents the

height of the gas cell and therefore the maximum line-of-sight distance through the Ar plasma. The electron density dependence on temperature is given in Table I. We have looked in particular at the wavelength region from 4300 to 4420 Å. All of the lines in this region have been identified as ArII lines. An experimental spectrum and the corresponding transition diagram are presented in Figure 1.

Table I. Dependence of Electron Density on Temperature

T (eV)	n_e (10^{17} cm^{-3})
1.0	0.4
2.0	2.2
2.5	3.2
3.0	3.7
4.0	5.1

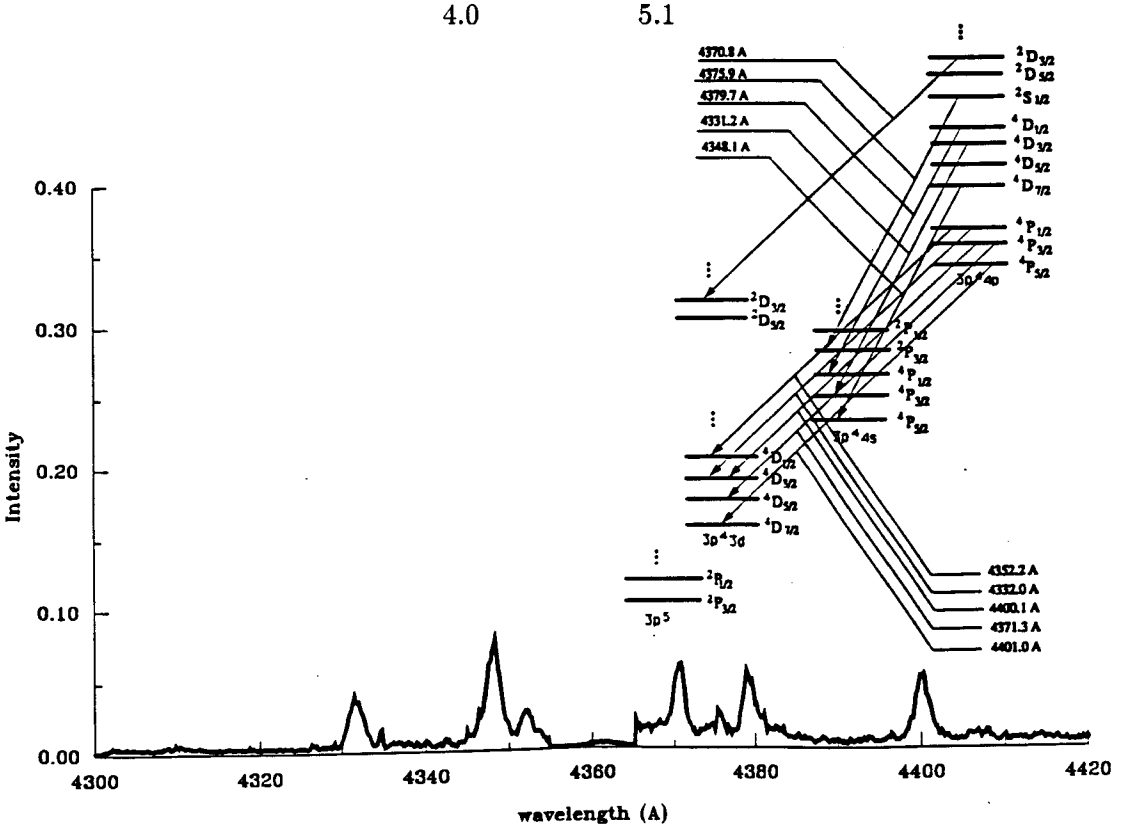

Figure 1. Spectra for shot 4659 in PBFA II experiment and the corresponding transition diagram.

Figure 2 shows a comparison between calculations with and without opacity at T_e = 2.5 eV. The 4348 Å line is most strongly affected by opacity, while some of the other lines are to a smaller extent. This is in qualitative agreement with the experimental spectrum because the 4348 Å line width was found to be considerably broader than the other lines[1]. We checked the sensitivity of the spectrum to the temperature and found that at T = 1 eV and T = 4 eV the spectral flux is

very small. The ArII lines show up best at $T = 2 - 3$ eV. The ratio of the 4348 Å line to other lines increases above $T = 2.5$ eV because the opacity begins to drop. This can be seen more clearly from Figure 3, which shows the optical depth as a function of temperature and wavelength. The 4348 Å line has the greatest optical depth, with its line center value rising to about $5 - 6$ at $T = 2 - 2.5$ eV.

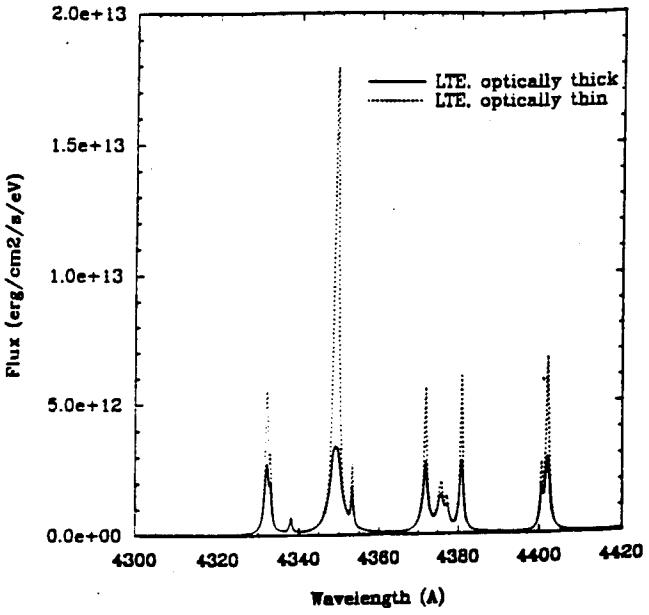

Figure 2. Opacity effects on lines of interest.

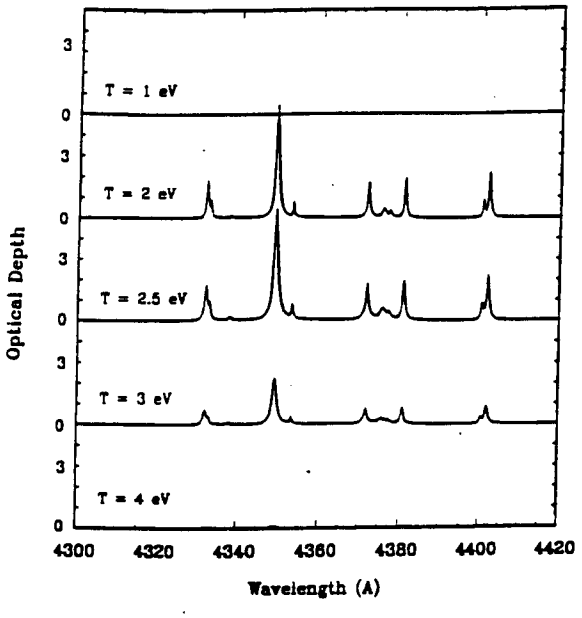

Figure 3. Sensitivity of optical depth to temperature for lines of interest.

The role of ion beam impact excitation on level populations and line intensities can be examined by comparing the excitation rate with those of corresponding thermal electron collisional processes. For the intercombination transitions ($\Delta S = 1$), ion impact excitation cross sections are extremely small for high energy ion beams ($\mathcal{E}_{ion} \leq 1$ MeV). This is because there is only exchange interaction for intercombination transitions, and when $\mathcal{E}_{ion} \gg 1836 \times \Delta E_{ij}$, the exchange cross section decreases $\propto \mathcal{E}_{ion}^{-3}$. For the transitions with $\Delta S = 0$, ion impact excitation cross sections are substantially larger in the beam energies of interest. The excitation rate can be comparable to or even dominate the thermal electron collisional rate. Figure 4 compares the excitation rate for electron collisional excitation versus proton beam impact excitation as a function of the electron temperature for several important transitions relevant to the lines of interest. It can be seen that the rates for electron collisional excitation and proton beam impact excitation are approximately the same for allowed transitions when $T = 2 - 3$ eV. For intercombination transitions, the electron collision rate dominates. For the spectral lines of interest, most of the excited levels are coupled to the ground state by intercombination transitions, hence the direct coupling by ion impact excitation is not important for these levels. However, the populations of these levels may be affected by ion impact

excitation in an indirect way, i.e., these levels can be strongly coupled to other levels which are related to the ground state via allowed transitions by electron collisional excitation.

There is about a 15% carbon impurity in the high energy proton beam. Whether carbon impact may play a role in affecting the level populations depends on the magnitude of corresponding excitation cross sections. Figure 5 shows the proton-impact and carbon-impact (CVII) cross sections for several excitation transitions. In PBFA II experiments, the proton energy is about 6 MeV and the energy of the carbon impurity is about 12 – 21 MeV. The current density of the carbon impurity is a factor of 4 smaller than that of the proton, while the corresponding carbon-impact excitation cross section is about several times that of the proton-impact cross section and hence the excitation rates are about the same. This suggests that for those transitions in which ion-impact excitations are important, both proton and carbon excitations should be considered.

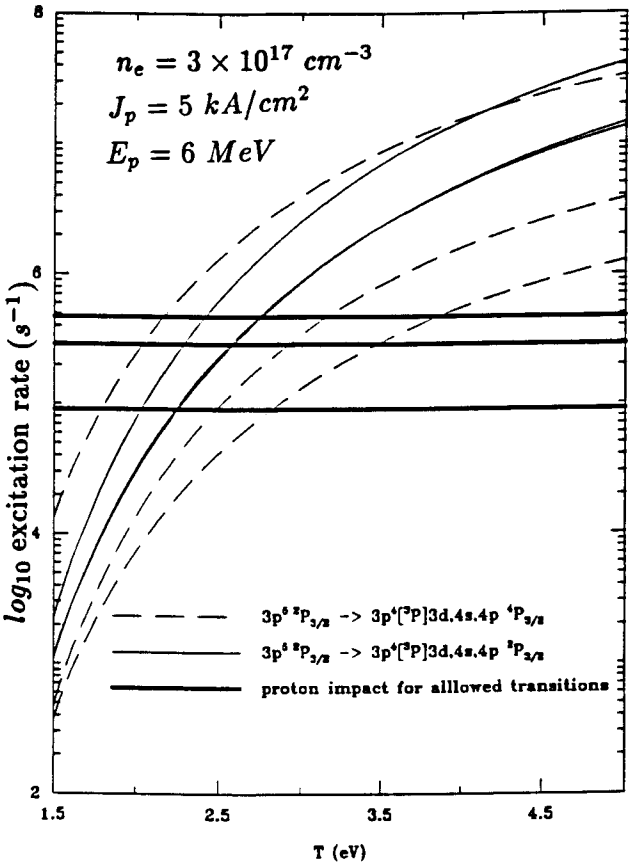

Figure 4. Electron collisional and proton beam impact excitation rate.

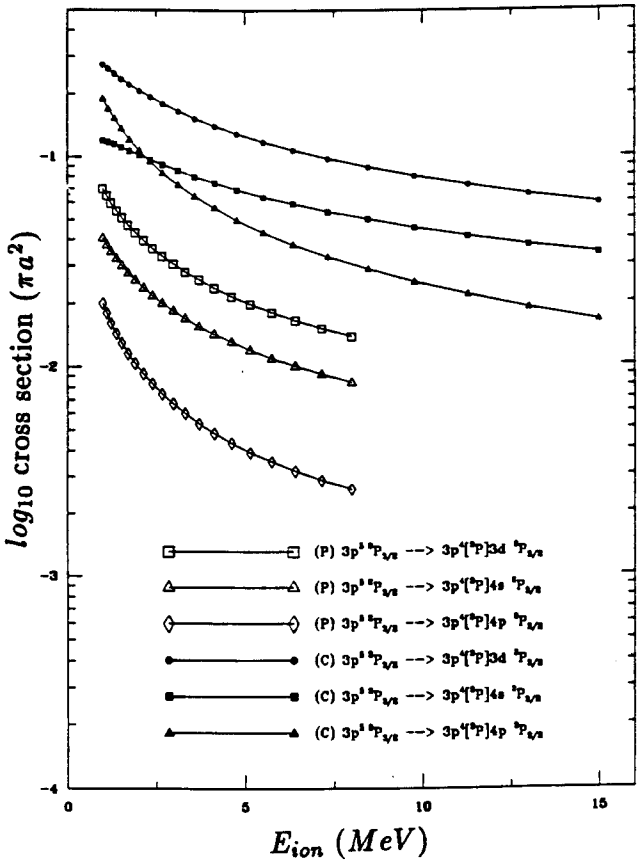

Figure 5. Proton- and carbon-impact excitation cross sections.

Summary

The preliminary results obtained from this study show that the strongest ArII lines observed in the PBFA II argon gas cell (e.g., 4348 Å) may have optical depths of order ten, while many of the

other lines may have optical depths of order unity. Opacity effects should therefore be considered in interpreting the observed spectra. We also find that the ion beam impact excitation can be important for allowed transitions but can be neglected for intercombination transitions. Carbon- and proton-impact excitation rates were found to be comparable in magnitude. In the followup study, we intend to perform more detailed calculations to assess the importance of ion beam impact excitation effects on level populations.

Acknowledgements

This work was supported by Sandia National Laboratories and Kernforschungszentrum Karlsruhe. Computing support has been provided in part by the National Science Foundation through the San Diego Supercomputing Center.

References

1. Bailey, J.E., Carlson, A.L., Johnson, D.J., McGuire, B.J., Nash, T., MacFarlane, J.J., and Wang, P., 9th International Conference on High Power Particle Beams, Washington, D.C., May 25 - 29, 1992.

2. MacFarlane, J.J., Wang, P., and Moses, G.A., Report No. UWFDM-822, Fusion Technology Institute, University of Wisconsin, Madison, WI, 1990.

3. MacFarlane, J.J., Wang, P., and Moses, G.A., *Lasers and Particle Beams* **8**, 729 (1990).

4. MacFarlane, J.J., Wang, P., and Henderson, D.L., Report No. UWFDM-847, Fusion Technology Institute, University of Wisconsin, Madison, WI, 1991.

5. Wang, P., *Computation and Application of Atomic Data for ICF Plasmas*, Ph.D. Dissertation, Dept. of Nuclear Engineering and Engineering Physics, University of Wisconsin, Madison, WI (1991).

6. Reader, J., Corliss, C.H., Wises, W.L., and Martin, G.A., *Wavelengths and Transition Probabilities for Atoms and Atomic Ions*, National Bureau of Standards (1990).

7. Griem, H.R., Phys. Rev. **165**, 258 (1968).

8. Konjevic, N., and Roberts, J.R., *J. Phys. Chem. Ref. Data* **5**, 209 (1976).